

UNIVERSITY OF MANCHESTER

**Surface Integrity Through Tomographic
Reconstruction**

by

James Andrew Carr

School of Materials

A thesis submitted to The University of Manchester for the degree of
Doctor of Philosophy
in the Faculty of Engineering and Physical Sciences

2015

Contents

List of Figures	6
List of Tables	10
Abbreviations	11
Abstract	13
Declaration	14
Copyright Statement	15
Acknowledgements	17
The Author	19
1 Introduction	21
2 Digital Imaging Techniques	24
2.1 Introduction	25
2.2 2D Imaging Techniques	25
2.2.1 Scanning Electron Microscopy	26
2.2.2 Transmission Electron Microscopy	27
2.2.3 Energy-Dispersive X-ray Spectroscopy and Other Signals	27
2.3 Sample Preparation	29
2.3.1 Ultramicrotomy for SBFSEM	29
2.3.2 FIBSEM Sample Preparation	30
2.3.3 Ultramicrotomy for TEM	30
2.4 3D Imaging	31
2.4.1 Tomography	31
2.4.2 Serial Block-Face Imaging	34
2.4.3 Serial Block-Face Imaging: A Review	36
2.4.3.1 Introduction	36
2.4.3.2 Automated serial sectioning	36
2.4.3.3 Limitations of SBFI	37
2.4.4 Contemporary Capabilities of 3D Imaging	38

2.4.5	X-Ray Tomography	39
2.4.6	Serial Block-Face Scanning Electron Microscopy	40
2.4.6.1	3View	40
2.4.6.2	FIBSEM	42
2.5	Concluding Remarks	43
3	Quantitative Characterization for Tomographic Imaging	44
3.1	Introduction	45
3.2	3D Images	46
3.2.1	Voxels	47
3.2.2	Bit depth	47
3.3	Tomographic Reconstruction	49
3.4	Preprocessing for SBF	52
3.4.1	Stack Alignment	52
3.5	Image Processing	53
3.5.1	Kernel Based Filtering	53
3.5.2	Advanced Filters	57
3.5.2.1	Anisotropic Diffusion	57
3.5.2.2	Morphological filtering	58
3.5.3	Image Registration	60
3.6	Segmentation	60
3.6.1	Thresholding	61
3.6.2	Watershed	63
3.6.3	Other tools and semi-automatic methods	64
3.7	Connected Component Labelling	66
3.8	Quantification I	69
3.8.1	Volume	69
3.8.2	Barycentre	71
3.8.3	Feret Diameter	73
3.8.4	Surface Area	74
3.9	Quantification II	77
3.9.1	Effective Diameter	77
3.9.2	Shape	78
3.9.3	Spatial Distributions	79
3.9.3.1	Number density	79
3.9.3.2	Nearest neighbour	80
3.9.3.3	First order clustering	81
3.9.3.4	Pair correlation function	82
3.10	Finite Element Analysis (FEA)	84
3.10.1	Meshing	84
3.10.2	Reformulation	87
3.10.3	Solving	89
3.11	Resolution	90
3.12	Concluding remarks	93
4	Aesthetic Properties of Protective Coatings	95
4.1	Introduction	96
4.2	Review of Light Scattering	97

4.2.1	Mie Scattering and Other Boundary Condition Methods	98
4.2.2	Extended Boundary Condition Method (T-Matrix Method)	99
4.2.3	Discretized integral formulation method (The Moment Method)	100
4.2.4	Multiple scattering (Monte Carlo and Kubelka-Munk)	100
4.3	Objectives	102
4.4	Samples	103
4.5	2D Quantification	107
4.6	Methodology	108
4.7	Results & Discussion	109
4.8	Conclusions	118
5	Multi-scale Tomographic Characterization of Inhibitors in Protective Aerospace Coatings	119
5.1	An introduction to corrosion inhibition	120
5.1.1	Corrosion	120
5.1.2	Inhibition of corrosion	122
5.2	Mechanism of Chromate Inhibition	124
5.3	Transport of Chromate Inhibitors	126
5.4	Experimental and Analytical Methods	131
5.5	Results and Discussion	132
5.6	Conclusions	144
6	Quantitative Characterization of Porosity and Determination of Elastic Modulus for Sintered Micro-silver Joints	145
6.1	Introduction	146
6.1.1	Background to Sintered Micro-Silver Joints	147
6.1.2	Elastic behaviour of porous solids	147
6.1.3	Aims	149
6.2	Materials and Methods	149
6.2.1	Specimen Production	149
6.2.2	Experimental Determination of Young's Modulus	150
6.2.3	SBFSEM	151
6.2.4	Image Processing and Quantification Methodology	152
6.2.5	Finite Element Image Based Modelling	153
6.3	Results and Discussion	154
6.3.1	Quantification	154
6.3.2	Influence on the Elastic Properties	159
6.4	Conclusions	162
7	Conclusions and Suggestions for Further Work	163
A	Nearest Neighbour Code	166
B	Transport Modelling in Shale	171
B.1	Background	172
B.2	Motivation	172
B.3	Methods	173
B.3.1	Experimental	173

B.3.2 Computational	173
B.4 Results	174
B.5 Conclusions and Further Work	177

Bibliography	178
---------------------	------------

List of Figures

2.1	The interactions that can result from an incident beam of electrons [1].	26
2.2	A more detailed explanation of the electron interactions from an atomic perspective [1].	28
2.3	(a) A view of the ultramicrotome from above. The sample moves in and out of the page to allow the blade to slice the sample. (b) A view from the side showing the motion of the sample in the holder against the blade. (c) The final dimensions of the sample ready for scanning.	30
2.4	Schematic of a typical tomography setup for a parallel beam.	32
2.5	Schematic of a typical tomography setup for a ‘divergent’ or ‘cone’ beam. The magnification of the projection is due to the divergent source.	33
2.6	Discretisation of the projection intensity distribution on the projection space defined by (x_p, y_p)	34
2.7	Layout of I13-Imaging beamline at DLS	40
2.8	A schematic diagram of the 3View facility.	41
2.9	A schematic of a typical FIBSEM facility.	42
3.1	A high level overview of the work-flow for tomographic datasets.	46
3.2	The discretization of detected signal as a result of bit depth.	48
3.3	The acquisition of projections (left) and reconstruction by BP (right).	50
3.4	A series of projections and the corresponding sinograms as seen from the top of the stacked projections.	50
3.5	The formation of a sinogram of a point sample misaligned from the centre of rotation.	51
3.6	Showing the iterative reconstruction methodology.	52
3.7	The convolution of an image, I_{ij} , with the kernel, F_{kl}	54
3.8	The input (left) and output (right) image after application of a 2 by 2 median filter.	56
3.9	A binary image undergoing closing. Active pixels are shown in white.	58
3.10	The segmentation of a phase by histogram based thresholding.	62
3.11	Watershed segmentation by the flooding from selected seeds.	64
3.12	A particle with a weak boundary that allows leaks into the matrix by a region growing algorithm.	65
3.13	The interpolation between 3 selections made using a 2D region growing algorithm.	66
3.14	A 2D binary image undergoing CCL. The top right labelled image shows 2 separate connected regions whereas the bottom left shows 5 separate connected regions.	67
3.15	A central pixel with a 4-connected neighbourhood (blue) and an 8-connected neighbourhood (blue+red).	68
3.16	Three kinds of neighbourhood for a 3D image: (a) 6-connected; (b) 18-connected; and (c) 26-connected.	68

3.17	A particle of arbitrary shape, showing the Feret diameter $F(\theta)$	73
3.18	Two methods for calculating perimeter of a digitized 2D interface.	75
3.19	The 4 fundamental line segment configurations as a function of the 4-voxel neighbourhood.	75
3.20	A surface generated on a pixelized boundary (shown in red) using the Marching Squares algorithm. The generated surface is shown by the dotted line.	77
3.21	A distribution of points with a central reference point (left) and the corresponding plots of n_i , r_i^2 and $g(r)$	83
3.22	The typical shape of a PCF.	83
3.23	The meshing of an STL surface by splitting and consequential removal of hexahedra FE cells.	86
3.24	Splitting of square elements (2D) and hexahedra elements (3D).	86
3.25	A tapered rod suspending a weight of mass m can be simplified by dividing the geometry into discrete elements.	88
3.26	A schematic demonstrating the convolution of two points (shown in red) separated by a distance r with the SEM incident beam (shown in yellow) of spot size d	91
3.27	Illustration of the impact of spot size on the representation of two close together points.	92
3.28	The discretizaion of two close togther objects.	93
4.1	The mathematical considerations used in the Kubelka-Munk method where a film of thickness L atop a material of known reflectance R_g is illuminated by a source of intensity I reflects with intensity J	102
4.2	A volume rendering of the organic extender used in sample 103.	103
4.3	Scanning electron micrographs of samples 103 (a), 104 (b) and 105 (c) showing the extenders and TiO_2 particles in the epoxy binder. The scale bars are $10 \mu\text{m}$	104
4.4	TEM images of the TiO_2 particles. The scale bars are 50 nm	106
4.5	The fitted, normalized 2D NN distributions for a 2D image (blue) and 3D image (red).	108
4.6	A schematic showing the possibility of the NN lying below the imaged 2D surface.	108
4.7	(a) Histogram of the NN distribution of the 3View images at the lowest magnification. (b) Fitted PDFs of the histogram data in (a).	110
4.8	(a) Mean NN distance plotted against spreadability. (b) Clustering factor R_n plotted against spreadability.	111
4.9	(a) Cross section showing the sweeping of TiO_2 by the ultramicrotome. (b) Surface rendering of the labelled low magnification 3View settings showing the impact on particle shapes. The scale bars are $1 \mu\text{m}$	113
4.10	(a) Single slice of sample 103 as acquired by FIBSEM. (b) Single slice of sample 103 as acquired by 3View using the high magnification settings. The scale bars are $2 \mu\text{m}$	114
4.11	Quantification of NN distribution using both magnifications used in the 3View as well as the FIBSEM data.	114
4.12	Surface rendering of the labelled FIBSEM data.	115
4.13	Comparison of the 3D NN distributions as calculated from the 3View data and the down-sampled FIBSEM data.	116
4.14	Quantification of the FIBSEM data: (a) The effective diameter distribution. (b) NN versus effective diameter scatter. (c) NN isoplot. (d) PCF.	117
4.15	Fitted ellipsoids generated from the FIBSEM image data.	117

5.1	The two half reactions involved in the corrosion of iron with the anodic reactions in red and the cathodic reactions in blue.	121
5.2	Evans diagrams showing how CIs influence the corrosion rates by affecting the anodic and/or the cathodic reactions [2].	124
5.3	The formation of a defect site in a primer layer coating applied to a metal substrate followed by the formation of a passivation layer at the defect site. .	126
5.4	A schematic of the transport mechanism by connected clusters. (a) An epoxy matrix (yellow) with inhibitor material (blue) and connectivity between particles by void space (shown in black). (b) An epoxy matrix saturated with water (green) and void spaces filled with water (red). (c) The creation of a defect in an aqueous environment. (d) The depletion of inhibitor material connected to the defect site with the depleted inhibitor material replaced with water-filled void (red).	130
5.5	Normalized transmission during radiography as a function of the Bragg angle of the monochromator.	132
5.6	A single reconstructed slice showing two defect sites at the interface. Highly spherical porosity is also observed alongside SrCrO_4 particles (small & bright particles) and the CaSO_4 particles (large & grey particles.)	133
5.7	Segmentation of the phases for quantification.	133
5.8	Slices through the 3D image before (left) and after (right) leaching. Slices correspond to the same ROI as determined by 3D image registration.	134
5.9	SBFSEM data showing the depletion of clusters of SrCrO_4 by (a & b) holes as well as (c) shrinking cores; (d) contact points between clusters are also observed.	135
5.10	(a) SBFSEM data of the defect site. The transparent epoxy layer can be seen where the larger SrCrO_4 particles (red) and the voids (blue) are shown. (b) A close-up, rotated view of the largest void shown in (a), demonstrating the transition from SrCrO_4 to void.	136
5.11	Fractal dimensions of the largest inhibitor clusters as determined by the box counting method on the segmented sXRT data (a & b) and the 3View data (c & d).	138
5.12	The effective diameter distribution (a) and NN distribution (b) of the pores before (blue) and after (green) leaching.	140
5.13	The effective diameter distribution (a) and NN distribution (b) of the SrCrO_4 before (blue) and after (green) leaching.	141
5.14	The effective diameter distribution (a) and NN distribution (b) of the CaSO_4 before (blue) and after (green) leaching.	142
5.15	The PCFs for the CaSO_4 (a) and pores (b) before (blue) and after (green) leaching.	143
6.1	The methodology for producing the sintered joint material [3].	150
6.2	Monte Carlo simulation of the interaction volume in pure silver.	151
6.3	The reconstructed porosity for the as-sintered (left) and aged (right) solders. A single pore network shown in red is observed in both samples. Pore clusters shown in blue are quantified in isolation to observe size and spatial distributions of the unconnected porosity and its subsequent impact on performance. . . .	152
6.4	Wire-frame mesh of the pore-silver interface used for the FEA.	154
6.5	Scanning electron micrographs of the polished surface, highlighting the evolution of the porosity from the as-sintered specimen (a) to the aged specimen (b).	155

6.6	(a) The pore area fraction as a function of depth from the segmented volume; (b) the effective diameter distribution. The mean effective diameter is 95 nm for the as-sintered sample and 140 nm for the aged sample. Frequency is normalized with pore number density; (c) the NN distributions. For the as-sintered and aged samples respectively, the mean NN distances are 289 nm and 366 nm, and the clustering ratios are 0.9629 and 0.8773. The frequency is normalized with pore number density.	156
6.7	FFT of the area fraction data (figure 6.6a) revealing a dominance of the low spatial frequency of the pores in the aged specimen.	157
6.8	Effective diameters plotted against NN distances for each connected pore for the (a) as-sintered and (b) aged specimens. Plots are colour coded by sphericity.	158
6.9	Images showing the solution of the displacement field within sub volumes of the as-sintered (a) and aged (b) specimens. Pressure is applied along the positive x direction.	160
6.10	A combination of results for both the FE modelling and direct elasticity measurements plotting Young's modulus against pore fraction. The fit shows an agreement of the data with the proposed empirical model.	161
A.1	A small system of particles illustrating the calculated vectors in 2D.	169
B.1	The faces of an example mesh showing the applied boundary conditions. . . .	174
B.2	A mesh undergoing diffusion and coloured by normalized concentration. . . .	174
B.3	The sum of the element residuals plotted as a function of time step.	175
B.4	A plot of the global mesh concentration as a function of time time.	176
B.5	A plot of the concentration along a single axis of the data. Each plot is a differing time step showing the evolution of the concentration field over time. Distance is not scaled.	176

List of Tables

3.1	Characterization of particle distribution based on R_n	82
4.1	Variables and their definitions used in the NN code.	103
4.2	The shape and scale factors of the fitted PDFs alongside the number density, mean NN distances and clustering ratio R_n of the NN distributions for the low magnification 3View images.	116
5.1	Analytical models and their respective χ^2 values for the leaching data [4]. . .	129
5.2	The volume fractions of the respective segmented phases before and after leaching	136
5.3	The fractal dimensions of the largest clusters	137
6.1	Known physical parameters of pure silver.	153
A.1	Variables and their definitions used in the NN code.	168

Abbreviations

BF	Bright Field
BP	Back Projection
BSE	Backscatter Electron
CCD	Charge-Coupled Device
CCL	Connected Component Labelling
CG	Conjugate Gradient
CI	Corrosion Inhibitor
CSIRO	Commonwealth Scientific and Industrial Research Organisation
DB-FIB	Dual Beam Focused Ion Beam
DLS	Diamond Light Source
EBCM	Extended Boundary Condition Method
EDX	Energy-dispersive X-ray spectroscopy
ENSMA	École Nationale Supérieure de Mécanique et d'Aérotechnique
ESEM	Environmental SEM
FBP	Filtered Back Projection
FE(s)	Finite Element(s)
FEA	Finite Element Analysis
FEM	Finite Element Modelling
FIB	Focused Ion Beam
FIB-SEM	Focused Ion Beam Scanning Electron Microscope
FSL-SS	Femtosecond Laser Serial Sectioning
IBM(s)	Image Based Model(s) / Modelling
ID	Insertion Device
LILW	Low and Intermediate Level Waste
LVDT	Linear Variable Differential Transformer
MAPEM	Maximum A Posteriori Expectation Maximization

MLEM	Maximum Likelihood Expectation Maximization
NN(s)	Nearest Neighbour(s)
PALS	Positron Annihilation Lifetime Spectroscopy
PDF	Probability Density Function
RAM	Random Access Memory
ROI(s)	Region(s) Of Interest
SBFI	Serial Block-Face Imaging
SBFSEM	Scanning Block-Face Scanning Electron Microscopy
SCM	Shrinking Core Model
SEM	Scanning Electron Microscopy / Microscope
STL	STereoLithography
sXRT	synchrotron-XRT
TEM	Transmission Electron Microscopy
TMM	the T-Matrix Method
UV	Ultraviolet
XRT	X-Ray Tomography

UNIVERSITY OF MANCHESTER

Abstract

Surface integrity through tomographic reconstruction

Faculty of Engineering and Physical Sciences

School of Materials

Doctor of Philosophy

by James Andrew Carr

December 2014

The capability of high resolution, low energy backscattered electron microscopy has been extended to enable serial sectioning in the chamber of a conventional scanning electron microscope. For the first time, this technique, employed in a commercially available 3View facility, is used to reveal the structure of materials in 3D on the sub-micron scale. The distribution of pigments in protective organic coatings is quantified from the reconstructed 3View images and a correlation between spreadability and nearest neighbour distance of the pigment clusters is drawn. X-ray tomography is used to perform an ex-situ leaching experiment of a corrosion resistant organic coating. The depletion of inhibitor material after exposure to a corrosive environment is observed. The 3View is used to obtain additional images at higher resolution. The results indicate that inhibitor material is transported through pre-existing porous networks or through the porous networks that form following depletion of the material itself. Image based models of porous sintered silver films are produced from data obtained in the 3View facility which are used to validate the dependence of elasticity on the pore fraction.

Declaration

I, JAMES ANDREW CARR, declare that this thesis titled, 'SURFACE INTEGRITY THROUGH TOMOGRAPHIC RECONSTRUCTION' and the work presented in it are my own. I confirm that:

- No portion of the work referred to in the thesis has been submitted in support of an application for another degree or qualification of this or any other university or other institute of learning.
- This work was done wholly while in candidature for a research degree at this University.
- Where I have consulted the published work of others, this is always clearly attributed.
- Where I have quoted from the work of others, the source is always given. With the exception of such quotations, this thesis is entirely my own work.
- I have acknowledged all main sources of help.

Signed:

Date:

Copyright Statement

- i The author of this thesis (including any appendices and/or schedules to this thesis) owns certain copyright or related rights in it (the “Copyright”) and he has given The University of Manchester certain rights to use such Copyright, including for administrative purposes.
- ii Copies of this thesis, either in full or in extracts and whether in hard or electronic copy, may be made **only** in accordance with the Copyright, Designs and Patents Act 1988 (as amended) and regulations issued under it or, where appropriate, in accordance with licensing agreements which the University has from time to time. This page must form part of any such copies made.
- iii The ownership of certain Copyright, patents, designs, trade marks and other intellectual property (the “Intellectual Property”) and any reproductions of copyright works in the thesis, for example graphs and tables (“Reproductions”), which may be described in this thesis, may not be owned by the author and may be owned by third parties. Such Intellectual Property and Reproductions cannot and must not be made available for use without the prior written permission of the owner(s) of the relevant Intellectual Property and/or Reproductions.
- iv Further information on the conditions under which disclosure, publication and commercialisation of this thesis, the Copyright and any Intellectual Property and/or Reproductions described in it may take place is available in the University IP Policy (see <http://documents.manchester.ac.uk/DocuInfo.aspx?DocID=487>), in any relevant Thesis restriction declarations deposited in the University Library, The University Library’s regulations (see <http://www.manchester.ac.uk/library/aboutus/regulations>) and in The University’s policy on Presentation of Theses.

TO MY FUTURE BRETHREN IN THE MAGIC ART

May the instructions contained in this book be as profitable to them as the composition of those instructions has been pleasant to me.

- Robert-Houdin

Acknowledgements

Doing justice to this section, once I've overcome every other, seems much harder than I initially assumed it to be. The main issues appear to be the number of people to mention and the difficulty in subsequently avoiding either boredom or nausea . . .

I would firstly like to thank my supervisor Professor George Thompson for his continued support and advice. His experience, time and tireless enthusiasm throughout my candidacy has proved to be invaluable. I would also like to thank Professor Peter Lee for his expertise, insights and guidance.

To all of you lucky souls still at the Corrosion and Protection Centre, thanks for all the lunches, drinks and chats. They will be sorely missed. A special thanks to Teruo Hashimoto from whom I have learnt so much.

Thanks to everyone at the Manchester X-Ray Imaging Facility (MXIF) both in Manchester and on-site at Diamond Light Source (DLS) for their support, patience and technical know-how. This work was made possible in part by the facilities and support provided by the MXIF and the Research Complex at Harwell (RCaH), funded in part by the EPSRC (EP/I02249X/1).

To Christoph, Ulrich, Andy, Joan and Kaz, I couldn't ask for better people to work with during those long and drudging stretches of beamtime. I look forward to working with you all again soon.

Thanks to my collaborators: Brenda at Akzo-Nobel, Netherlands; Simon at Akzo-Nobel, UK; Tony, Adrian, Fiona and Sam at the Commonwealth Scientific and Industrial Research Organisation (CSIRO), Australia; Xavier and his research group at École Nationale Supérieure de Mécanique et d'Aérotechnique (ENSMA), France. I hope we can continue some of the great work we started over these past years.

To my friends and family who, willingly or not, shared in my struggle and who believed that I could do this more than I ever did: you were right. Happy now?

Thanks, finally, to my darling fiancé, Jess, who, of this entire body of work, cares only about these solitary lines of text. You've been my sanity, perspective and motivation. I don't know what I'd do without you.

For Jack and Jenna

The Author

James graduated with a degree in Physics (MPhys) (hons) from the University of Manchester in 2008 and returned in 2011 to begin a research career as a LATEST2 PhD Research Affiliate at the Corrosion and Protection Centre (CPC) within the School of Materials. His primary research goals are the investigation of the transport behaviour of corrosion inhibitors in self-healing coatings for aerospace applications. However, many other areas of interest have emerged since and during the course of his PhD. Since joining the CPC, James has also joined a network of imaging experts within the Manchester X-ray Imaging Facility (MXIF), which has facilitated a range of interdisciplinary work both inside and outside the university.

James has supported a number of his colleagues within LATEST2 in the area of imaging for the purpose of characterization and quantification of light alloys and coatings for automotive and aerospace applications. Interests in the area of 3D imaging has also led to collaborative efforts in other fields beyond corrosion and materials science. He has extensive experience as part of the experimental teams at I13 imaging beamline at DLS and has delivered training in tomographic reconstruction methodologies as well as 3D image analysis.

James has co-authored a number of publications listed below:

Liu, Y., Zhou, X., Carr, J., Butler, C., Mills, S. L., O'Connor, J., McAlpine, E., Hashimoto, T., Zhong, X., Thompson, G. E., Scamans, G. M., Howe, P., McCool, M. A., Malone, N. S., 2013. Visualisation of conductive filler distributions in polymer composites using voltage and energy contrast imaging in SEM. *Polymer*, 54(1), pp.330.

Thompson, G. E., Hashimoto, T., Zhong, X., Curioni, M., Zhou, X., Skeldon, P. R., Withers, P. J., Carr, J. A., Monteith, A. G. 2013. Revealing the three dimensional internal structure of aluminium alloys. *Surface and Interface Analysis*, 45(10), pp.1536.

Trueman, A., Knight, S., Colwell, J., Hashimoto, T., Carr, J., Skeldon, P., Thompson, G. E., 2013. 3-D tomography by automated in situ block face ultramicrotome imaging using an FEG-SEM to study complex corrosion protective paint coatings. *Corrosion Science*, 75, pp.376.

Hughes, A. E. Trinchi, A. Chen, F. F. Yang, Y. S. Cole, I. S. Sellaiyan, S. Carr, J. Lee, P. D. Thompson, G. E. Xiao, T. Q., 2014. Revelation of Intertwining Organic and Inorganic Fractal Structures in Polymer Coatings. *Advanced Materials*.

Hughes, A. E., Trinchi, A., Chen, F. F., Yang, Y. S., Cole, I. S., Sellaiyan, S., Carr, J., Lee, P. D., Thompson, G. E., Xiao, T. Q., 2014. The application of multiscale quasi 4D CT to the study of SrCrO₄ distributions and the development of porous networks in epoxy-based primer coatings. *Progress in Organic Coatings*.

James has also authored the submitted manuscript:

Carr, J. A., Milhet, X., Caccuri, V., Hashimoto, T., Thompson, G. E., Boyer, S. A. E., Gadaud, P., Gerland, M., Lee, P., (submitted). Quantitative Characterization of Porosity and Determination of Elastic Modulus for Sintered Micro-silver Joints

Chapter 1

Introduction

Tomographic imaging is perhaps one of the most direct and powerful methods for the characterization and modelling of materials. The representation of objects in 3D is easy to interpret and provides an ability to obtain qualitative as well as quantitative information. In contrast, quantitative information obtained from *2D images* must necessarily rely on either statistical approximations to certain distributions (e.g. size) or limiting assumptions concerning the geometry of certain features (e.g. shape, spatial distribution). Tomographic imaging allows full quantitative characterization of materials without the necessity for *a priori* information of the material.

The unifying theme of the work presented herein is the application of a new 3D imaging facility to the characterization and modelling of materials. The method of such image acquisition is known generally as Serial Block-Face Imaging (SBFI). A review of the history of SBFI is provided in section 2.4.3, which is well placed within the descriptions of traditional tomographic techniques documented in Chapter 2. Serial Block-Face Scanning Electron Microscopy (SBFSEM) is a form of SBFI which has been implemented in the commercially available 3View[®] facility [5]. Such a facility provides the ability to automatically section materials within the chamber of a Scanning Electron Microscope (SEM) allowing the 3D structure of materials to be revealed at unprecedented length scales. Both the strengths and limitations of the technique will be explored in terms of competing or complimentary experimental techniques detailed in Chapter 2.

On acquisition of a 3D image, there are a very large number of operations one can perform depending on the intended aim of the investigation. This extensive post-acquisition workflow and the associated methodologies for quantifying and modelling the tomographic data are detailed in Chapter 3.

Three materials are investigated to provide the necessary substance for evaluation of the technique. Owing to the diverse nature of the materials investigated, chapters 4 to 6 each

provide background to the materials and associated aims of the investigations. As such, each of these investigations can be considered self-contained and not explicitly related with the exception of the common technique used to investigate the materials.

Chapter 4 is concerned with the nanometre structure of paints and how 3D imaging can be used to understand how this structure relates to macroscopic properties. The relationship between spreadability and the spatial distribution of pigment dispersed in the paint is explored. A review of light scattering theory precedes the presentation of the results. This is done with the anticipation that simple analytical models, based on the quantitative 3D information obtained by SBFSEM, can be developed to more efficiently predict the behaviour of visible light in the medium. An alternative technique is used to validate the data obtained by SBFSEM in addition to providing multi-scale information regarding the size, shape and spatial distributions of the pigment.

Chapter 5 builds on previous work undertaken in the field of self-healing organic coatings for aerospace applications. The sub-micron structure of the coatings are observed using SBFSEM following an ex-situ tomography experiment involving the egress of corrosion resistant material from the coating. Problems associated with performing X-Ray Tomography (XRT) on the coatings are overcome by tuning the beam energy from the synchrotron source. Thin-slice Transmission Electron Microscopy (TEM) and Energy-Dispersive X-ray spectroscopy (EDX) were used in combination to determine how the material travels through the epoxy matrix of the coating.

Chapter 6 is concerned with how SBFSEM can be used to evaluate and model the mechanical properties of materials. A new joining technology used for die bonding is examined and the impact of the porous structure on the elasticity of the material is modelled. The effect of ageing on the porous structure is characterized and quantified to provide information on the material life cycle.

Chapter 2

Digital Imaging Techniques

2.1 Introduction

This chapter will describe the experimental techniques used to acquire images for the investigations documented in the following chapters. There is a predominant focus on 3D imaging (section 2.4), but it will also be necessary to document other experimental techniques. These are used either as supporting or auxiliary data (section 2.2) together with sample preparation techniques employed in advance of image acquisition (section 2.3).

In sections 2.4.1 and 2.4.2, it is the author's intention to describe 3D imaging in general terms. As such, the following should be congruent with a description of forming any kind of digital image be it with ions, neutrons, photons, electrons or any other 'signal'. This is to maintain an overarching appreciation for digital imaging and what constitutes a digital image, which will be pertinent to Chapter 3 where details of processing tomographic data-sets will be explored. The meaning of a digital image, however, will ordinarily rely on the means by which the image was acquired, i.e. the specific kind of signal used. For this reason, applied examples follow this high level description to serve as a means of interpreting digital images typically produced in materials science research.

In section 2.4.3, a review of the literature predominantly focused on SBF1 is presented, which provides a summarizing, chronological description of the emergence of this imaging technique and its limitations. This is followed by a review of contemporary 3D imaging capabilities in section 2.4.4. Specific kinds of 3D imaging to be used in the following chapters will then be detailed in sections 2.4.5 and 2.4.6.

2.2 2D Imaging Techniques

Characterization of materials has long since been dominated by 2D imaging. This section will briefly describe well established 2D imaging techniques, which will also be relevant to

the following sections concerning 3D imaging.

2.2.1 Scanning Electron Microscopy

The Scanning Electron Microscope (SEM) utilizes a beam of electrons which scans or ‘rasters’ the sample. As the beam passes over the sample, many interactions can take place as shown in figure 2.1 [1, 6]. Primarily, the SEM will look at backscattered electrons (BSE) and/or secondary electrons although it is not possible to completely isolate the detection of either of these classifications of signal [1]. This broad categorization of detected signal is, however, useful in terms of what is of interest to the microscopist, i.e. atomic density or topology.

Secondary electrons are low energy scattered electrons, which are detected by an Everhart-Thornley detector [7]. The detector accelerates the electrons towards a scintillator, which generates a signal that can then be amplified and stored to compose an image. Due to their low energy, secondary electrons originate from very near the surface of the sample and, therefore, provide good topological information such that high surface gradients* will produce high signals. Surface gradients that are normal to the incident beam will, conversely, produce low signals.

*That is to say surface gradients that are close to the incident beam angle.

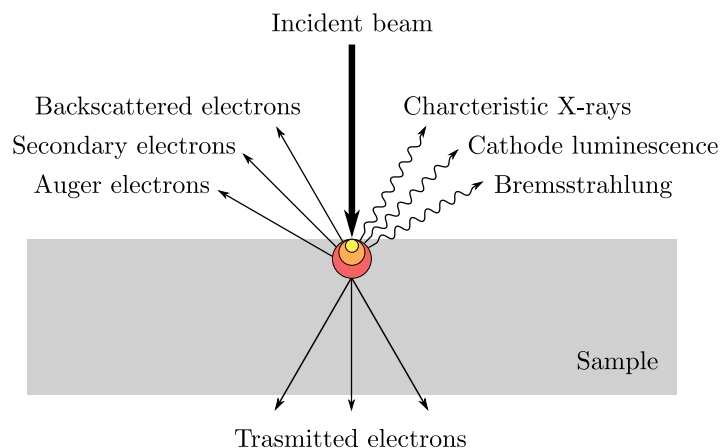


FIGURE 2.1. The interactions that can result from an incident beam of electrons [1].

BSEs are elastically scattered electrons, which are detected either by scintillator based or solid-state based detectors positioned such that the incident beam passes through the detector. This positioning is to ensure the majority of the BSE flux is captured. BSEs give atomic density information such as that high atomic density will produce higher energy BSEs and, therefore, a higher signal and vice versa.

BSEs can be captured by the secondary electron detector and, therefore, it is possible to achieve atomic density information using only this kind of detector, but the low flux of BSEs in the position of the secondary electron detector will often significantly reduce the signal to noise ratio [6].

2.2.2 Transmission Electron Microscopy

A TEM will utilize the transmitted electrons depicted in figure 2.1 to form either a diffraction pattern or an image. TEM specimens are sufficiently thin ($\sim 10 - 100$ nm) to allow the electron beam to penetrate completely through the sample. The signal detected is formed as a result of the various kinds of scattering that take place within the sample [1]. In bright field (BF) mode, the image formed is representative of atomic density in a similar fashion to BSEs in the SEM. However, compared to the SEM, the signal is inverted such that high atomic densities will produce low signals.

2.2.3 Energy-Dispersive X-ray Spectroscopy and Other Signals

As shown in figure 2.1, there are a variety of other interactions that can be used to provide additional information. These other interactions are summarized in figure 2.2, which provides a more detailed mechanistic view of the interactions generated from a beam of electrons incident on a material.

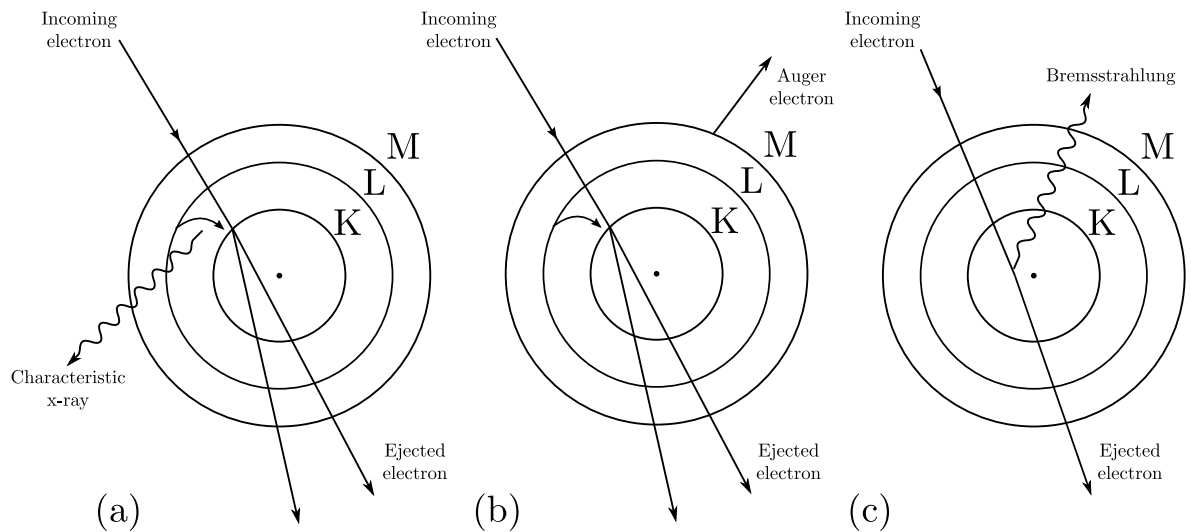


FIGURE 2.2. A more detailed explanation of the electron interactions from an atomic perspective [1].

Of most interest to the author is situation (a) in figure 2.2, where an incoming electron knocks an electron out of an inner orbital and ejects it, thus leaving an electron hole [8]. The atom, now in an excited state, will then emit a characteristic X-ray due to an electron transition from a higher orbital to fill the electron hole. This characteristic X-ray will have an energy that is equal to the difference of energy states of the atom and, therefore, is unique to the atom involved. This implies that detection of X-rays in an electron microscope has scope to provide elemental information. This kind of measurement is widely known as Energy-Dispersive X-ray spectroscopy (EDX) [1]. The effect described above can also take place by knocking out electrons of higher orbitals, which are spaced closer together. Therefore, the energy of the emitted photon is reduced and falls within the range of visible light producing an effect called cathodoluminescence.

Instead of emitting a characteristic X-ray, it is also possible for an outer electron to be emitted following the knocking out of an electron [9, 10]. This emitted electron is known as an Auger electron and is depicted in figure 2.2(b). The energy of the Auger electron is equal to the difference of the two excitation states of the atom, i.e. the same as the aforementioned characteristic X-ray.

In figure 2.2(c), an effect known as Bremsstrahlung is the excitation of an atom without the knocking-out of an electron. Although not detected in isolation, it contributes to all spectra received through EDX. Essentially Bremsstrahlung is the result of the acceleration of the electron as it passes an atom due to the interaction of the electromagnetic fields of the charged bodies. The energy values are not discrete as is the case for characteristic X-rays and Auger electrons, and can be seen as a ‘background’ signal in EDX spectra.

2.3 Sample Preparation

2.3.1 Ultramicrotomy for SBFSEM

Sample preparation for SBFSEM involves the use of an ultramicrotome to produce a tip on the sample so that the in-situ ultramicrotome used in the facility can adequately slice the block-face of the sample. A set-up of the ultramicrotome system used is illustrated in figure 2.3. Figure 2.3(a) displays a view from above the system, showing the sample and the blade position at an angle to the sample to allow the production of a tip. The blade used can be a glass or diamond knife, which depends strongly on the sample material. Figure 2.3(b) displays a side view of the system, demonstrating the motion of the sample holder. The blade remains stationary while the sample moves progressively further forward after systematically removing thin slices from the sample due to the illustrated rocking motion of the sample holder. Figure 2.3(c) shows the final appearance of the sample itself with indicated dimensions suitable for the 3View system.

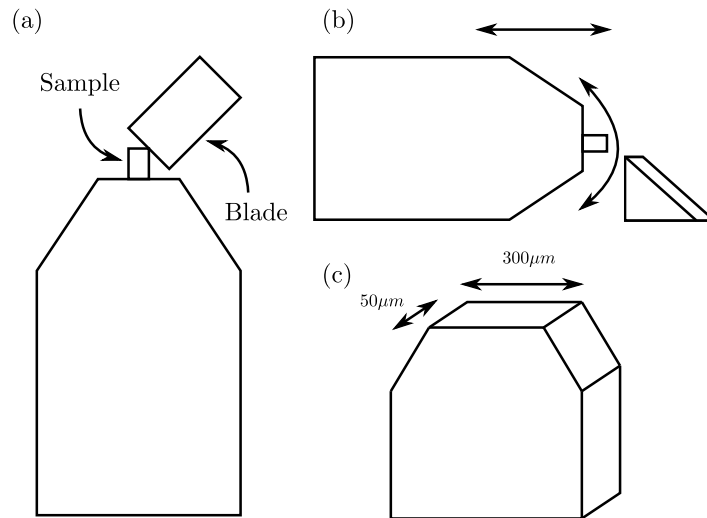


FIGURE 2.3. (a) A view of the ultramicrotome from above. The sample moves in and out of the page to allow the blade to slice the sample. (b) A view from the side showing the motion of the sample in the holder against the blade. (c) The final dimensions of the sample ready for scanning.

2.3.2 FIBSEM Sample Preparation

To facilitate the reduction of charging [11] of non-conductive samples in a Focused Ion Beam SEM (FIBSEM), it is necessary to provide a conduction route to ground. This is achieved by first mounting the sample on a metallic stub using silver paste as an adhesive. The mounted sample is then gold sputter coated [12] so that a conductive layer covering the entire surface of the sample is formed. In addition, within the FIBSEM itself, there is a facility to deposit a platinum layer over the region of interest. The platinum layer also helps protect the internal structure of the sample from excessive damage under FIB irradiation.

2.3.3 Ultramicrotomy for TEM

Ultramicrotomy is a technique used for producing thin ($\sim 10\text{nm}$) slices of material for investigation in a TEM [13–16]. The primary motivation is to provide a significant flux of transmitted electrons through the material. Initially, the sample is ultramicrotomed to produce a tip as described in section 2.3.1. Typically, thin slices are produced and collected from a water bath situated next to the diamond knife. Rather uniquely in this case, due to

the solubility of certain phases within self healing coatings (see Chapter 5), thin slices are produced and collected in a *dry* environment. This is to keep water soluble particles intact for examination in the TEM.

2.4 3D Imaging

This section will summarize the 3D image acquisition techniques used by the author to obtain data on the internal structure of materials under investigation. Firstly, a distinction between two broad categories of 3D imaging should be drawn to illustrate the contrasting methodologies and consequential limitations of these techniques. These categories are known as SBFi and tomography. It is not unusual for SBFi to be considered a form of tomography, but it will become apparent that it differs dramatically from any other form of 3D image acquisition in terms of how the 3D volume is assembled. In brief, the fundamental difference being that traditional tomography utilizes a signal *transmitted* through a specimen and SBFi utilizes a signal *reflected* from the surface of a specimen.

2.4.1 Tomography

Tomography involves the acquisition of projections, which are formed by an attenuated signal at a detector after transmission through a specimen (figure 2.4). Projections are 2D representations of 3D objects that are analogous to shadows cast by an object in visible light. Contrary to visible light incident on opaque objects, sources such as X-rays, electrons, gamma rays, radio waves etc. can penetrate and transmit through most materials. This allows a projection to have variation in signal intensity within the region enclosed by the surface of the specimen. This contrast is due to intensity variations in the attenuated signal resulting from the material absorbing or, otherwise, scattering the signal away from the detector.

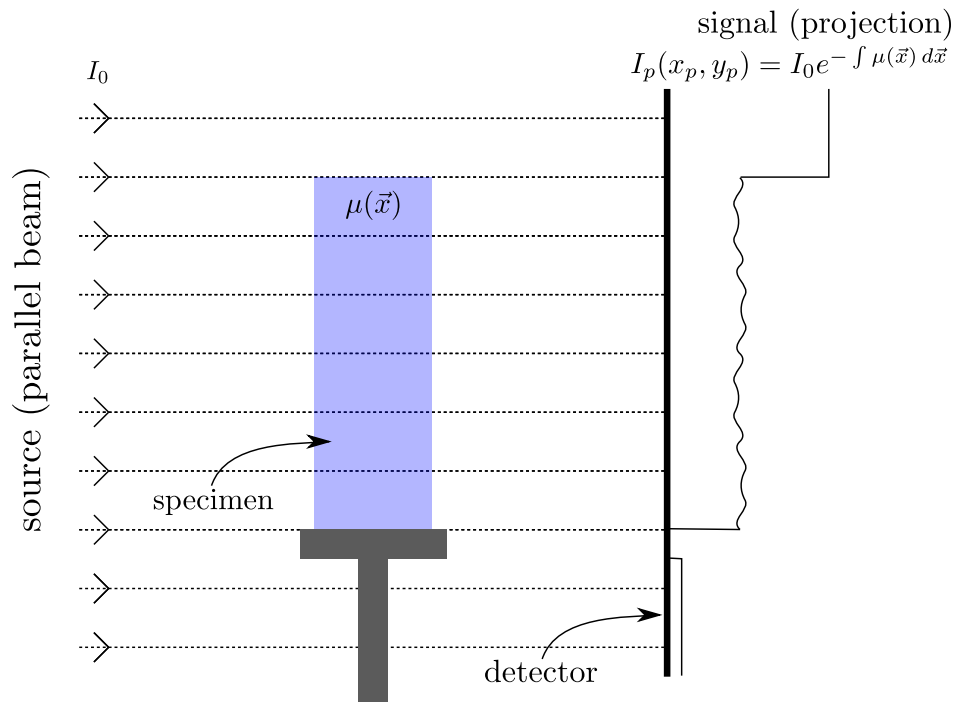


FIGURE 2.4. Schematic of a typical tomography setup for a parallel beam.

An extrapolation of the Beer-Lambert law [17–19], which describes how visible light is absorbed by homogenous materials can be applied more generally to heterogeneous materials exposed to some penetrating source. This is achieved by assigning an absorption coefficient field, $\mu(\vec{x})$, to the specimen, which quantitatively describes the amount by which the specimen absorbs the signal at a position, \vec{x} .

In the trivial case where this field, $\mu(\vec{x})$, and the source intensity, I_0 , are known, then the intensity, $I_p(x_p, y_p)$, on the projection space can be calculated by taking the line integral from the signal source to this point as shown in figure 2.4.

$$I_p(x_p, y_p) = I_0 e^{-\int \mu(\vec{x}) d\vec{x}} \quad (2.1)$$

Projections are simply continuous 2D arrays of these integrals, which give information about how much signal the specimen has absorbed along the direction between the source and the detector. In reality, projections are captured digitally and so the continuous nature of the

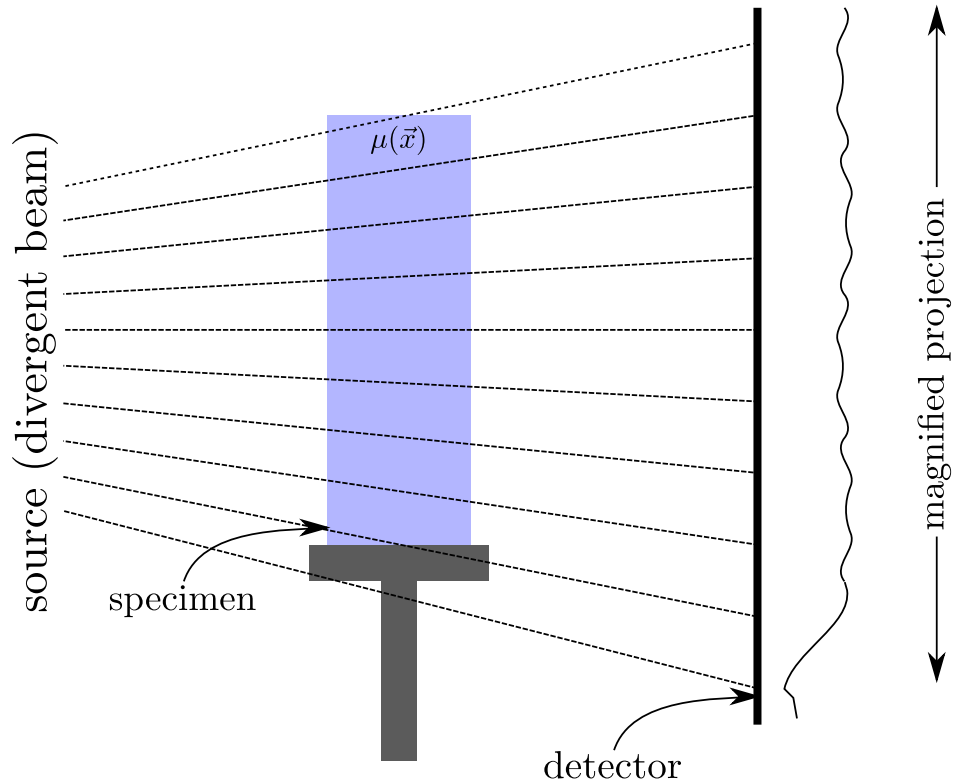


FIGURE 2.5. Schematic of a typical tomography setup for a ‘divergent’ or ‘cone’ beam. The magnification of the projection is due to the divergent source.

intensity variations becomes discrete. Formally, this is achieved by taking an average intensity across the surface of a pixel for dimensions, l_p , so that the actual projected image, $I_p(x_p, y_p)$, is converted to a digital projection, $I_p(i, j)$, in the following manner:

$$I_p(i, j) = \frac{1}{l_p^2} \int_{(i-1)l_p}^{il_p} \int_{(j-1)l_p}^{jl_p} I_p(x_p, y_p) dy_p dx_p \quad (2.2)$$

where i and j correspond to the discrete positions on some digital image detector, for example a Charge-Coupled Device (CCD), a schematic of which is shown in figure 2.6. This is known formally as the discretisation of the projection intensity. It is noted that equation 2.1 is valid only for situations where the source signal is a parallel beam. It is possible to generate analogues to the above for divergent source beams (see figure 2.5), where one must consider line integrals that are not parallel to the aforementioned case due to contributions of intensity from regions that are not directly in line with the source and the detection point.

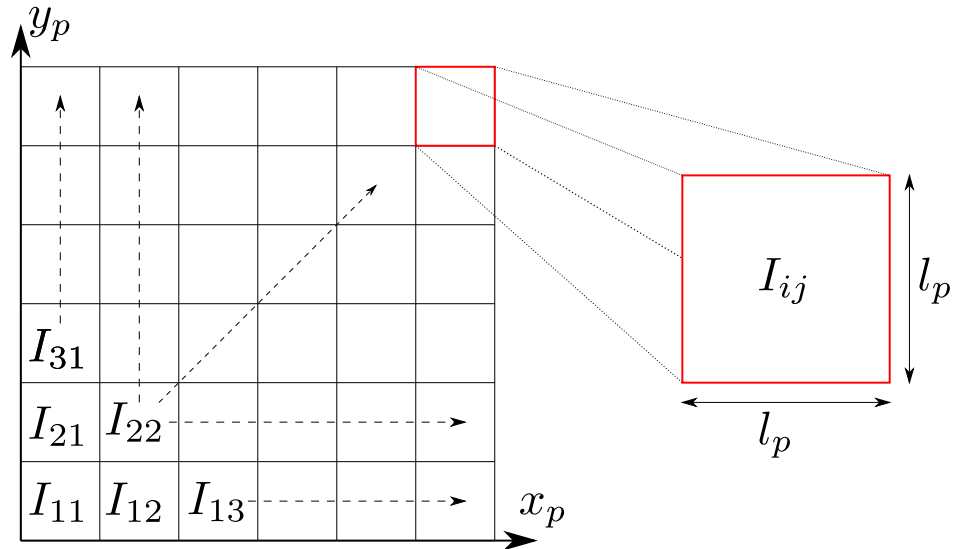


FIGURE 2.6. Discretisation of the projection intensity distribution on the projection space defined by (x_p, y_p) .

In the non-trivial case where there is an unknown material being investigated, a number of projections can be taken whilst rotating the specimen in the beam or, equivalently, rotating the source and detector around the specimen. Spatial information about $\mu(\vec{x})$ along all three dimensions can be obtained through an inverse transformation known as tomographic reconstruction to form a 3D image of the specimen. This image is in essence a 3D array of values that are the average discretised absorption coefficients (or some function of the absorption coefficients) of the sample. Tomography, as described above, is a non-destructive imaging technique used to observe the internal structure of a sample by producing contrast differences in 3D space from a series of digitally reconstructed 2D projections. This 3D space consists of voxels which take on digital values that are a function of the absorption or phase differences of the signal in the sample.

2.4.2 Serial Block-Face Imaging

The word ‘tomography’, from the Greek *tomos* meaning “slice” and *graphō* meaning “write”, is rather paradoxically reserved for techniques that involve no slicing whatsoever. Tomography is a non-destructive technique that involves the utilization of a signal *transmitted* through

a sample to form projections which are then reconstructed to form a 3D array of voxels. SBF, on the other hand, does involve slicing and utilizes a signal *reflected* from the sample surface. Like tomography, the reflected signals form a 2D image, but the image is formed as a result of interactions of the signal near the surface such that the signal is a representation of a volume bounded by the surface of the sample and a depth below that surface, known as the ‘interaction volume’. This is very much in contrast to the raw data produced via traditional tomographic techniques that are 2D projections of the entire sample volume.

Because reflected signals are achieved from interactions near the surface of the sample, a series of images can be formed by systematically removing the surface layers between scans. This technique, unlike tomography, is destructive so that the sample being imaged is systematically destroyed during the process of writing the 3D image. It is critical to ensure that, during imaging, the interaction volume near the surface of the sample involved in creating the image must not exceed the slice thickness. That is to say, the slice thickness should not be less than the penetration depth of the signal.

Reconstruction for SBF is trivial in comparison to tomography as it simply involves stacking a series of 2D reflected images that represent the internal structure of the specimen along a single axis to provide the extra dimensionality to the image. Like tomography, this technique produces a 3D space consisting of voxels, which take on varying contrast values. However, these values are a function of the reflected signal interactions (as discussed in section 2.2) at each surface of the sample between slices. Reconstruction of these kinds of images is, therefore, much more intuitive and requires significantly reduced computing power to produce when compared to tomography.

2.4.3 Serial Block-Face Imaging: A Review

2.4.3.1 Introduction

Developments in SBFI have progressed significantly in resolution, efficiency and effectiveness of reconstruction since its early application. DeHoff [20] identified the strengths of the technique, which allowed for quantification of geometrical quantities previously unavailable to 2D and stereoscopic techniques. Information such as connectivity of phases and features in 3D, volumetric density of particles, spatial distribution, and true 3D shape are clearly very useful quantities that are only available by analysing 3D image datasets. Techniques previously undertaken by Mangan et al. [21], Worlfsdorf et al [22] and Li et al [23, 24] utilised manual serial sectioning methods to achieve 3D image datasets. Alkemper and Voorhees [25] have reviewed these techniques highlighting the limitations in the speed of image acquisition as well as consistency in the sectioning despite the prediction that automated sectioning would be developed [20].

2.4.3.2 Automated serial sectioning

Alkemper [25, 26] notes that typical timescales for the acquisition of around 100 manual serial sections can fall in the range of weeks and that problems occur with image alignment and the precision of the section thickness. Alkemper's papers first describe a technique where a sample is automatically translated between a digital optical microscope and a milling machine allowing tens of images to be acquired per hour, thus drastically reducing the acquisition time. Consistency in section thickness is also improved by fixing step sizes of the milling machine, allowing resolutions of up to 1 μm in the milling direction. Limitations associated with alignment along the image plane are addressed by implementing a Linear Variable Differential Transformer (LVDT) to provide recorded information about the displacement of the sample

between images. The Micromiller method described by Alkemper provides resolutions in the planer directions of 0.96 μm and variations in milling step size due to temperature variations of approximately 2% with sectioning thicknesses between 1-20 μm .

At the same time, alternative techniques for performing serial sectioning were being developed and include the use of a VCR Dimpler [27], milling [25, 26], polishing with fiducial marking [28], and ultramicrotoming [29]. Spowart et al [30] first published details of an automated serial sectioning device utilizing a polisher and optical microscope called Robo-Met.3D. The sample is mounted on a robotic arm, which moves the sample between a polisher, an automatic etching station and an optical microscope. In terms of section thickness, the Robo-Met.3D improves on the Micromiller by a factor of 10, achieving sections down to 100 nm thick with deviations of around 4% due to variations in polishing time, load applied by the arm, angular speed of the polisher and heterogeneity in the sample.

2.4.3.3 Limitations of SBF I

In reviewing the contemporary automated serial sectioning techniques, i.e. Micromiller and Robo-Met.3D, Spowart [31] suggests that competition between SBF I and other techniques which do not destroy the sample in the process will not be well matched. Techniques such as high resolution XRT [32, 33] at the time could produce resolutions (up to 1 μm) comparable to the Micromiller and the Robo-Met.3D (up to 0.1 μm), and were not destructive thus allowing for repeatability or dynamic studies (so called ‘4D image datasets’). Similarly, 4D image datasets can also be produced using synchrotron-XRT (sXRT) such that real time 3D images of evolving microstructures can be obtained. This is advantageous for studying recrystallization and other dynamic processes concerning the evolution of the granular structure of polycrystalline materials [34, 35]. Principally, it is the destructive nature of SBF I that is the main limitation for Spowart when making this comparison and, along with comparable

spatial resolution limits ($\sim 1 \mu\text{m}$), XRT does appear to be the superior technique. It is worth noting, however, that Robo-Met.3D and FIBSEM [36] respectively have spatial resolution capabilities of one and two orders of magnitude better than micro-XRT.

2.4.4 Contemporary Capabilities of 3D Imaging

Current resolution capabilities of XRT and SEM instrumentation have advanced well beyond that documented by Spowart [31, 37]. Nano-XRT lab-based equipment is now commercially available at resolutions of 50 nm [38, 39], whereas previously these resolutions were only available with synchrotron X-ray nanotomography [40–42]. However, synchrotron X-ray nanotomography experiments are currently achieving resolutions approaching the sub 10 nm range by improving the optical properties of the lenses in the rigs used on the synchrotron beam lines [40–42].

Advances in SEM resolution have also facilitated an increase in the capabilities of SBFSEM, but this also necessitated the requirement for more refined and precise sectioning techniques. Early examples of automated SBFSEM [43] used an in-situ ultramicrotome to section the specimen in the chamber of an SEM; however, the materials suitable for such a technique were limited due to charging effects [5] as well as the limited capabilities of automating the sectioning and image acquisition with computers [44]. More recently, Femtosecond Laser Serial Sectioning (FSL-SS) has been utilized to section samples mounted on a programmable stage which can translate the sample between a high pulse rate laser used for sectioning and either an optical or SEM imaging rig [45]. The laser is capable of removing material many orders of magnitude faster than a FIB or mechanically with an ultramicrotome without significant heat damage but it does produce a roughness on the sample of around 100 nm [45], therefore, limiting the feasibility of this technique for the automated sectioning of samples for high resolution imaging.

Requirements in the biological sciences for high resolution 3D imaging of small cellular structures and complete neuronal circuits over tens of microns [44, 46] have led to the development of the 3View [47], an Environmental SEM (ESEM) with an in-situ ultramicrotome. The problems associated with automated in-situ serial sectioning in an SEM are overcome by implementing an ESEM to avoid sample charging [1] as well as providing bespoke software as a plug-in for Digital Micrograph [48] for automating the serial sectioning and image acquisition process. Since Macke and Denk [44, 46], the technique has widened its application to Materials Science first published by Zankel [5] where its feasibility for composite materials, paper and botanical specimens was demonstrated. The 3View has been demonstrated to achieve resolutions on the block-face of 5.6 nm when used with an FEI Quanta 250 FEG-ESEM at 2 keV and has the capability to slice at 2.5 nm [49]. This allows very high resolution 3D image datasets that are tens of microns large giving the 3View a marked advantage in terms of resolution and sample volume over even the best synchrotron X-ray nanotomography.

2.4.5 X-Ray Tomography

XRT is the application of tomography as discussed in section 2.4.1, using X-rays as the penetrating signal. XRT can be performed using lab or synchrotron sources of X-rays and it is here that an overlap with section 2.2.3 can be found. Lab sources utilize the emission of characteristic X-rays by the excitation of elements by electron irradiation. The energy of such X-rays is discrete in nature as they correspond to the energy levels within the element used as the ‘target’. In synchrotron sources, however, a continuous energy spectra of X-rays can be produced by an Insertion Device (ID).

The layout of I13-Imaging beamline at DLS is depicted schematically in figure 2.7. It shows the ID at the leftmost side of the illustration. The ID produces X-rays by ‘undulating’ or

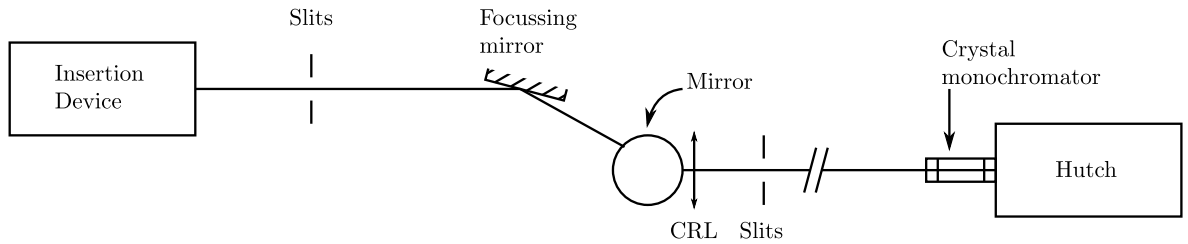


FIGURE 2.7. Layout of I13-Imaging beamline at DLS

‘wiggling’ the electron beam within the storage ring. The motion of the electrons, i.e. their acceleration, is responsible for spontaneous emission of high energy photons via Bremsstrahlung. These X-rays travel along the beamline through an arrangement of slits, mirrors and lenses that result in a parallel beam of X-rays being produced in the hutch where the experimental rig is set up. The monochromators are responsible for selecting the desired energy of the X-ray beam, making synchrotron radiation a highly versatile source for XRT.

2.4.6 Serial Block-Face Scanning Electron Microscopy

SBFI involves the imaging of the surface of a sample whilst systematically removing thin layers from the surface to create a stack of 2D images. This section will only discuss electron imaging based systems known as SBFSEM, due to the length scales necessary to perform adequate imaging of the internal structure of the materials under investigation ($<1 \mu\text{m}$). The aforementioned series of surface removals or ‘serial sections’ can be achieved by using an in-situ ultramicrotome or FIB both of which are discussed herein.

2.4.6.1 3View

Serial sectioning has been implemented in the Gatan 3View system [47], which is illustrated in figure 2.8. The 3View rig consists of a stage, which can be shifted in the z -direction to very high precision ($\sim\text{nm}$), and a diamond knife, which moves parallel to the xy -plane. The prepared sample can then be mounted within the system and the SEM focused. Once an

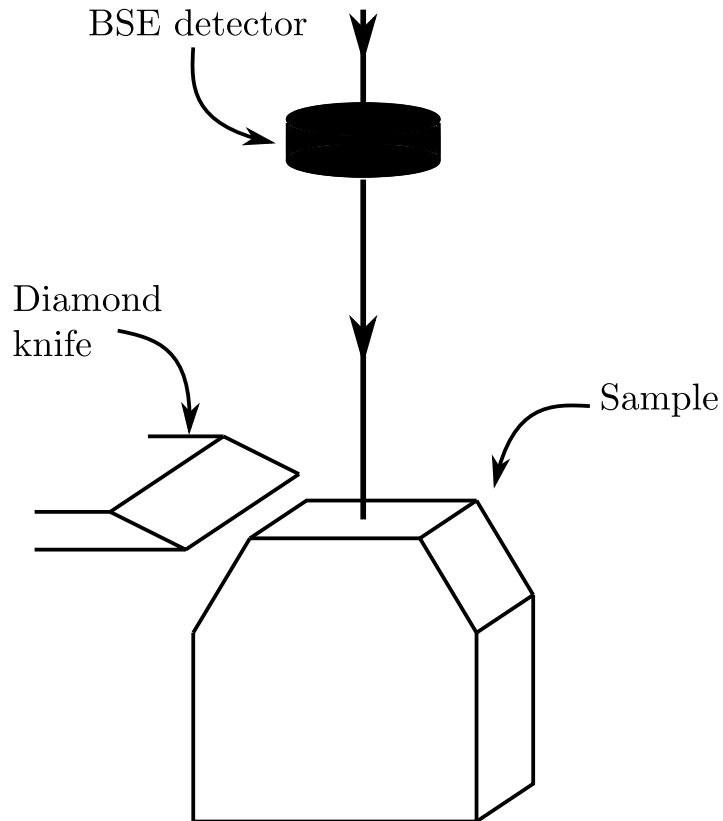


FIGURE 2.8. A schematic diagram of the 3View facility.

initial SEM is acquired of the block-face, the sample is then raised by the stage and the diamond knife moves along to cut a slice off the block-face before the stage returns to the image plane for the SEM to acquire the subsequent image in the series.

The 3View is used within an ESEM chamber, which makes the instrument ideal for non-conductive samples susceptible to charging under an electron source such as biological specimens but also paints which are primarily non-conducting. The 3View provides a means of very quickly producing 3D volumes with resolutions of up to 10 nm along all 3 spatial axes and Regions Of Interest (ROI) of up to 40 μm in the image plane (x & y axes) and several millimetres along the cutting axis (z axis) [49]. High resolution lab-based nano-XRT has resolutions of up to 50nm, whereas the 3View resolution is around 5 times higher depending on the SEM used to host the stage. Additionally, scan times are a few hours instead of a few days for high resolution settings. The disadvantage is that the technique is destructive and, therefore, repeatability is lost. Additionally, the fact that between imaging the sample

is being mechanically sliced can present problems in validating the correspondence between the sample and the image itself.

2.4.6.2 FIBSEM

A Focused Ion Beam (FIB) can be used to perform serial sectioning in a FIBSEM.[†] A schematic of the inside of a FIBSEM chamber is shown in figure 2.9. The left image depicts a prepared sample (as described in section 2.3.2) at coincident height within the FIBSEM chamber. Coincident height is achieved by adjusting the height and tilt of the stage such that the SEM and FIB are focused at the same point on the sample. It is also necessary to deposit a layer of platinum above the ROI and to mill ‘trenches’ to expose the block-face as depicted on the right image of figure 2.9.

Serial sectioning with a FIB is often more reliable than sectioning with an ultramicrotome in terms of mechanical deformation but also in terms accuracy of the section thickness.

[†]Also known as a Dual Beam-FIB (DB-FIB).

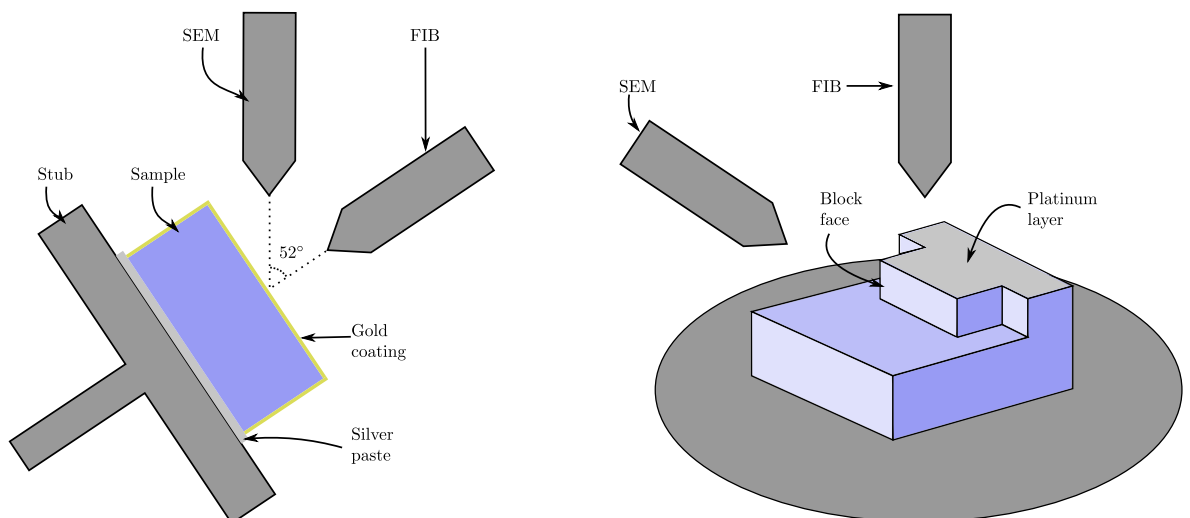


FIGURE 2.9. A schematic of a typical FIBSEM facility.

2.5 Concluding Remarks

This chapter has presented a summary of the experimental techniques used to observe the microstructure of materials under investigation including a review of SBF. The 3View system and I13-Imaging beamline at Diamond have been utilized predominantly, but often validation using other methods is necessary to achieve additional or supporting information.

With respect to determining the best technique, there are many other factors to consider. It is found (see chapter 4) that mechanically slicing certain kinds of samples can create significant deformation in individual samples. Performing nano-XRT was also not ideal as significant exposure to X-rays deformed the sample to the point where no reconstruction could be performed. FIBSEM was found to circumvent both issues for this particular investigation. Furthermore, in Chapter 5 the dynamics of a system were under investigation such that a non-destructive technique (synchrotron-XRT) was the best imaging technique.

In the following chapter, the author will describe the handling, processing and analysis of the data generated from these experiments.

Chapter 3

Quantitative Characterization for Tomographic Imaging

3.1 Introduction

This chapter will detail various methodologies that are employed by the author in the post image acquisition stage, which naturally follows on from the previous chapter concerning image acquisition itself. The concept of a 3D digital image will be formally introduced so that an understanding of the operations that act on images can be appreciated. Following this section, the formation of representative 3D digital images in the post acquisition stage of both tomography and SBFIT that is often referred to as ‘tomographic reconstruction’ is discussed. This is the process by which raw data from 3D image acquisition facilities can be converted into a 3D image that represents the scanned specimen. The formalism concerning filters and how they operate on images will be explored as well as their impact on further stages of the image processing work-flow (see figure 3.1). The process of selecting regions within an image, known as ‘segmentation’, are elucidated for the purposes of the latter stages of the work-flow. ‘Quantification’, that is to say the derivation of quantitatively meaningful information concerning the geometry of segmented images, will be described. In some cases, segmented images are used to perform Image Based Modelling (IBM) using the Finite Element Method (FEM), also known as Finite Element Analysis (FEA). This is where the equations governing some physical mechanism of interest are solved across small elements which collectively compose the 3D structure of the image. The precursor for FEM, therefore, is the generation of Finite Element (FE) meshes which are also briefly described. Finally the impact of using discrete images on the ability to adequately resolve features of interest is discussed.

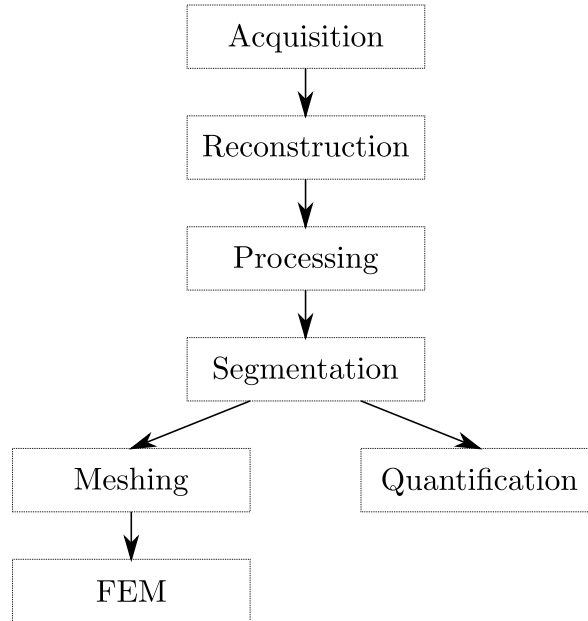


FIGURE 3.1. A high level overview of the work-flow for tomographic datasets.

3.2 3D Images

For the purpose of this work, a 3D image, in its most general form, is some representation of an object in 3D space. In principle, it is possible to describe an object using some mathematical function, $O(\vec{r})$, which corresponds to the positions of some physical parameters (e.g. density) in the object. In practice, this function is never known: the aim of 3D imaging, therefore, is to produce a multidimensional array of values that approximates a discretized form of this idealized equation. This multidimensional array, I_{ijk} , is equivalent to a digital 3D image where a value located at an index, (i, j, k) , corresponds to a physical location in the object [50–52]. On a very high level, therefore, digital 3D image acquisition can be described as the following:

$$O(\vec{r}) \xrightarrow{\text{acquisition}} I_{ijk} \quad (3.1)$$

3.2.1 Voxels

Because the image is discrete, it is also necessary to specify by how much the elements of I_{ijk} are separated in physical space. Voxels describe the spatial distribution of the elements of I_{ijk} [50]. All the voxels in a single digital image are identical in spatial extent and have dimensions (v_x, v_y, v_z) where v_x , for example, describes the distance separating neighbouring elements along the x -axis.

The discrete nature of I_{ijk} can often be the most limiting aspect of the data and contributes towards the ability to adequately resolve features within the object alongside other limitations such as the optics or the kind of signal used in the acquisition facility. If the problem of interest is multi-scale in nature, then it is necessary to acquire images with a variety of voxel sizes so that the length scales of interest are adequately sampled.

It is desirable to have a situation where the voxel dimensions are equal to allow for equal sampling in all three spatial dimensions.

3.2.2 Bit depth

Values within a digital image are stored on a computer and must, therefore, be assigned a certain number of bits which ultimately limits the range of values the elements in an image can have [53]. The number of bits assigned to an element is called the image's bit depth. Bit depth impacts the resolution of the contrast in an image by discretization of the detected signal in the same sense that discretization of the space (see equation 2.2 in Chapter 2) impacts the spatial resolution of the image.

In figure 3.2, the distribution of a detected signal in the frequency domain is shown in red. The discretization of this signal is illustrated in black, where the bin width is a fixed size that is specified by the bit depth of the image. The lowest commonly used bit depth is 8 bit

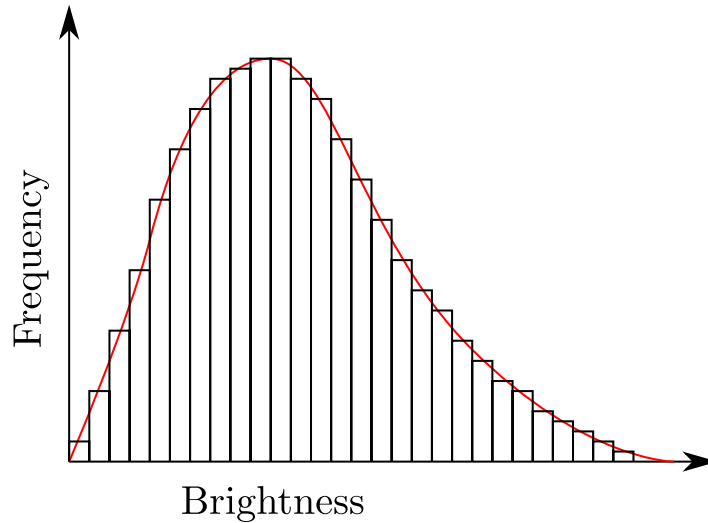


FIGURE 3.2. The discretization of detected signal as a result of bit depth.

which allows for $2^8 = 256$ possible values (0 to 255) to be assigned to the elements of I_{ijk} . In general, the number of values available for an n bit image is 2^n so that the bin width, w , is related to the bit depth by the following:

$$w = \frac{1}{2^n} \quad (3.2)$$

illustrating that the resolution in contrast increases exponentially with bit depth. However, a linear increase in disk space usage is also evident with increasing bit depth. For these reasons, it is preferable to work in the lowest bit depth necessary to visualize or segment (see section 3.6) the regions of interest within the image, thus optimizing storage of the image itself.

It is noted that binary images (i.e. 1 bit images) are also commonly produced. Binary images have elements of the image that are either ‘active’ (1) or ‘idle’ (0), which generally corresponds to regions inside and outside a particular phase of interest.

3.3 Tomographic Reconstruction

Tomographic reconstruction refers to the formation of a 3D image from a series of projections acquired in tomography facilities.

As explained in chapter 2, tomography utilises the acquisition of projections, as shown in the left image of figure 3.3, whilst rotating the sample. The image also shows the signal generated from the object at different angles. These signals describe a reduction in signal intensity due to the attenuation of the sample. In reality, hundreds of projections are taken to adequately capture complex internal geometries of real samples.

There exist many different approaches to tomographic reconstruction [53–64]; the most commonly used method is known as Filtered Back Projection (FBP) [55–58, 65–67]. This is where the projections generated are inverted, filtered and then projected back (or ‘back projected’) onto a discrete 3D space as shown in the right image of figure 3.3. As shown, using only three projections, it is possible to reconstruct an image with a geometry approximately representing the original circular sample. It should be clear that increasing the number of recorded projections at smaller angular intervals will, therefore, generate an even more precise reconstructed image.

FBP is an improvement on Back Projection (BP), which does not involve the application of filtering prior to back projecting and, thus, FBP leads to more defined boundaries in the reconstructed image [56].

In order to perform the reconstruction, it is necessary to find the centre of rotation of the sample, which can be estimated from the sinograms. Sinograms are formed by stacking the projections of a tomography scan and looking at the rotated stack as shown in figure 3.4. At the bottom of figure 3.5, there is a circular stage that rotates about its centre and a sample positioned some distance away from the centre of rotation. Projections of this sample are a

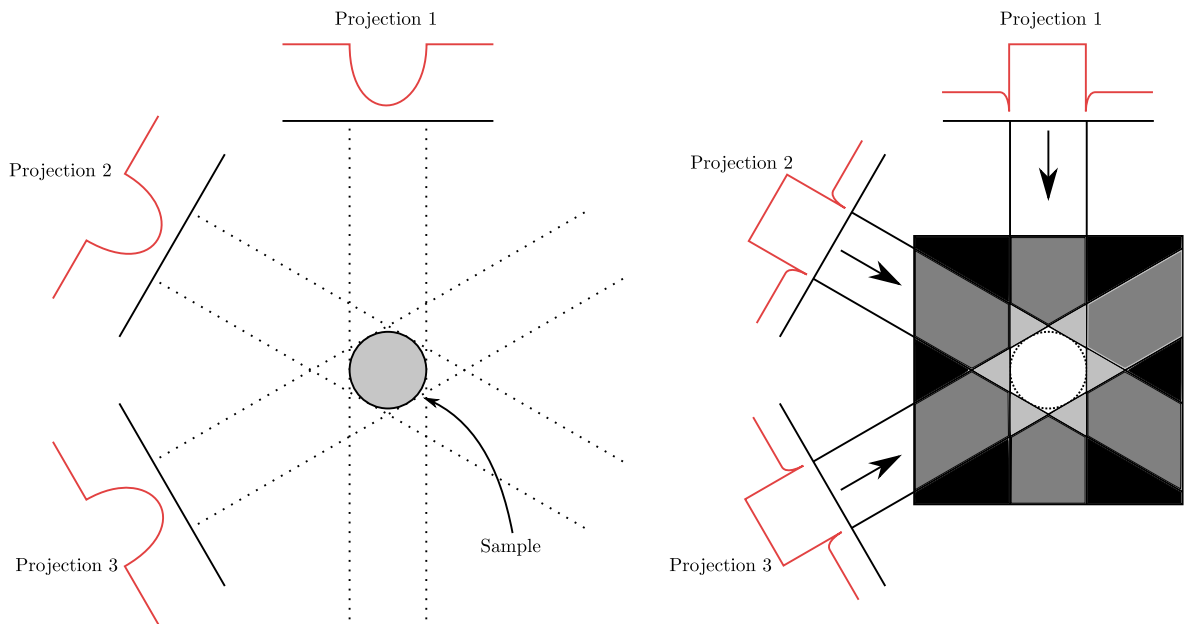


FIGURE 3.3. The acquisition of projections (left) and reconstruction by BP (right).

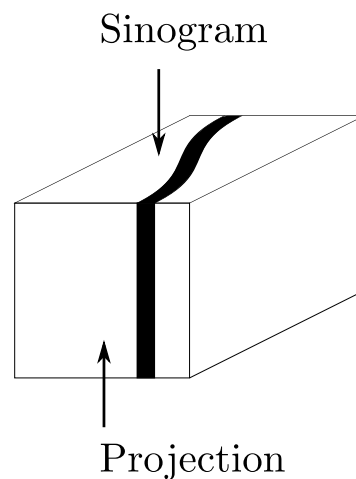


FIGURE 3.4. A series of projections and the corresponding sinograms as seen from the top of the stacked projections.

function of the angular orientation of the stage and are shown stacked at the top of the image. It is demonstrated, therefore, that a point on a rotating stage produces a sinusoidal trace in the stacked projections commonly referred to as a sinogram. In general, a sinogram can be mathematically described by the Radon transform [64, 68], which is a means of transforming a function in real space to its corresponding sinogram.

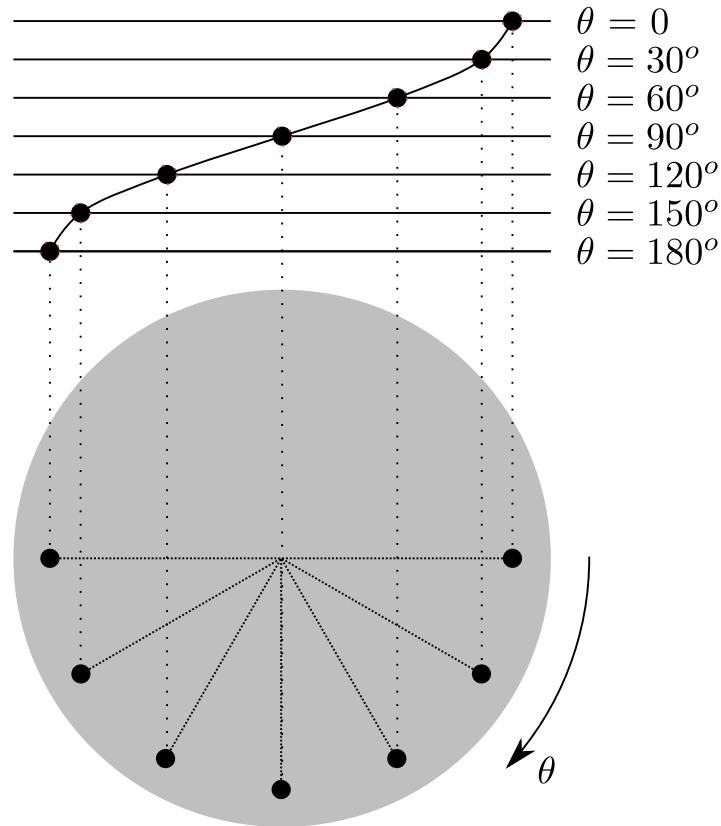


FIGURE 3.5. The formation of a sinogram of a point sample misaligned from the centre of rotation.

The initial acquisition of projections in tomography can, therefore, be thought of as performing a discrete Radon transform of the function $O(\vec{r})$. The problem of tomographic reconstruction can, thus, be thought of as transforming these projections into an image, I_{ijk} , by finding the inverse Radon transform. This is still an active area of research in the field of inverse problems in mathematics, and imaging generally, for which a number of algorithms exist. Iterative techniques such as Conjugate Gradient (CG) [54], Maximum Likelihood Expectation Maximization (MLEM) [61–63] and Maximum A Posteriori Expectation Maximization (MAPEM) [59, 60] are also commonly utilized in the place of so-called ‘analytic methods’ such as FBP [64]. The general form of iterative techniques is shown in figure 3.6.

In this figure, an initial reconstruction is performed on the projections which can then be transformed back for comparison with the original projections. Adjustments to the reconstruction can then be iteratively improved until a good agreement between the transformed

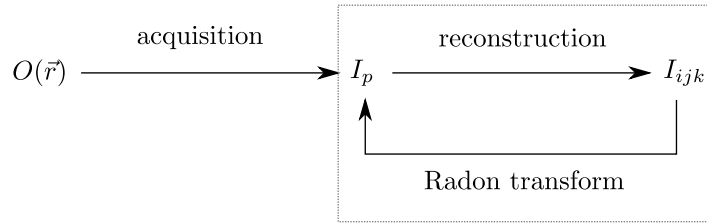


FIGURE 3.6. Showing the iterative reconstruction methodology.

reconstructed image and the original projections is found.

The particular algorithm used for synchrotron-XRT by the author has been developed by Kyrieleis and Titarenko [65–67], and utilizes the FBP technique.

3.4 Preprocessing for SBF I

Compared to tomography, the preprocessing involved in SBF I is significantly more simplified. The raw data generated are already in the form I_{ijk} , where k refers to the slice number and i & j specify the element corresponding to the pixel (i, j) on the k^{th} slice. No reconstruction step is necessary. It is, however, necessary to adequately align the image stack as misalignment due to stage movement during serial sectioning can take place.

3.4.1 Stack Alignment

Stack alignment is a process by which neighbouring slices in an image stack can be aligned to correct for sample drift in SBF I data. In some cases, it is possible to incorporate a detector to measure the sample drift, which can then be used to align the slices. In the case of SBFSEM, the drift distances are very small and difficult to measure in-situ. The method of aligning data in the post acquisition stage is the process of comparing neighbouring slices, i.e. $I(i, j, k)$ & $I(i, j, k + 1)$, and transforming them in such as way as to match similar features between slices. This procedure can be thought of as a form of 2D image registration [52] where two

similar images are aligned. This is in contrast to 2D image registration where images of the *same* ROI are aligned.

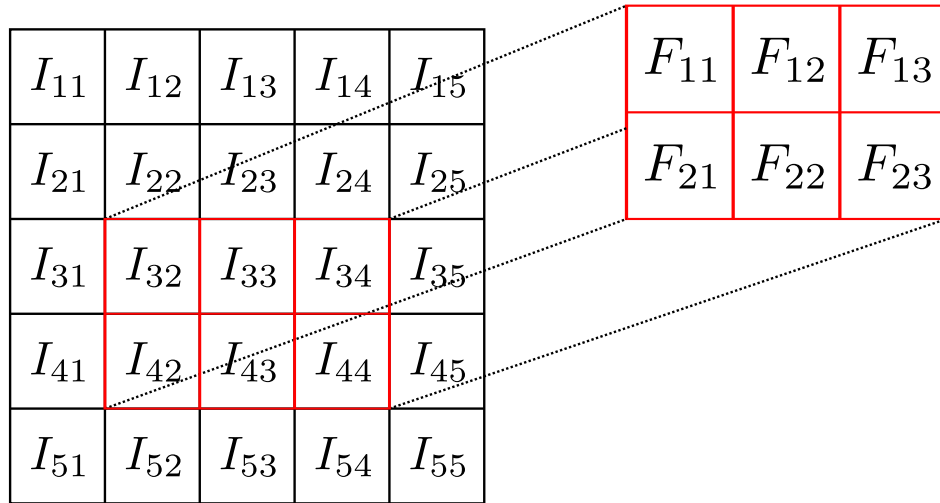
The transformation, T , can range from simple linear translations and rotations to non-linear fields that allow expansion and compression of the images. Typically, the author has utilized linear transformations to produce good stack alignment. This is motivated by the results, but also consideration of the source of misalignment. In the 3View, typically, it is observed that the misalignment is translational and in the slicing direction and, hence, simple linear translations allow for adequate realignment. In the case of FIBSEM data, rotational transformations are added as deformation of the block-face is observed during the ion beam milling.

3.5 Image Processing

Applying image filters to data is useful for a number of reasons. Primarily, filters are utilized to remove noise from an image, but can also be applied to aid later segmentation of the image. For the purpose of illustration, a brief description of how filters operate on a 2D input image, I_{ij} , follows in this section; however, all examples are applicable and extendable to 3D images, I_{ijk} .

3.5.1 Kernel Based Filtering

To understand the mechanism of most digital image filters, the concept of a kernel must be introduced. A kernel, much like a digital image, is simply an array of values with dimensions much smaller than the image it operates on. The output or filtered image, O_{ij} , is calculated by taking the convolution of the input image, I_{ij} , with the kernel, F_{kl} [69–71]. Formally, this is written as

FIGURE 3.7. The convolution of an image, I_{ij} , with the kernel, F_{kl} .

$$O = I * F \quad (3.3)$$

For a 2D digital image, the convolution is discrete [72]:

$$O(i, j) = \sum_{k=1}^m \sum_{l=1}^n I(i+k-1, j+l-1)F(k, l) \quad (3.4)$$

where m and n are the dimensions of the kernel, F_{kl} .

The application of equation 3.4 is best illustrated by an example shown in figure 3.7. Consider a 2 by 3 kernel operating on an image, I_{ij} ; the output image, O_{ij} , is computed for each element. For element O_{32} , for example, the sum of the product of the elements of I_{ij} overlapping with F_{ij} at the element (3, 2) as shown in figure 3.7 is taken:

$$O_{32} = F_{11}I_{32} + F_{12}I_{33} + F_{13}I_{34} + F_{21}I_{42} + F_{22}I_{43} + F_{23}I_{44} \quad (3.5)$$

Other elements of O_{ij} are calculated by shifting the kernel over I_{ij} to create a different set of overlapping elements.

Filters, such as the Gaussian filter, are computed in this manner. It is first necessary to compute the kernel used, which is defined by discretization of the Gaussian distribution (with $\mu = 0$) shown in equation 3.6

$$G(x, y) = \frac{1}{2\pi\sigma^2} \exp\left(-\frac{x^2 + y^2}{2\sigma^2}\right) \quad (3.6)$$

Assuming that the distribution becomes negligible beyond 3 standard deviations from the mean and using $\sigma = 1$, a 5 by 5 kernel representing the Gaussian distribution can be generated as follows [71]:

$$G_{kl} = \frac{1}{273} \begin{pmatrix} 1 & 4 & 7 & 4 & 1 \\ 4 & 16 & 26 & 16 & 4 \\ 7 & 26 & 41 & 26 & 7 \\ 4 & 16 & 26 & 16 & 4 \\ 1 & 4 & 7 & 4 & 1 \end{pmatrix} \quad (3.7)$$

In contrast to the previous general example, this kernel will position itself with its central element (G_{33}) over the element to be filtered instead of the previous example, where the first element of the kernel (F_{11}) is used.

Other very common filters used can also be non-algebraic, for example, the mean, median, minimum and maximum filters [71]. These filters look at the overlapping elements of I_{ij} with the kernel and return the mean, median, minimum or maximum value to O_{ij} . An illustration of the median filter using a 2 by 2 kernel size on an image is shown in figure 3.8.

The output image is calculated by taking the overlapping values on the input image with the kernel and then taking the median of these. For example, O_{11} is the median of the overlapping values I_{11} , I_{12} , I_{21} and I_{22} , therefore, $O_{11} = 1$. Due to the finite size of the kernel, some

0	1	2	6	6	6	1	2	5	7	7	7
1	2	3	7	7	7	2	3	8	8	8	8
2	3	8	8	8	8	3	8	9	9	9	9
3	7	9	9	9	9	5	9	9	10	10	10
3	8	9	10	10	10	8	9	10	10	10	10
7	8	9	10	10	10	8	9	10	10	10	10

FIGURE 3.8. The input (left) and output (right) image after application of a 2 by 2 median filter.

ambiguity arises on how to calculate the edges of the output image. In order to preserve the size of the image, it may be necessary to pad the input image with values that are used purely in the filtering and then discarded once the output has been calculated. In the illustrated example, the input image has been padded with the values found along the right and bottom edge of the image, i.e. the very last row or column of the image is duplicated for the purpose of performing the filtering.

Of particular importance, as illustrated in this example is the impact of such filters on edges [70]. On the left image of figure 3.8, an edge is highlighted in red, where the neighbouring pixel differential is ≥ 2 . Using the same definition of the edge on the output image, it is found that the boundary has shifted towards the lower values in the image. Highlighted in red on the right image of figure 3.8 are pixels, which were previously on the other side of the boundary. This demonstrates that the median filter is not edge-preserving as is the case for most commonly used filters, including all those described in this section so far. Preserving edges when it comes to looking at small dispersed phases* in tomographic data-sets is critical for achieving optimum volume fraction estimations as explained in section 3.8.1.

*That is to say when the size distribution is of the same order as the voxel dimensions.

3.5.2 Advanced Filters

3.5.2.1 Anisotropic Diffusion

An example of an advanced filter used by the author that preserves edges is commonly referred to as the anisotropic diffusion filter [73]. This filter operates by treating the array of greyscale values as a concentration field, $\rho(\vec{r}, t)$, that obeys Fick's law [74], which states that the flux field, $\vec{\phi}(\vec{r}, t)$, describing the 'transport' of the concentration is as follows:

$$\vec{\phi} = -D \cdot \vec{\nabla} \rho \quad (3.8)$$

where D is the diffusivity which, in general, is a tensor. Combined with the continuity equation

$$\frac{\partial \rho}{\partial t} = -\vec{\nabla} \cdot \vec{\phi} \quad (3.9)$$

an equation eliminating the flux and describing the evolution of the concentration can be found:

$$\frac{\partial \rho}{\partial t} = \vec{\nabla} \cdot (D \cdot \vec{\nabla} \rho) \quad (3.10)$$

The anisotropic diffusion filter operates by coupling the gradient ($\vec{\nabla} \rho$) of the image with the diffusivity (i.e. $D = D(\vec{\nabla} \rho)$) tensor to ensure that transport across strong boundaries (i.e. regions of high gradient) is minimized, thus preserving edges. Edge preserving filters are useful in solving some of the problems arising at the quantification stage, as previously mentioned whilst simultaneously removing noise by smoothing.

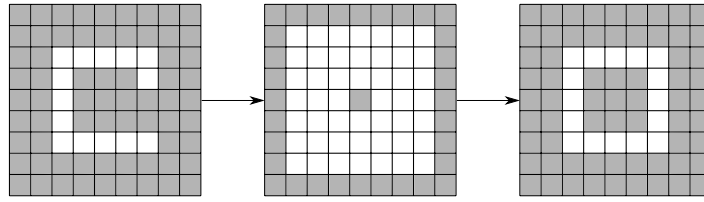


FIGURE 3.9. A binary image undergoing closing. Active pixels are shown in white.

3.5.2.2 Morphological filtering

The fundamental morphological operations that can be performed on an image are called ‘erosion’ and ‘dilation’ [75], which can act on both greyscale and binary images.

Erosion of an image, I , by kernel, K , is written as:

$$I \ominus K \quad (3.11)$$

and dilation of an image with the same element is written as:

$$I \oplus K \quad (3.12)$$

In digital imaging, these operations are identical to minimum and maximum filters, as described in section 3.5.1, respectively. The most intuitive application with binary images will demonstrate that these operations remove or add active voxels around interfaces in the binary image. Combinations of erosion and dilation operations can produce more complex operations such as ‘opening’ and ‘closing’, which can be used in image transformations such as the top-hat transform.

Figure 3.9 illustrates the process of first dilation of a simple binary image where the active pixels are expanded in all directions normal to a boundary. The second step in figure 3.9 is the erosion of the dilated image, which restores the extent of the original binary image but

has left the void filled. This overall process, i.e. dilation followed by erosion, is known as closing and is defined as:

$$I \bullet K = (I \oplus K) \ominus K \quad (3.13)$$

Conversely, erosion followed by dilation is known as opening, which is defined as:

$$I \circ K = (I \ominus K) \oplus K \quad (3.14)$$

Erosion and dilation can also be applied to greyscale images. Erosion of a greyscale image will darken the image, whilst dilation will brighten the image in the manner expected by applying their equivalent minimum and maximum filters respectively.

The top-hat transform, which is often used to detect local minima or maxima, in an image can be defined. The white top-hat transform, T_W , is defined as:

$$T_W(I) = I - I \circ K \quad (3.15)$$

The dark top-hat transform, T_D , is defined as:

$$T_D(I) = I \bullet K - I \quad (3.16)$$

These transformations can be very useful in quickly segmenting and quantifying barycentres (see 3.8.2) of large numbers of particles dispersed in a matrix provided there is adequate contrast between the matrix and the particles.

3.5.3 Image Registration

Digital image registration can be used to align different image data-sets of the same object or ROI by iteratively mapping the transformation of one image onto another and evaluating the quality of the alignment [52]. In the same manner that stack alignment is achieved, the general form of the optimization procedure is preserved here, but the transformations are afforded an additional degree of freedom owing to the alignment of two 3D images instead of two 2D slices.

An additional optimizing step can be implemented to allow for fewer applied transformations and consequential assessments of alignment quality by performing an initial downsampling of the data-sets before alignment. Once adequate alignment of the downsampled images is achieved, a higher sampled set of images can be used until the original dimensions of the images are restored to allow for fine adjustments in the transformations to be iterated.

Image registration is particularly useful for time-series data-sets as well as for correlative imaging.

3.6 Segmentation

Segmentation is the process by which one transforms a greyscale image, I , to a ‘label image’, L , whose pixel/voxel values correspond to the phase or material type:

$$I \xrightarrow{\text{segmentation}} L \quad (3.17)$$

For example, consider an n -bit 3D greyscale image of a system containing two phases. Our greyscale image will have voxels valued from 0 to $(2^n - 1)$ and, provided an adequate image acquisition technique has been employed, these values should provide a means of identifying

the two phases in the system. Segmentation will transform the greyscale image to a label image, where the voxels are either equal to 0 to indicate the presence of one phase or 1 to indicate the presence of the other phase. In this case, the label image is simply a binary image. By extension, a higher bit depth is required for label images of systems with more than two phases. Alternatively, a number of binary images can be produced for each identifiable phase in the greyscale image.

The kind of segmentation used depends on the acquisition technique, resolution and image quality. Presented in this section are two commonly used segmentation methodologies, which are ‘automatic’ in the sense that they do not rely much on the user to achieve good results provided the image quality is sufficient. In the case where images are not optimal, it is still possible to segment using semi-automatic or manual methods which rely heavily on the user. This can often be a tedious, but effective method owing to the superior pattern recognition capabilities of humans.

3.6.1 Thresholding

The simplest method for selecting voxels in a greyscale image is based purely on the greyscale value or a range of greyscale values by a process known as thresholding. In standard thresholding, one phase can be selected to produce a binary image, B , by specifying a range of greyscale values, T_{min} & T_{max} , on the image histogram as shown in figure 3.10.

This process will convert all voxels falling within this specified range to 1 and the remaining voxels become 0 as follows:

$$B = \begin{cases} 1; & \text{for } T_{min} \leq I \leq T_{max} \\ 0; & \text{otherwise.} \end{cases} \quad (3.18)$$

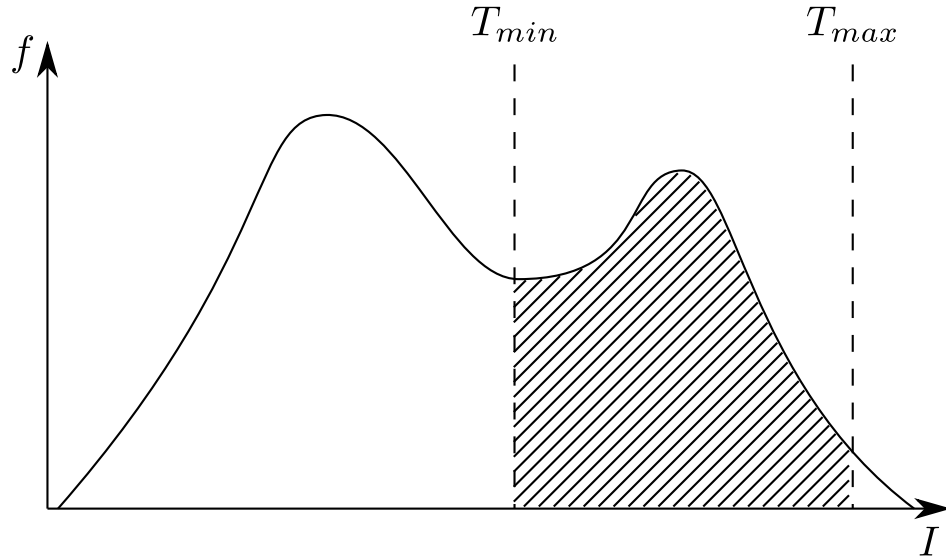


FIGURE 3.10. The segmentation of a phase by histogram based thresholding.

The values T_{min} & T_{max} can, of course, be manually adjusted by the user and it is common for software to display the selected regions using an overlay on the greyscale image. Manually adjusting the thresholding can allow the user to visually inspect the adequacy of the selection, but it is often not a recommended approach for comparative analysis because there will be natural variation in the judgment of the user leading to a reproducibility problem. Several automatic methods that compute the optimum T_{min} & T_{max} values exist [76–79], and a summary of these methods is detailed by Sezgin & Sankur [80].

Thresholding can be performed with multiple limits to define more than one phase in a label image, L . For example, if there are 3 well-defined phases that can be distinguished based on greyscale value alone then we can define two ranges T_{1min} & T_{1max} and T_{2min} & T_{2max} with the third phase being the remaining voxels or the ‘background’:

$$L = \begin{cases} 2; & \text{for } T_{2min} \leq I \leq T_{2max} \\ 1; & \text{for } T_{1min} \leq I \leq T_{1max} \\ 0; & \text{otherwise.} \end{cases} \quad (3.19)$$

It is also possible to generate masks to exclude certain voxels completely from a threshold. This can be useful if the mask covers a region that has greyscale values that fall within the threshold range, but are not part of the phase to be segmented.

Typically, thresholding can be very effective on greyscale images that have undergone some pre-processing such as the application of filters to smooth noise in the image. However, sometimes individual voxels can be selected after thresholding due to a noisy image despite filtering beforehand. It is possible to perform a series of erosions until these voxels have vanished and then follow with the same number of dilations. This will only work when the pixels to be removed are smaller than the smallest region that has been adequately segmented. This series of erosions and dilations also has the effect of smoothing edges in larger selected regions, which can impact quantification of surfaces, e.g. surface area.

3.6.2 Watershed

Watershed segmentation [81–83] is a useful algorithm for segmenting greyscale images when thresholding does not adequately find the boundaries between phases. It is most easily imagined using a 1D image as shown in figure 3.11, where a profile of greyscale values as a function of distance is shown. The greyscale values can be imagined to correspond to peaks and valleys like a landscape. The user specifies ‘seed points’ for each phase, which can be imagined to be some source of water that ‘flood’ the landscape. When water from two sources meets, a boundary is formed in the newly created label image.

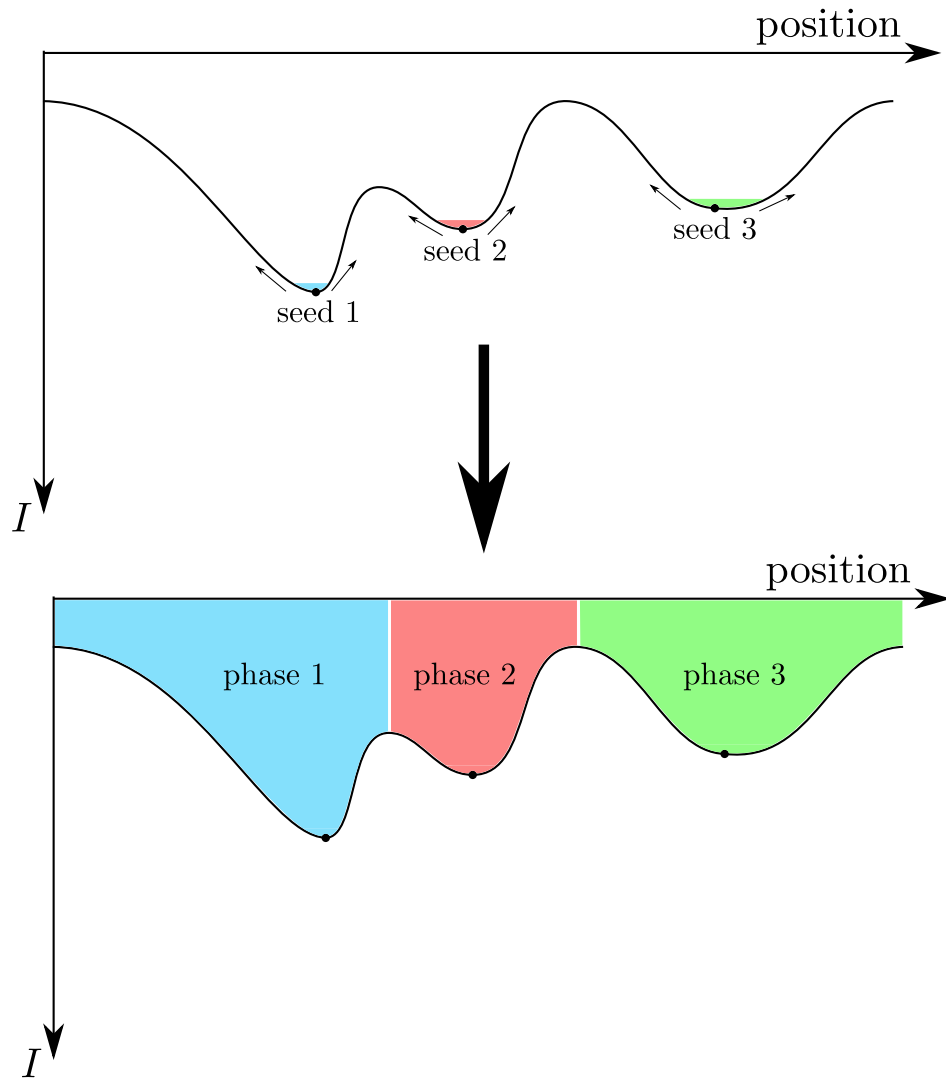


FIGURE 3.11. Watershed segmentation by the flooding from selected seeds.

3.6.3 Other tools and semi-automatic methods

Automatic segmentation methods can work very well if the image produced is of good quality. There are, however, situations where the image quality is sufficient for a user to distinguish regions within the image and to select them using semi-automatic or manual methods. There are a number of other tools available to allow a more representative segmentation to be achieved in this way.

Manual selection of individual regions can be made through specifying a range of greyscale values (absolute) or a range relative to the current voxel (relative) and manually selecting a seed point to perform a region growing algorithm [84]. This is a voxel based method that

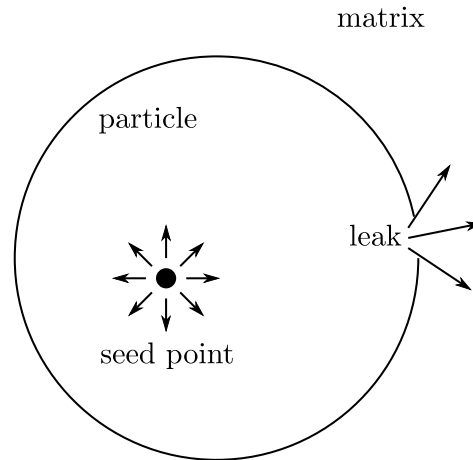


FIGURE 3.12. A particle with a weak boundary that allows leaks into the matrix by a region growing algorithm.

involves selecting a seed point, which is grown in all directions. Neighbouring voxels are added to the region based on their greyscale values. If the neighbouring voxel falls within the specified range, it is added to the region. This process is iteratively performed until any voxels neighbouring the region fall outside the specified range. Region growing can be done in 2D on a selected plane of interest or in 3D. Additional morphological operations can be performed on the selection to smooth the boundary, remove islands or other sources of noise that are picked up erroneously by the region growing.

Region growing in 3D can often lead to 'leaks' (see figure 3.12), where the region is grown far beyond what is intended by the user. These can be caused by weak boundaries surrounding the intended region. Even one voxel separating the phase from the matrix can allow leaks and there is often a trade-off between specifying the correct greyscale range and preventing leaks. One solution is to reduce the greyscale range to partially select the particle and then dilate the selection. Another can apply 2D region growing along planes that do not contain leaks and then interpolating between them as shown in figure 3.13. In this figure, a series of planes is shown in profile; three selections are made using 2D region growing as shown in black and an interpolation of these selections is shown in yellow. If a leaky boundary is present on the third plane, for example, this method can circumvent excessive region growing

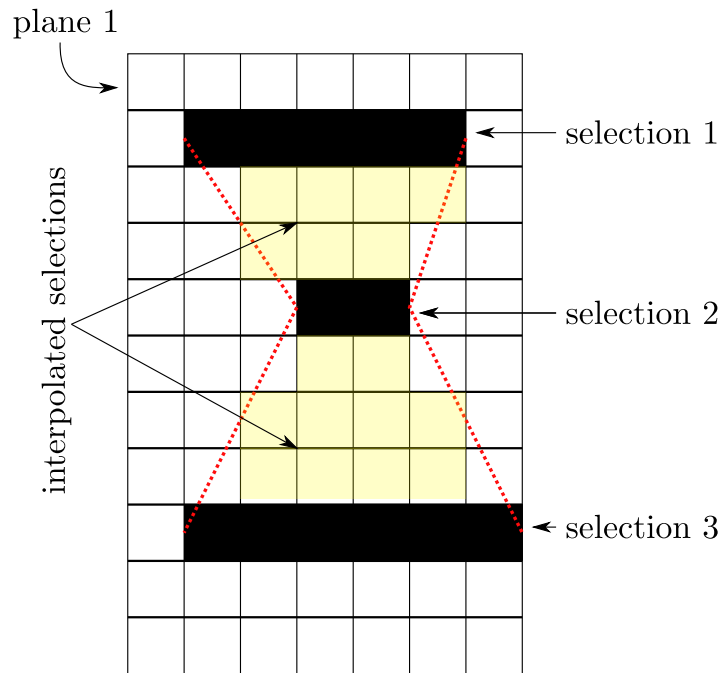


FIGURE 3.13. The interpolation between 3 selections made using a 2D region growing algorithm.

by not applying it on this plane.

3.7 Connected Component Labelling

This section will describe the meaning of connectivity in the context of labelling connected regions in a segmented image.

Once an image has been segmented, it is possible to identify, by means of a ‘connected component labelling’ (CCL) algorithm [85–88], which voxels belong to a single connected group of voxels known as a ‘connected region’. Once a binary image has undergone CCL, it becomes a labelled image where the voxel values correspond to the connected region.

CCL is especially important for images that contain dispersed particles since getting the labelling correct will be the difference between a collection of particles or a single cluster of connected particles. A combination of resolution, image dimensions, voxel size and correct segmentation all impact heavily on the connectivity of segmented regions.

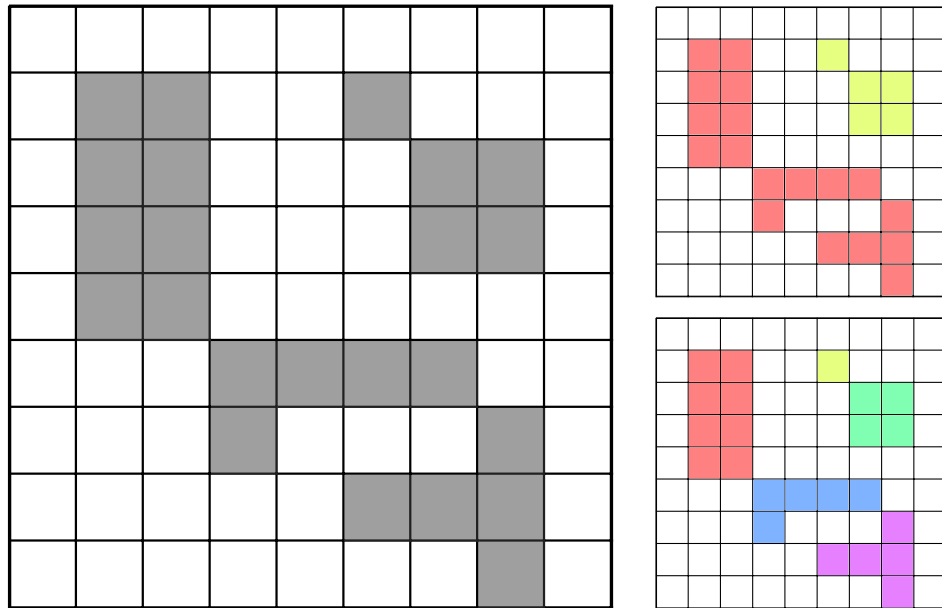


FIGURE 3.14. A 2D binary image undergoing CCL. The top right labelled image shows 2 separate connected regions whereas the bottom left shows 5 separate connected regions.

A simple 2D example of how CCL works is illustrated in figure 3.14, which shows two ways of determining connected regions. In figure 3.14, whether there are 2 or 5 connected regions in the binary image is purely down to whether pixels that share a vertex are said to be part of the same connected region or not.[†]

In the illustrated example, whether 2 or 5 connected regions are computed is determined by the ‘neighbourhood’ used in the CCL [51, 70]. The neighbourhood is defined as the number of pixels for which a central pixel is said to be connected. In 2D, it is possible to have 4-connected and 8-connected neighbourhoods, as shown in figure 3.15, which shows the 4-connected neighbourhood in blue. The 8-connected neighbourhood is a combination of both blue and red.

In 3D, there are three ways of determining the connectivity due to the extra degree of freedom associated with arrays of voxels instead of pixels.

[†]Clearly, sharing an edge would imply a connected region as, otherwise, all pixels would be considered separate connected regions.

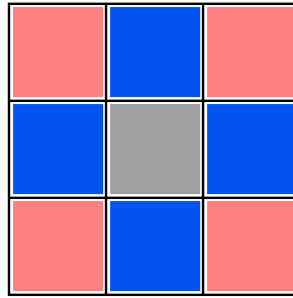


FIGURE 3.15. A central pixel with a 4-connected neighbourhood (blue) and an 8-connected neighbourhood (blue+red).

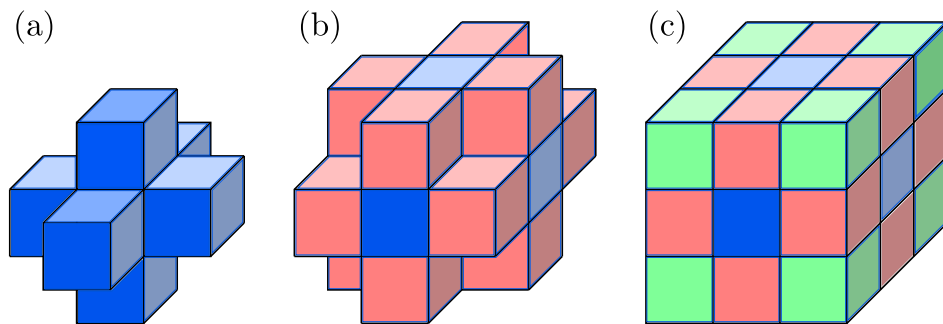


FIGURE 3.16. Three kinds of neighbourhood for a 3D image: (a) 6-connected; (b) 18-connected; and (c) 26-connected.

Figure 3.16 demonstrates the neighbourhoods used for determining connectivity in a CCL on a 3D image. In (a), the neighbourhood is defined by the number of voxels sharing a single face of the central voxel for which there are 6 as coloured in blue. In (b), we have 12 additional voxels as defined by the number of voxels sharing a single edge with the central voxel; these are coloured in red which combine with the 6-connected neighbourhood to form the 18-connected neighbourhood. Finally, voxels sharing a single vertex with the central voxel provide 4 additional voxels (coloured in green) which, combined with the previous two neighbourhoods, produce the 26-connected neighbourhood as shown in (c). These neighbourhoods can be considered to function very similarly to kernels used in image filtering in that the central pixel voxel's connectivity is assessed by the pixels within that kernel.

CCL works, therefore, by assessing whether a connected pixel falls within the neighbourhood defined by the user and producing a labelled image appropriately. It is possible to alter dramatically the number of connected regions in a labelled image by adjusting the neighbourhood

in the CCL. The neighbourhood to be applied for a particular image is not rigorously defined, but is an important aspect of the quantification methodology and should be noted for the sake of reproducibility of results. There are, however, general rules of thumb which depend on the further application of the labelled image.

If, for example, the spatial distribution of a collection of particles is to be quantified, a smaller neighbourhood would be preferable to ensure that adequate separation of particles is achieved in the labelled image. Conversely, if a morphological skeleton of a network is to be generated, a larger neighbourhood could be used to ensure that the full connectivity is captured. Ideally, as neighbourhood is ultimately an experimental variable, all neighbourhoods should be used and impacts on the continued analysis compared. However, a qualitative understanding of CCL as outlined above is usually sufficient to understand how altering the neighbourhood would impact on the results.

3.8 Quantification I

Once an image has been segmented and connected regions computed, it can then be quantified. That is to say, various characteristics of the segmented image can be assigned values which correspond to the image's geometry. Three main fundamental quantities and their calculation are presented in this section. The following section (3.9) is concerned with how to use these quantities to generate more meaningful data that can be used to interpret and compare multiple data-sets.

3.8.1 Volume

A connected region may be assigned a volume by simply counting the number of connected voxels and multiplying by the voxel volume. Formally, the i^{th} connected region has a volume,

V_i , defined by:

$$V_i = n_i v \quad (3.20)$$

Each voxel in the connected region will have a single constant value, v , for the volume and each connected region will have a varying number of voxels, n_i , associated with it as determined by the segmentation and the CCL used.

For example, if the voxel size is 50 nm by 50 nm by 50 nm and the count is 100 connected voxels, then this particle's volume is $V = 100 \times 50^3 \text{ nm}^3 = 1.25 \times 10^7 \text{ nm}^3$. Using this example to illustrate the importance and subjective nature of image segmentation, it is clear that particle volumes are sensitive to changes in their boundaries. Taking the above example for the particle volume, if the segmentation was performed slightly differently, such that only one-half of the voxels on the surface were to be included in the phase, it is expected to reduce the quantified volume by about 43% as demonstrated in the example below.

Consider a particle of volume, $V_p = 1.25 \times 10^7 \text{ nm}^3$, the effective diameter is $d_p = \sqrt[3]{6V/\pi} = 288 \text{ nm}$. If the segmentation was such that the effective diameter is reduced by the size of a single voxel length ($d_e \stackrel{!}{=} 238 \text{ nm}$), this yields a volume of $V_e = (\pi/6)d_e^3 = 0.71 \times 10^7 \text{ nm}^3$, which is approximately 43% less than the original volume!

More generally, if we consider a sphere of diameter, d , and volume, V , we find the absolute error of V by differentiating (propagation of errors):

$$V = \frac{\pi}{6}d^3$$

$$\Delta V = \frac{\pi}{2}d^2\Delta d$$

$$\frac{\Delta V}{V} = \frac{3\Delta d}{d}$$

It is, therefore, demonstrated that for the same absolute error in diameter (for example, the error introduced as a result of applying an edge altering smoothing filter or a slightly incorrect threshold) will substantially increase the relative error of the volume measurement for a ‘small’ connected region. ‘Small’ in this context is where the voxel length is of a similar order to the connected region’s effective diameter, i.e. $\Delta d \sim d$. Using edge preserving filters for materials containing a dispersed or particulate phase that is nearing the resolution limit of the detector is, therefore, preferable so that error in the volume fraction can be reduced.

3.8.2 Barycentre

The ‘barycentre’ or centre of mass of connected regions may also be quantified in a manner that is analogous to calculating the barycentres of a distribution of particles each with their own centres of mass. However, instead of an array of particles it is necessary to consider an array of connected voxels that each have a centre of mass directly at their centre. The region over which this calculation is performed is determined by the image segmentation and CCL, such that any voxels falling within a connected region are included in the barycentre calculation. Each voxel has a coordinate associated with it which is at its centre and it is

also possible to weight the barycentre by that individual voxel's brightness value, which is analogous to the mass of a particle (using the aforementioned analogy).

The equation for determining the barycentre, \vec{R} , for an array of n particles is [89]:

$$\vec{R} = \frac{1}{M} \sum_{i=1}^n m_i \vec{r}_i \quad (3.21)$$

where M is the total mass of the particles, m_i is the mass of the i^{th} particle and r_i is the centre of mass of the i^{th} particle. Following this analogy, if the brightness weighted centre of mass of the segmented phase is required, the mass is simply replaced with the intensity of the i^{th} voxel, I_i , i.e. we make the substitution $m_i \rightarrow I_i$ in equation 3.21. In addition, because the barycentre for each connected region is to be computed, we should represent the connected region by the index i as well as the voxels in the i^{th} connected region by the index j so that the j^{th} voxel in the i^{th} connected region has intensity I_{ij}^{\ddagger} and position \vec{r}_{ij} . It is now possible to represent the barycentre of the i^{th} connected region as:

$$\vec{R}_i = \frac{1}{\sum_{j=1}^{n_i} I_{ij}} \sum_{j=1}^{n_i} I_{ij} \vec{r}_{ij} \quad (3.22)$$

where n_i is the total number of voxels in the i^{th} connected region.

If the phase is uniform in density, i.e. all the voxels in that phase have the same intensity, then the calculation is simply:

$$\vec{R}_i = \frac{1}{n_i} \sum_{j=1}^{n_i} \vec{r}_{ij} \quad (3.23)$$

[‡]This should not be confused with the notation for 2D digital image.

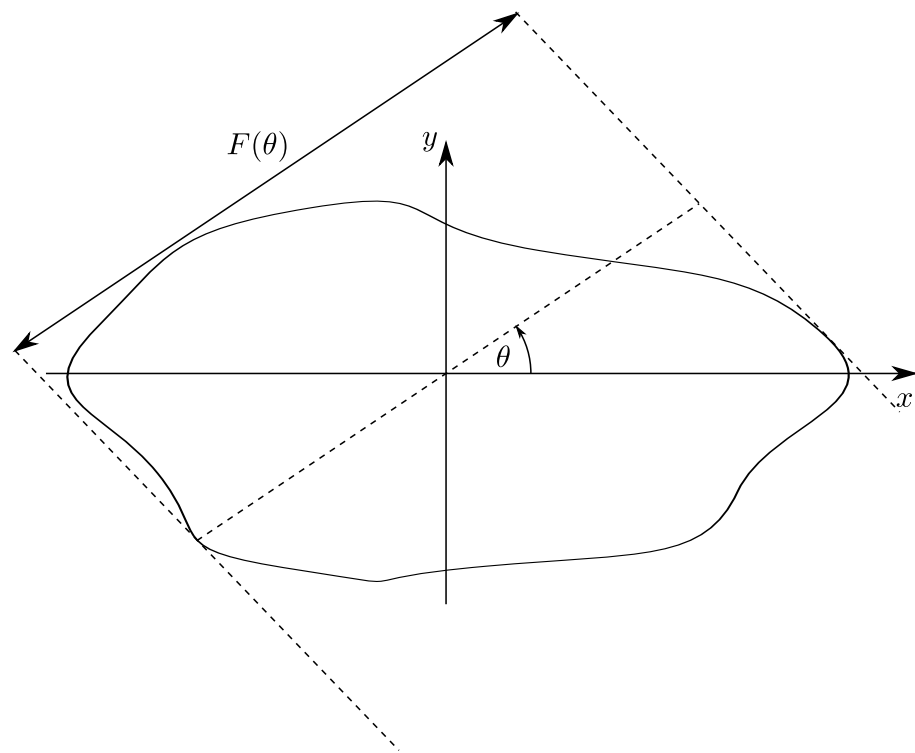


FIGURE 3.17. A particle of arbitrary shape, showing the Feret diameter $F(\theta)$.

3.8.3 Feret Diameter

The Feret diameter [90] is a distribution of distances between two parallel lines (in 2D) or planes (in 3D) as a function of the orientation (θ) of those lines or planes. Figure 3.17 illustrates a 2D example of how to measure a Feret diameter, $F(\theta)$. In 3D, the Feret diameter is both a function of the azimuthal and polar angles, $F(\theta, \phi)$, but typically interest is only placed on the minimum and maximum Feret diameters (F_{min} & F_{max} respectively). Additionally, mean Feret diameter could be used as a candidate for the effective diameter of a particle (see section 3.9.1), but the computing time required to calculate Feret diameter often exceeds alternatives used herein.

3.8.4 Surface Area

If the surface of a 3D object is defined by a set of parametric equations, $x(t)$, $y(t)$ & $z(t)$, it is possible to find the surface area of the object as follows [91]:

$$P = \int \sqrt{x'^2 + y'^2 + z'^2} dt \quad (3.24)$$

However, when dealing with digitized objects, the discrete faces which comprise the surface of a 3D object render the above equation redundant. There are a number of methods for arriving at the best estimate for surface area of a digital 3D object. A simple method involves counting the faces of the voxels, which are positioned along the interface; this approach will typically overestimate the surface area. Another method involves connecting voxel centres to form triangular surfaces, which can then be counted. Most contemporary methods involve assigning weight factors that scale the faces according to the local geometry and intensity.

In 2D images, the situation is simplified, but provides a means of stating the problem which can then be extended to 3D cases. The perimeter is the 2D analogue of the surface area in 3D and so computing perimeter in 2D examples will be explored first. Consider a binary image with square pixels of length, l_p , and a boundary as shown in figure 3.18. The perimeter may be calculated by simply counting the edges along the interface. In this case, there are 10 edges so the perimeter using our first estimate is $P_{2D_1} = 10l_p$. Another estimate of the perimeter may be computed by connecting the centres of the interfacial pixels and counting these connecting line segments [92]. In the illustrated example, there are 10 horizontal/vertical segments of length $l_p/2$ and 4 diagonal segments of length $l_p/\sqrt{2}$. This gives the second estimate of the perimeter as $P_{2D_2} \approx 7.83l_p$, which is significantly less than P_{2D_1} .

So the first estimate, P_{2D_1} utilizes *one* kind of line segment, which is either vertical or horizontal to the coordinate system of the image and has a fixed size restrained by the size

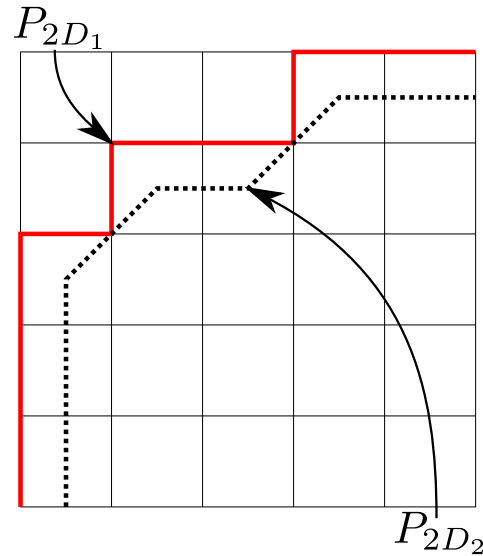


FIGURE 3.18. Two methods for calculating perimeter of a digitized 2D interface.

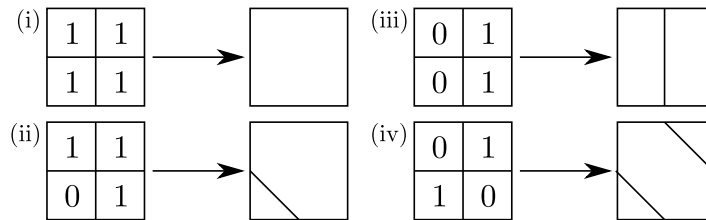


FIGURE 3.19. The 4 fundamental line segment configurations as a function of the 4-voxel neighbourhood.

of the pixels, l_p . For the second estimate, P_{2D_2} , two kinds of line segment are used that form links between pixel centres and take on lengths of either $l_p/2$ or $l_p/\sqrt{2}$. However, both these estimates do not generate optimal measurements. The best estimate for the perimeter must fall between P_{2D_1} and P_{2D_2} and this is achieved by considering the 4-pixel neighbourhood of the binary image to determine what kind of line segment should be applied and where. This method is known as the ‘Marching Squares’ algorithm [93, 94] and utilizes fifteen different line configurations. These can be simplified to four configurations that have certain transformation properties. These four configurations are shown in figure 3.19.

In case (i) in figure 3.19, the neighbourhood is homogeneous and, therefore, is not on an interface so no line segment is inserted. This configuration under inversion (i.e. $1 \rightarrow 0, 0 \rightarrow 1$) remains the same. All rotational transformations which map back onto the original grid are identical for case (i).

For case (ii), the neighbourhood shows one odd corner pixel and so the line segment is inserted diagonally across the odd pixel. Inverting this neighbourhood will not affect the inserted line segment and rotating this neighbourhood will similarly rotate the inserted line segment.

For case (iii), the neighbourhood has a vertical division of pixels and so a vertical line separating the different pixels is inserted. As with case (ii), inverting this neighbourhood will not affect the inserted line segment and rotating this neighbourhood will similarly rotate the inserted line segment.

For case (iv), the neighbourhood has a diagonal division of pixels and so two diagonal lines are inserted. Inverting the neighbourhood will rotate the inserted line segment by 90 degrees and rotating this neighbourhood will similarly rotate the inserted line segment.

To generate all 15 configurations, we take all non-identical permutations of inversions and 90 degree rotations of the 4 fundamental configurations. For case (i), there are 2 combinations by inversion. For case (ii), there are 1 inversion and 4 rotations making 8 configurations. For case (iii), there are 2 rotations or (equivalently) 1 rotation and 1 inversion making 3 configurations. For case (iv), there is 1 rotation or (equivalently) 1 inversion making 2 configurations.

Returning to the problem in figure 3.18, using the Marching Squares algorithm, the surface generated is shown in figure 3.20, which yields a perimeter of $7.54l_p$. The errors associated with using the first two estimates P_{2D_1} and P_{2D_2} are 25% and 4% respectively.

In the 3D case, it is also possible, as in the 2D case, to simply count the interfacial faces of the voxels or, indeed, to count the faces generated from connected centres of voxels. However, again, the contemporary methodology is the utilization of a ‘Marching Cubes’ algorithm [95], which looks at the 8-voxel neighbourhood to determine the inserted surface geometry. In the Marching Cubes algorithm, there are also 15 fundamental configurations which also have their own transformation rules.

When presenting results for size distributions, the effective diameter is a preferred measure instead of volume due to its linearity.

3.9.2 Shape

There are many ways to define shape; for example, the ratio between minimum and maximum Feret diameter (see 3.8.3) would provide information of the elongation of a connected region in an image. However, it is also possible to define shape as some function of perimeter and area in 2D or surface area and volume (as defined in sections 3.8.1 and 3.8.4) in 3D [96]. These functions are respectively known as circularity and sphericity, which are defined in such a way as (i) to be dimensionless; (ii) to generate a value of 1 for a circle (in 2D) or sphere (in 3D); and (iii) to generate a value of less than 1 for any other geometric shape.

These shape factors are commonly derived from considering the isoperimetric inequality [93], which states that for a closed curve of length L and enclosed area A , $4\pi A \leq L^2$ where the equality holds true only for a circular curve. Circularity is, therefore defined as $\sqrt{4\pi A}/L$, which meets all three conditions listed above. Extending the isoperimetric inequality to a higher dimension to define sphericity in 3D, one may start by making the substitution $L \rightarrow A$, which would require the numerator of circularity to be substituted for $A^{1/2} \rightarrow V^{2/3}$ to keep the dimensions consistent as per condition (i). A scaling factor of $\sqrt[3]{36\pi}/\sqrt{4\pi}$ must also be introduced to meet condition (ii) such that sphericity is defined as [71, 97]:

$$\Psi = \frac{\sqrt[3]{36\pi}V^{2/3}}{A} \quad (3.26)$$

Therefore, using the fundamental quantities of surface area and volume, as defined in the previous section, we can generate additional information about the shape of the connected region by looking at this quantity

3.9.3 Spatial Distributions

The quantification of spatial distributions of a collection of dispersed connected regions primarily utilizes the barycentres of those connected regions as discussed in section 3.8.2. A list of barycentres, does not adequately provide a clear means by which to compare different arrangements of connected regions or ensembles of particles and, therefore, further computations must be performed to meet this end. In this section, a number of quantification methodologies that elucidate spatial distribution are presented.

3.9.3.1 Number density

Number density is a very good first order approximation for gaining insight into the global distribution of the ROI. It can be used to estimate the spacing or ‘nearest neighbour distances’ (see later), which was a problem first considered over a hundred years ago to understand the spatial distribution of particles in an ideal gas [98]. The derivation has since been republished [99] and it’s applicability to 3D imaging and quantification cannot be underestimated despite its simplicity.

Assuming that the particle distribution is entirely random, it can be shown that the number density[§] has a very simple relationship to mean particle separation $\langle D_{rand} \rangle$ in n dimensional space [99].

$$\langle D_{rand} \rangle \sim \left(\frac{1}{\rho_n} \right)^{1/n} \quad (3.27)$$

It can be shown that for 2D and 3D respectively [99]:

[§] $\rho_{n_{2D}} = N/A$ for 2D and $\rho_{n_{3D}} = N/V$ for 3D

$$\langle D_{rand} \rangle = \phi_{2D} \left(\frac{A_{ROI}}{N} \right)^{1/2}; \quad \phi_{2D} = 0.5 \quad (3.28)$$

$$\langle D_{rand} \rangle = \phi_{3D} \left(\frac{V_{ROI}}{N} \right)^{1/3}; \quad \phi_{3D} = 0.55396 \quad (3.29)$$

where A_{ROI} and V_{ROI} are the area and volume of the ROI respectively and N is the number of connected regions.

In isolation, the number density is a rather simple approach to comparative quantitative analysis of segmented images but, as shown in section 3.9.3.3, it can be used to compare real measurements of particle spacings (see section 3.9.3.2) to provide a measure of global clustering.

3.9.3.2 Nearest neighbour

Calculating the nearest neighbour (NN) distances from a collection of N barycentres $\vec{R}_i = (x_i, y_i, z_i)$ can be approached in a number of ways. The author has utilized a brute force method that has been optimized by making use of MATLAB's implementation of vectorization [100, 101]. The method consists of calculating the matrix, D_{ij} , whose elements describe the distance between the i^{th} and j^{th} particle such that:

$$D_{ij} = \left| \vec{R}_i - \vec{R}_j \right| = \sqrt{(x_i - x_j)^2 + (y_i - y_j)^2 + (z_i - z_j)^2} \quad (3.30)$$

As D_{ij} is symmetric ($D_{ij} = D_{ji}$), it is possible to calculate a row or a column at a time and take the smallest non-zero (as $D_{ii} = D_{jj} = 0$) value, which will be the NN distance. The i^{th} row or (equivalently) column of D_{ij} , therefore, is calculated with the code shown in program 1 below:

```

1 % calculate number of coordinates
2 N = size(x,1);
3
4 % preallocate nearest neighbour distances
5 nn_distance = zeros(N,1);
6
7 % each loop calculates the ith element of nn_distance
8 for i=1:N
9
10         % a Nx3 matrix containing all the displacements between ...
11         % the ith particle and all other particles
12         displacement_vectors = cat(2, x(:,1)-x(i,1), x(:,2)-x(i,2), ...
13         x(:,3)-x(i,3));
14
15         % a Nx1 vector containing all the distances achieved by ...
16         % applying pythagoras to displacement_vectors
17         distances = sqrt(sum(displacement_vectors.^2,2));
18
19         % sort the distances such that sorted_distances = ...
20         % [0, NN, 2nd NN, 3rd NN, ...]
21         sorted_distances = sort(distances);
22
23         % populate the nearest neighbour distance
24         % neighbour = 1 for nearest neighbour, 2 for 2nd nearest ...
25         % neighbour etc.
26         nn_distance(i) = sorted_distances(1+neighbour);
27
28 end

```

PROGRAM 1. MATLAB code designed to calculate NN distance.

A full explanation of this code can be found in Appendix A. In summary, the code takes the barycentres, \vec{R}_i , which are transformed into a distance matrix, D_{ij} , which can be used to determine the i^{th} 's particles NN distance, D_i .

3.9.3.3 First order clustering

In section 3.9.3.1, an estimate of the mean NN distance for a collection of randomly distributed points was given $\langle D_{rand} \rangle$. How to explicitly calculate the actual NN distribution, D_i , was also demonstrated in section 3.9.3.2. It is possible, then, to determine the true mean NN distance of a collection of points:

$$\langle D_{obs} \rangle = \frac{1}{N} \sum_{i=1}^N D_i \quad (3.31)$$

Given that the only assumption made regarding the calculation of $\langle D_{rand} \rangle$ was that the distribution of points was random, taking the ratio of the estimated and observed values for mean NN distance can give insight into the randomness R_n of the distribution [102]:

$$R_n = \frac{\langle D_{obs} \rangle}{\langle D_{rand} \rangle} \quad (3.32)$$

For clarity, when the distribution is random $\langle D_{obs} \rangle = \langle D_{rand} \rangle$; when the distribution is clustered $\langle D_{obs} \rangle < \langle D_{rand} \rangle$; and when the distribution is regularly spaced, $\langle D_{obs} \rangle > \langle D_{rand} \rangle$. Therefore, we can characterize the kind of spatial distribution of the points by the ratio, R_n , as shown in table 3.1.

TABLE 3.1. Characterization of particle distribution based on R_n .

R_n	Distribution
1	Random
< 1	Clustered
> 1	Regular

3.9.3.4 Pair correlation function

The Pair Correlation Function (PCF), $g(r)$, is related to the probability of finding a point at a distance, r , from another point in a collection of points. Consider the example illustrated in figure 3.21 where, on the left, a collection of points is shown with a reference point in red at the centre. The space around the reference point is divided into concentric rings of width, Δr . In 3D the PCF is calculated by counting the number of points, n_i , within the i^{th} shell, i.e. the number of points between r_i and $r_i + \Delta r$, and using the following equation:

$$g(r) = \frac{n_i}{4\pi r_i^2 \Delta r \rho N} \quad (3.33)$$

where N is the number of particles in the volume V such that $\rho = N/V$.

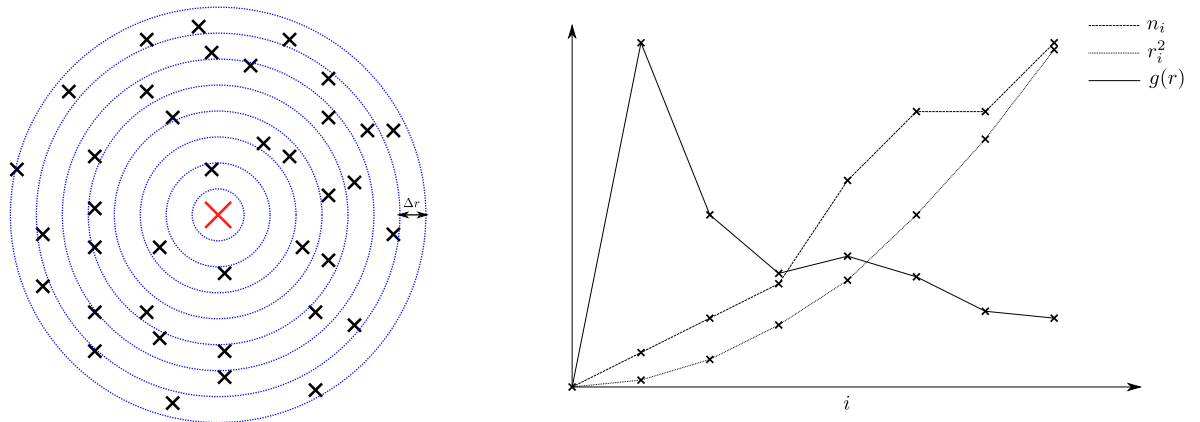


FIGURE 3.21. A distribution of points with a central reference point (left) and the corresponding plots of n_i , r_i^2 and $g(r)$.

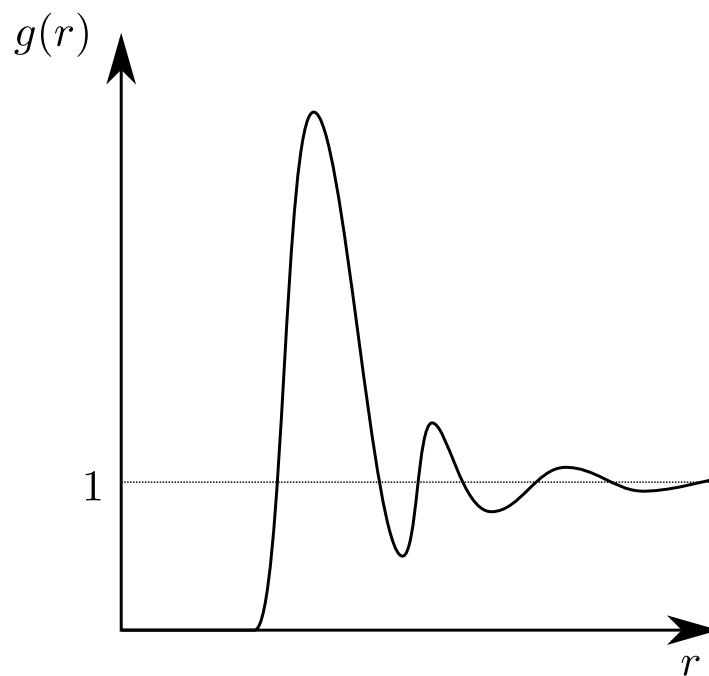


FIGURE 3.22. The typical shape of a PCF.

The right of figure 3.21 shows a scaled plot of n_i , r_i^2 and $g(r)$, which has been calculated from the illustration on the left of figure 3.21. The typical shape of the plot shows an initial maximum first peak from zero followed by a number of other peaks that oscillate around the line $g(r) = 1$, as shown in figure 3.22.

3.10 Finite Element Analysis (FEA)

FEA is a means to solve problems with complex geometries for which the governing equations are known, but the mathematical tools available are not sufficient to find an exact analytical solution. A solution, therefore, is sought by making simplifying assumptions so that an approximate solution can be found. The prevailing characteristic of the technique is to divide the geometry under investigation into smaller and more simplified parts known as Finite Elements (FE) or, simply, ‘elements’. The governing equations can then be reformulated across each element so that the problem is converted into a large series of more simple equations that can be solved by a computer. The approach is analogous to that of calculus, which involves the use of infinitesimally small elements that can be integrated or summed over to find a solution to a problem in continuous space. FEA finds approximate solutions to continuum problems by using elements that have size and extent. The global solution to the problem is then a sum of the solutions of the elements.

There are three main steps involved in FEA as indicated below:

1. Dividing the geometry up into elements (meshing).
2. Reformulation of the problem in terms of the elements.
3. Iteratively solving the reformulated problem.

3.10.1 Meshing

There are many different ways and software packages designed to produce FE meshes. A single method for producing FE meshes, as performed by the `snappyHexMesh` utility bundled with OpenFOAM [103], is described here as a method utilized by the author. This utility produces

meshes composed of hexahedra and split-hexahedra, which can then be used to find solutions for the governing equations.

Consider a binary image that forms a known boundary between some phase and the exterior. This boundary can be described by a simple stereolithography (STL) file, which is generated using a ‘generalized marching cubes algorithm’ as described in section 3.8.4 [104]. For illustration purposes, an STL surface is shown in 2D in figure 3.23 and the hexahedra are shown as squares. The meshing algorithm first generates an initial grid of the largest elements which completely surrounds the surface. This is followed by a procedure of iterative splitting of selected elements so that the geometry can be represented as accurately as possible. For each iteration of the splitting, the algorithm identifies elements that are intersected by the STL surface and splits them. Splitting produces 4 elements for every split square element and, in the 3D case, 8 elements are produced as shown in figure 3.24.

The process of splitting elements is repeated for a certain number of iterations as specified by the user. For this reason, more complicated surface geometries require a higher number of iterations to ensure the elements capture the profile adequately. In addition to this, certain elements near the surface can be skewed and deformed to better represent the boundary.

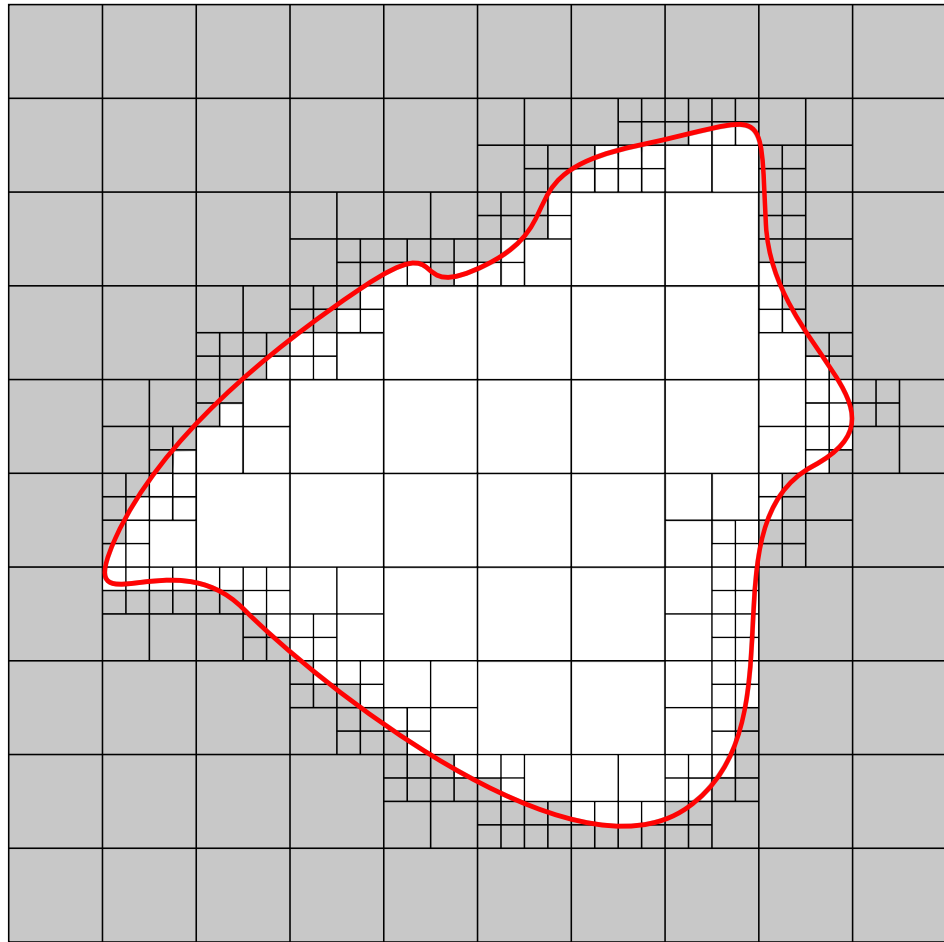


FIGURE 3.23. The meshing of an STL surface by splitting and consequential removal of hexahedra FE cells.

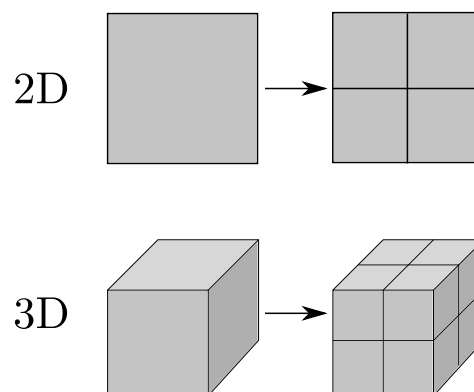


FIGURE 3.24. Splitting of square elements (2D) and hexahedra elements (3D).

3.10.2 Reformulation

Having produced a mesh, it is then necessary to reformulate the problem that is usually defined on a continuum into a discrete problem that can be iteratively solved on a computer.

Presented here is a brief description of the approach for modelling using FEs as taken from the standard introductory texts in this field [105–109]. To generate an appreciation of how this reformulation step can be performed, a simple problem of a load bearing rod is considered here. The problem itself does have an exact analytical solution owing to its simple geometry, but it can also be solved by dividing the domain into a small number of FEs.

Consider figure 3.25 where, on the left, the problem can be visualized. A tapered rod of length $3L$ and Young's modulus E has a cross sectional area of $7A_0$ at its base and A_0 at its top. The rod supports a weight of mass m and is under compression. The problem is solved analytically by calculating the field, $u(x)$, which describes the displacement of an infinitesimally thin slice at position x along the tapered rod [106]. This is done by considering the normal stress, σ , along the tapered rod:

$$\sigma = \frac{F}{A(x)} = E\epsilon = E \frac{\partial u}{\partial x} \quad (3.34)$$

In FEA, the first step is to divide the rod up into discrete elements as shown in the middle of figure 3.25. From bottom to top, these elements have cross sectional areas of $6A_0$, $4A_0$ and $2A_0$ to approximate the geometry of the original problem. This process is analogous to meshing as described in section 3.10.1. Finally, then, the problem is reduced to considering a series of rods on the right of figure 3.25 of length, L , where the assigned cross sectional areas are treated implicitly as properties of the rods. The rods are joined by nodes numbered from 1 (at $x = 0$) to 4 (at $x = 3L$).

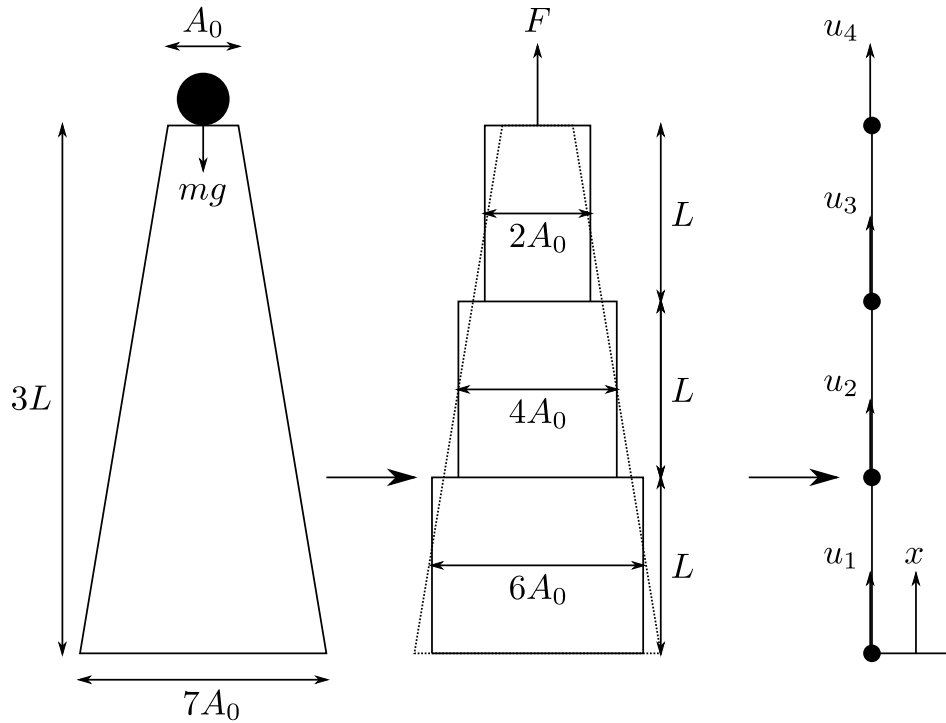


FIGURE 3.25. A tapered rod suspending a weight of mass m can be simplified by dividing the geometry into discrete elements.

The field, $u(x)$, in equation 3.34 is approximated by a discrete field, u_i , for the i^{th} node so, in general, we can write:

$$u(x) = a_{i,i}(x)u_i + a_{i,i+1}(x)u_{i+1} \quad (3.35)$$

The problem can then be written into a series of equations involving the matrix, a_{ij} , and the discrete field, u_i :

$$u(x) = a_{11}(x)u_1 + a_{12}(x)u_2; \quad 0 \leq x \leq L \quad (3.36)$$

$$u(x) = a_{22}(x)u_2 + a_{23}(x)u_3; \quad L \leq x \leq 2L \quad (3.37)$$

$$u(x) = a_{33}(x)u_3 + a_{34}(x)u_4; \quad 2L \leq x \leq 3L \quad (3.38)$$

It is then possible to calculate the shape functions, a_{ij} , which can often contain very complicated terms relating to the elements generated at the meshing stage. In this 1D example, the terms are very simple as they describe a tent function along the elements in the mesh:

$$a = \begin{pmatrix} 0 & \frac{x}{L} & 0 & 0 \\ 0 & 2 - \frac{x}{L} & \frac{x}{L} - 1 & 0 \\ 0 & 0 & 3 - \frac{x}{L} & \frac{x}{L} - 2 \end{pmatrix} \quad (3.39)$$

Typically, however, these shape functions are generated by computer packages [106, 110].

The normal stress field is also discretized and is defined between two nodes i and $i + 1$ as:

$$\sigma_{i,i+1} = \frac{F}{A_i} = E \frac{u_{i+1} - u_i}{L} \quad (3.40)$$

3.10.3 Solving

Once the problem has been reformulated, a solution can be sought by once again utilizing the underlying equation. In this case, equation 3.34 can be used as we have rearranged the problem in terms of the discrete fields, σ and $u(x)$. These quantities can be plugged back into the equation for validation of the solution [106]:

$$\sigma - Eu'(x) = R \quad (3.41)$$

where R is called the ‘residual’. In order to solve the problem, therefore, many different stress and displacement fields are trialled and an accompanying residual is calculated. The objective of the solver is to minimise the residual as this indicates how closely the discrete fields represent a solution to the problem as stated in its original form.

3.11 Resolution

In digital imaging, the term ‘resolution’ can often be ambiguous as the term is used to describe many different aspects of the limitations of certain imaging facilities. With the increasing popularity of digital imaging in the past decade, the term has become part of the common vernacular, which has led to confusion of the term. For example, resolution is now used to describe the number of pixels in a display or CCD. In addition, the physical dimensions that corresponds to the size of a pixel (i.e. the pixel size) are commonly quoted in place of the resolution of the imaging facility. Experienced practitioners also mistakenly take resolution to be the smallest object that can be seen in the facility. Provided there is sufficient contrast, it is possible to detect features much smaller than the pixel size of the facility.

From an optical perspective, resolution is the ability to distinguish between two points that are close together [111]. This limit depends on a number of factors that depend on the optics of the system as well as the signal being used. The ‘limit of resolution’, Δl_{\min} , is defined as [112, 113]

$$\Delta l_{\min} = 1.22 \frac{f\lambda}{D} \quad (3.42)$$

where f is the focal length, D is the aperture size and λ is the wavelength of the signal.

In an SEM, it is often spot size, which is determined by the optics of the overall facility, that determines the resolution. Consider figure 3.26, which shows two points in red separated by distance r . As the spot (shown in yellow) of the SEM rasters across the points, a signal is produced as shown. The SEM detector, for each location of the spot, produces a signal that is the magnitude of the convolution of the spot with the sample. In the considered case, when the spot is in its leftmost position, no part of the spot interacts with the points and

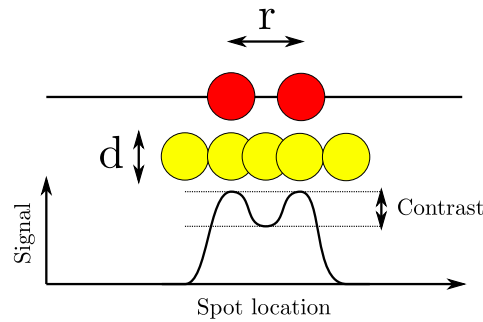


FIGURE 3.26. A schematic demonstrating the convolution of two points (shown in red) separated by a distance r with the SEM incident beam (shown in yellow) of spot size d .

the signal is at its minimum. In the second position from the left, the spot fully overlaps with the leftmost point and a maximum signal is generated. As the spot continues to move right, the signal drops as the interaction between the point and the spot reduces. If the point separation is sufficiently small, the reduction will not be to a minimum as the spot begins to overlap with the second point and the signal increases once again. The difference between this upper signal and lower signal is labelled as ‘contrast’ in figure 3.26. It is clear that if the points do not produce adequate contrast from the background, then the ability to resolve them is reduced. In this example, it is shown that the two points can be resolved provided there is adequate contrast in the signal since two clear peaks which correspond to the points are shown.

In the first example, the spot size is of the same order as the point separation, i.e. $d \sim r$. Three other examples, shown in figure 3.27, demonstrate $d \ll r$, $d = r$ and $d \gg r$ respectively. By performing the same steps by convolving the spot with the features to produce the signal, it is clear that one must use a spot size smaller than the separation of the points to resolve them.

In addition to the resolution limits based on the optics of the system, it is also necessary to consider the limitations of resolution based on the discretization of the images. In reality, a pixel represents the average of the convolution of the spot with the sample over a period of time known as the dwell time [1]. This discretization of the space in the image allows the

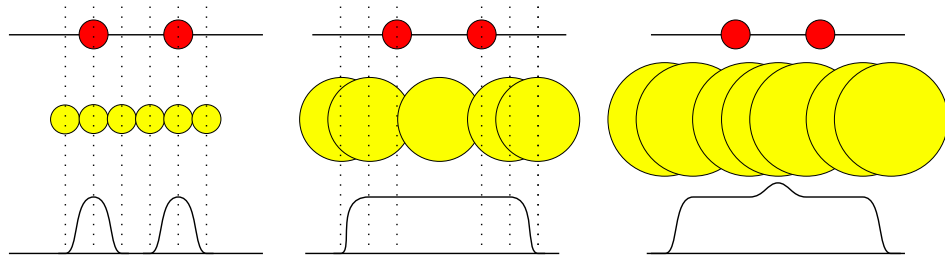


FIGURE 3.27. Illustration of the impact of spot size on the representation of two close together points.

image to be stored digitally, but also comes at the expense of potentially losing additional information due to the pixel size. Figure 3.28 shows how two points can be converted into a digital image. The important variable is the pixel size shown by the overlay of a grid relative to the separation of the two points. In the first example on the left of figure 3.28, the pixel size is sufficiently small to provide two pixel widths of separation between two connected regions in the digital image and, thus, adequate pixel dimensions have been used to allow resolution of the points. On the right of figure 3.28, the two points are converted into a single connected region with no real hope of distinguishing them in the image itself[¶]. The middle of figure 3.28 shows a situation that also produces a single connected region. This can, however, be dealt with using a separation algorithm that can produce splits through connected regions such as the one discussed here. This does, however, highlight the limiting case in terms of digital imaging as any pixel sizes greater than this situation will not be capable of resolving these two points.

In addition to the spatial discretization of the image, the signal itself is discretized as discussed in section 3.2.2. The bit depth of the image is, also, a factor when considering resolution. If, for example, a threshold is applied to an image with a low bit depth, the ability to distinguish the points from the background is more difficult. In addition, the contrast as labelled in figure 3.26 may be of the same order as a bin width, making the distinction between the two points impossible.

[¶]There may, in fact, be a means to resolve the points if there is an adequate drop in signal between the two points.

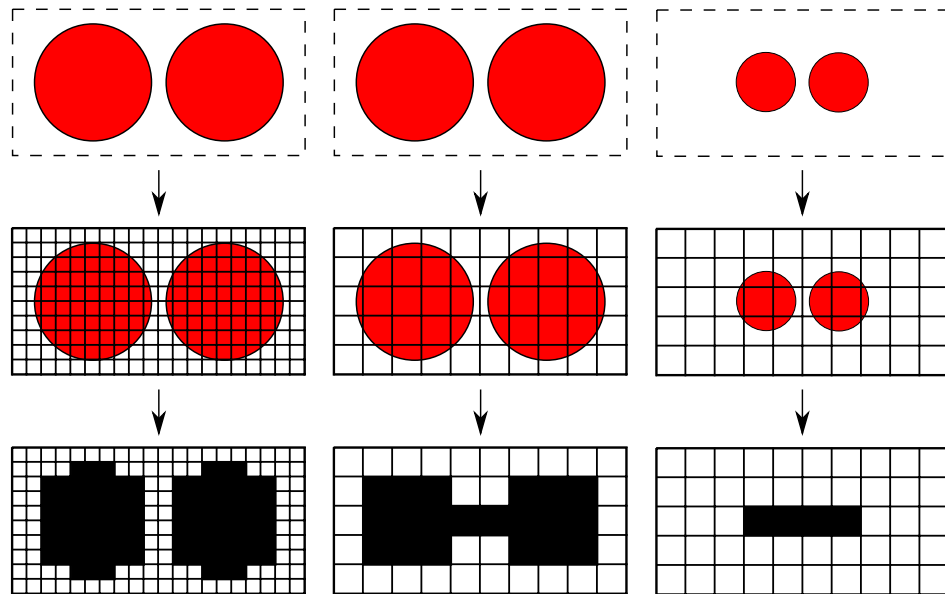


FIGURE 3.28. The discretization of two close together objects.

The optical and digital aspects of resolution considerations have been discussed. For imaging objects that are at the limit of the apparatus, these considerations should factor into the quantification. For example, in size distributions, the number of connected voxels in a region is counted. However, the potential inability to distinguish between a single connected region and a collection of close together objects lends ambiguity to the quantification. With improved resolution, the size distribution should shift to show an increase in the number of small regions alongside a decrease in the number of large regions. In addition, spatial distributions will become smaller with an ability to resolve smaller distances and, hence, NN and pair correlation functions will also be affected.

3.12 Concluding remarks

An overview of the image processing and data analysis applied has been explored in this chapter. In combination with chapter 2, this completes the discussion of the main techniques employed by the author. The description of an image as well as how an image can be formed has been provided. An explanation of the variety of operations that are typically performed

on the image such as filtering, segmentation and CCL have been elucidated. The motivations for this procedure has also been explored under the main themes of quantification and FEM. Finally, a discussion on resolution and the additional limitations placed on the ability to resolve objects is presented. This discussion contains considerations that impact resolution due to discretization of the signal by binning (see figure 3.2) as well as discretization of space by pixels (2D) and voxels (3D) (see figure 3.28).

Chapter 4

Aesthetic Properties of Protective Coatings

4.1 Introduction

Protective coatings serve a variety of functions that are both practical and aesthetic. TiO_2 is widely used as a pigment in many different kinds of coatings from domestic to high performance aerospace paints. Being an expensive material, therefore, the principle aim of this investigation is to understand how to optimize the concentration of the pigment to provide adequate opacity and spreadability by finding quantifiable trends and correlations between aspects of the microstructure and its measured opacity.

Opacity is the ability of a coating to prevent the passing of electromagnetic radiation (typically visible light). The opacity of a coating can be seen as both an aesthetic and a practical quality as it firstly prevents the protected surface from view but, either as an incidental or intentional outcome, may also protect the surface, or the coating itself, from radiation damage. In the case of TiO_2 , it is a very good blocker of ultraviolet (UV) radiation, which is known to damage polymers [114]. Principally, then, the TiO_2 preserves the integrity of the coating by preventing UV damage to the paint binder.

In this chapter, an introduction to light scattering theory is presented in the context of understanding how the internal structure of coatings relates to hiding power or ‘opacity’. SBFSEM has been utilized to investigate the structure of domestic paints containing TiO_2 particles; this also reveals the necessity for 3D imaging and quantification over traditional 2D techniques. Quantification of the spatial distribution of the paints is computed and finally compared with spreadability measurements. Spreadability is found to correlate with the NN distribution of the pigment. The 3D spatial distribution of paints on the sub-micron scale is, therefore, critical in optimizing the performance.

4.2 Review of Light Scattering

Cured paints consist primarily of two components:

1. binder and
2. pigment.

The binder is typically a polymer resin and is the principle component of any paint. It provides adhesion as well as many other mechanical properties of the film which will not be discussed beyond its necessity for serving barrier and suspension functions within paints.

The term ‘pigment’ is considered to be very broad in definition and may be further subdivided. For example, a pigment such as the one considered in this chapter is primarily added for protection associated with its hiding ability. However, as described later in chapter 5, pigments can also act as corrosion inhibitors. ‘Extenders’ are other kinds of additives that are optically inert and primarily serve to increase the volume of the paint to reduce cost and/or to alter the mechanical properties of the coating [115].

In this chapter, an investigation into a paint consisting of an epoxy-based binder, TiO_2 pigments and a variety of fillers will be conducted. TiO_2 pigments form distributions of small particles of dimensions around $0.23 \mu\text{m}$, which is the optimum size for the pigment in white paint [116]. The size and shapes of the particles are important in appreciating how they interact with the incident light, which ultimately determines the appearance and general optical behaviour of the paint [117].

Classical understanding of the behaviour of electromagnetic radiation is achieved through solving Maxwell’s equations [118], but the majority of the work in understanding how light interacts with matter has been advancing for well over a century after Maxwell first published this work. Light scattering is a term used to describe a number of optical interactions such as

reflection, refraction and diffraction [119]. The particular aspects relating to understanding the optics of pigmented materials will be briefly summarized herein by selecting work from the study of Light Scattering Theory. A review of the early work relating to the scattering of light from single particles of differing geometries will be followed by more modern approaches, which consider multiple and dependent light scattering phenomena.

4.2.1 Mie Scattering and Other Boundary Condition Methods

The most simple formulation of the problem of light scattering is one involving the scattering of planar electromagnetic waves incident on a spherical particle that was first considered by Lorenz [120], but also independently by Mie [121] and is termed Mie Scattering or the Mie Solution. Obtaining algebraic solutions for this most simple problem can require considerable work [122]. Approximations may be employed based on the relative length scales of the particle and the wavelength of the incident light to reduce the calculations, for example the Rayleigh approximation [123] valid for small particle diameters. For light scattering from pigmented materials such as paints, where the particle sizes are of similar size to the incident radiation wavelength, however, these kinds of approximations are not valid [124].

Mie Scattering set a precedent in the particular mathematical technique for approaching such problems in light scattering known as Boundary Condition Methods [119]. Asano and Yamamoto [125] achieved analytical solutions for the scattering of light from a single spheroidal particle as a function of its geometry as well as its refractive index, which extended the Mie Solution to individual particles of a more general shape and physical parameters. Understandably, this solution is considerably more laborious than the Mie Solution and only considers a single particle.

With the above two methods taken into account, it is clear that applying such techniques to large arrays of particles of arbitrary shape and size will certainly not be possible analytically.

Considering even single particles of arbitrary shape and size will require some kind of approximation or a numerical method [119] and so it will be necessary to discuss non-analytical approaches to these kinds of problems. In the knowledge that computation has advanced considerably since Jones' review on the topic of light scattering, concentration on two numerical methods for which computers can be utilized will be made herein [119].

4.2.2 Extended Boundary Condition Method (T-Matrix Method)

The first numerical method that is still used in contemporary modelling of light scattering was first formulated by Waterman [126] and was termed the Extended Boundary Condition Method (EBCM), which is nowadays referred to more generally as the T-Matrix Method (TMM). The problem is approached by imposing the boundary condition that in the region of space enclosed by the particle, the field resulting from the incident wave is cancelled by the induced surface currents of the particle. By imposing this condition, the field “in the exterior region [of the particle] can be determined from considerations in the interior”. Initially, Waterman solved this problem by considering continuous axially symmetric particles, but the TMM has been shown in a review by Mishchenko et al [127] to be applicable to arbitrarily shaped single particles as well as ‘ensembles’ of non-spherical particles. The mathematical form of the problem is as follows:

$$\begin{bmatrix} \vec{p} \\ \vec{q} \end{bmatrix} = T \begin{bmatrix} \vec{a} \\ \vec{b} \end{bmatrix}$$

where T is the ‘amplitude scattering matrix’ which transforms the incident electric field components, \vec{a} and \vec{b} , of the incoming wave to the components of the scattered electric field, \vec{p} and \vec{q} [127]. Mishchenko et al go on to demonstrate many advantages for using TMM to reduce computing time compared to other techniques. The extension of this method from

a single particle to multiple particles is made by assuming that the total scattered field is the sum of the individual scattered fields from each particle for which the T matrices are known. Bruning and Yuen [128, 129] first used this method for scattering systems of two spheres, and then “an arbitrary number of scatterers” was later computed by Peterson and Ström [130, 131].

4.2.3 Discretized integral formulation method (The Moment Method)

An alternative numerical method involves solving a number of integral equations derived from Maxwell’s equations and is termed the Moment Method [132]. Maxwell’s equations can be used to derive the Electric Field Integral Equation [133] which can then be used to generate a set of linear surface integral equations [132]. These integral equations can be solved by discretizing the space for arbitrary geometries [134, 135] in a manner very similar to the FEM [107].

4.2.4 Multiple scattering (Monte Carlo and Kubelka-Munk)

In an ensemble of scattering particles, when the separation of the particles is significantly less than the mean free path of the scattered radiation, it is necessary to consider multiple scattering models to understand how the light behaves. The above two numerical methods can be extended for multiple scattering events, but do require a great deal more mathematical rigour or some suitable assumption to allow for approximations [136–138].

Alternatively, a simpler approach that is more computationally expensive is the Monte Carlo method [139–142], where individual scattering processes are tied together successively such that individual paths through the ensemble can be computed one at a time.

A very popular methodology for modelling thin films such as paints is often employed, which makes a number of assumptions to formulate a very simple problem. The approach is referred to generally as the Many-Flux Method and leads to a calculation of the transmittance and reflectance of a medium provided it is reasonable to assume the following [143]:

- The material is "thin" such that its thickness is much smaller than its planar dimensions.
- The material is homogeneous (translational symmetry) and isotropic (rotational symmetry).
- The boundary conditions are time independent (i.e. incident radiation intensity is constant with time and the optical properties of the material are also time independent).
- The material does not emit radiation.

The Multiple-Flux Method considers a number of radiation 'channels' within the material that take on discrete directions relative to a spherical coordinate system in the material. The simplest and most well known case is that published by Kubelka and Munk [144], which considers only two channels orthogonal to a continuous material consisting of infinitely thin reflecting absorbing and transmitting layers as shown in figure 4.1. The first channel is in the direction travelling from the incident light into the material and is called the transmitted channel, and the second channel is in the direction opposite to the first. The equations are integrated along the thickness of the material such that at any stage a channel can be attenuated, reflected or transmitted through the infinitesimally thin layer, which can account for the effects due to multiple scattering within the material. The full optical behaviour of the material can then be characterized by determining the scattering and absorption coefficients derived from the above considerations. These coefficients are relatively simple to measure through illuminating the sample and measuring the transmitted and reflected intensities [145]. Due to the simplifications made with respect to the Many-Flux Method, errors are often

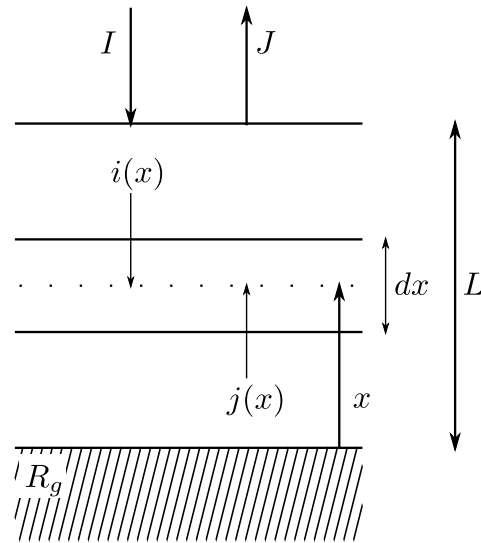


FIGURE 4.1. The mathematical considerations used in the Kubelka-Munk method where a film of thickness L atop a material of known reflectance R_g is illuminated by a source of intensity I reflects with intensity J .

introduced as a result of not considering the polarization of light [143] or the general fact that the interacting material can change the optical properties of the incident light [146]. These errors can often be overcome by simply adding more channels to account for the differences in optical properties of the radiation, therefore, making the Multiple-Flux Method ideal for modelling the optical properties of paints and other thin films.

4.3 Objectives

The cost of white paint comes predominantly from the cost of TiO_2 itself and, therefore, it is important to optimize its use [117]. It is the aim of this investigation to quantitatively characterize the paint samples to obtain relationships between the macroscopic properties such as spreadability and opacity with microscopic properties such as the distribution of the TiO_2 . Auger et al. have investigated the scattering cross sections of clusters of TiO_2 as a function of the size and shape distributions by using known scattering properties obtained from T-matrix simulations [116]. Contemporary high resolution 3D imaging can provide additional information such as the spatial distribution of TiO_2 of real paint systems, which will

be used to compare with known values for spreadability. Additionally, using these techniques, it is possible to produce FE, Image Based Models (IBMs) from the 3D data-sets that can be used to reveal the full scattering properties of the system.

4.4 Samples

Initial investigations of the spatial distribution of TiO_2 involve the use of traditional 2D electron microscopy to investigate the sub-micron structure of 3 domestic paints each containing 14% of TiO_2 (by volume). Different extenders are added to the paints as shown in table 4.1 alongside the respective values for spreadability. A reconstructed image of the organic extender used in sample 103 is shown in figure 4.2.

TABLE 4.1. Variables and their definitions used in the NN code.

Sample name	Extender	Spreadability (m^2L^{-1})
103	organic	5.50
104	inorganic (small)	6.58
105	inorganic (large)	6.94

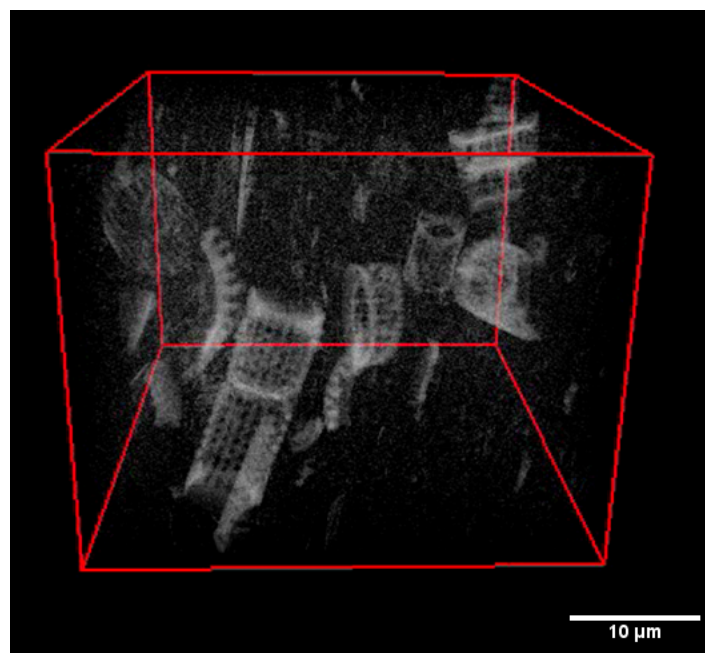


FIGURE 4.2. A volume rendering of the organic extender used in sample 103.

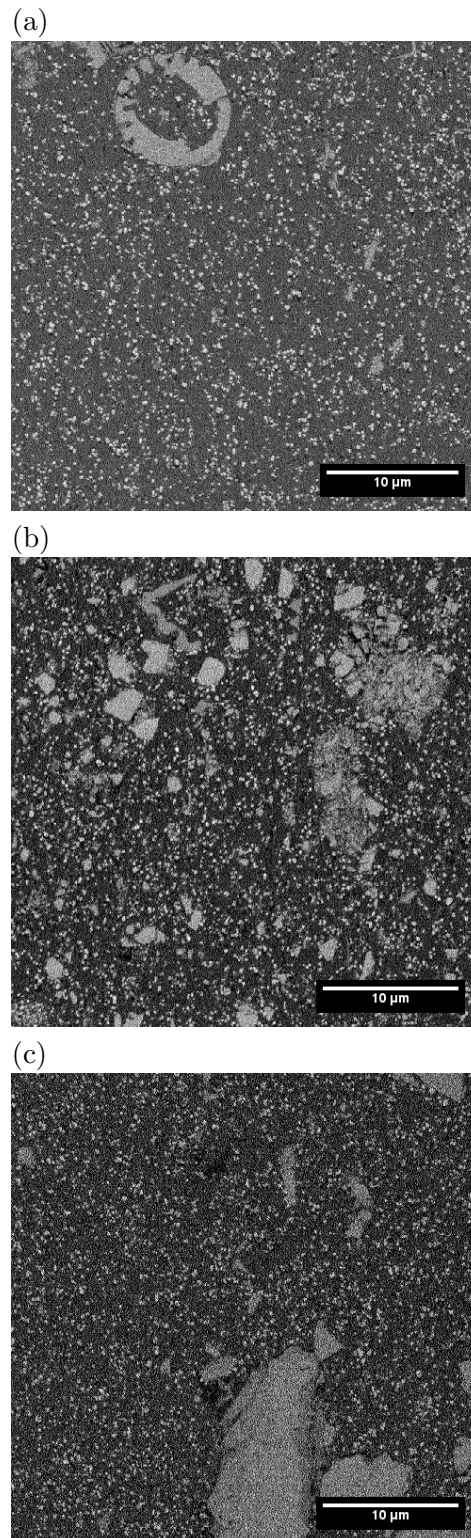


FIGURE 4.3. Scanning electron micrographs of samples 103 (a), 104 (b) and 105 (c) showing the extenders and TiO_2 particles in the epoxy binder. The scale bars are 10 μm .

Conventional 2D ESEM reveals the structure of the samples as shown in figure 4.3. As the extenders role is to increase the overall volume of the paint, they are not directly included in the analysis of the spatial distribution of light scatterers that are predominantly the TiO_2 particles. The particles themselves have also undergone TEM to observe their profiles; expected particle diameters are $\sim 10^{-1} \mu\text{m}$, which is in line with the narrow size distribution that manufacturers supply (around $0.23 \mu\text{m}$) [116].

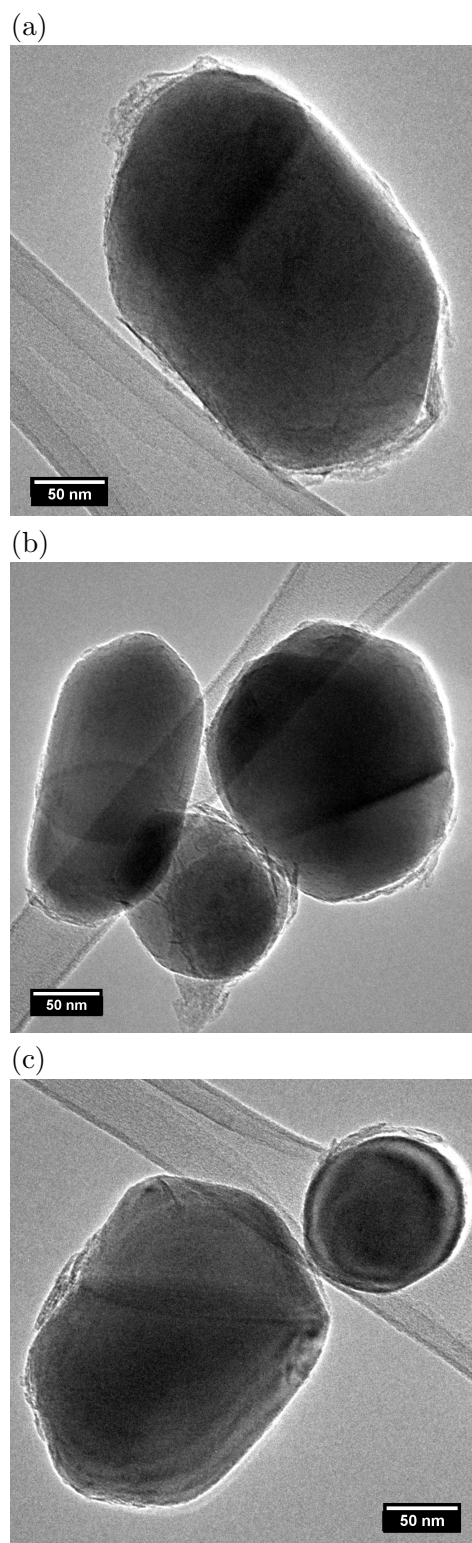


FIGURE 4.4. TEM images of the TiO_2 particles. The scale bars are 50 nm.

4.5 2D Quantification

It has been long established that quantification based on 2D data can be problematic. For example, the *estimation* of the size distribution of a system based on 2D information is possible although a number of limiting assumptions must be made that will not necessarily represent the system. In addition, the spatial distribution and shapes of objects simply cannot be adequately estimated using 2D information [147]. Initial analysis of the 2D sample images demonstrates the necessity for 3D image acquisition and quantification to obtain representative measurements. The 2D images are segmented and quantified as described in Chapter 3. A 2D version of the NN code detailed in appendix A is applied to the barycentres to provide NN distributions for the image. When compared to the 3D NN distributions, there is a significant increase in the mean and variance of the distribution. Figure 4.5 shows some typical results that have been fitted with a probability density function (PDF) in the form of a gamma distribution shown in equation 4.1.

$$f(x|a, b) = \frac{1}{b^a \Gamma(a)} x^{a-1} \exp\left(\frac{-x}{b}\right) \quad (4.1)$$

where a and b are the parametric variables that determine the shape and scale of the distribution respectively.

Due to the fact that it is possible for the NN to lie below or, indeed, above the imaged surface (see figure 4.6), it is clear that 2D techniques will not produce representative NN distances. In fact, the probability that the NN of interest happens to lie on the imaging plane for a 2D image is demonstrably low. Therefore, 2D images will never produce representative NN distributions.

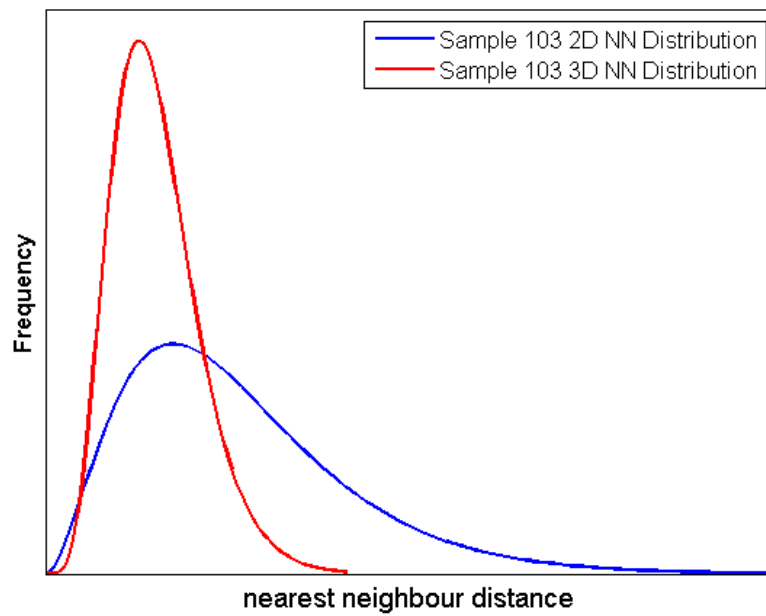


FIGURE 4.5. The fitted, normalized 2D NN distributions for a 2D image (blue) and 3D image (red).

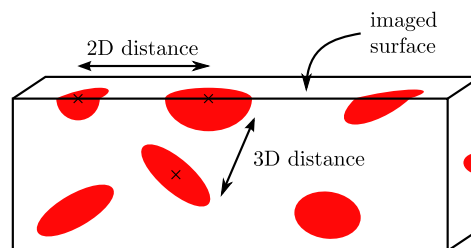


FIGURE 4.6. A schematic showing the possibility of the NN lying below the imaged 2D surface.

4.6 Methodology

Two SBFSEM techniques are employed to investigate the spatial distribution of TiO_2 particles: both 3View (see section 2.4.6.1) and FIBSEM (see section 2.4.6.2) are used. For the 3View, samples are prepared by ultramicrotomy as described in section 2.3.1 and for FIBSEM, samples are prepared as described in section 2.3.2.

In the 3View, images are acquired at 2 magnifications using a BSE detector. The low magnification images have a voxel size of $54 \text{ nm} \times 54 \text{ nm} \times 50 \text{ nm}$ and image dimensions of $744 \times 744 \times 800$. The high magnification images have a voxel size of $9.6 \text{ nm} \times 9.6 \text{ nm} \times 20 \text{ nm}$

and image dimensions of $1024 \times 1024 \times 459$. In the FIBSEM, images are acquired using a BSE detector with a voxel size of $10 \text{ nm} \times 10 \text{ nm} \times 10 \text{ nm}$ and image dimensions of $1156 \times 1086 \times 160$

Both the high magnification and FIBSEM images were acquired solely for sample 103 for the purpose of validating the results of the quantification for the spatial distribution of the particles. In addition, FIBSEM was used to quantify the pair correlation function, NN orientation, size and shape distributions which are shown to accurately represent the profiles of the TiO_2 particles.

4.7 Results & Discussion

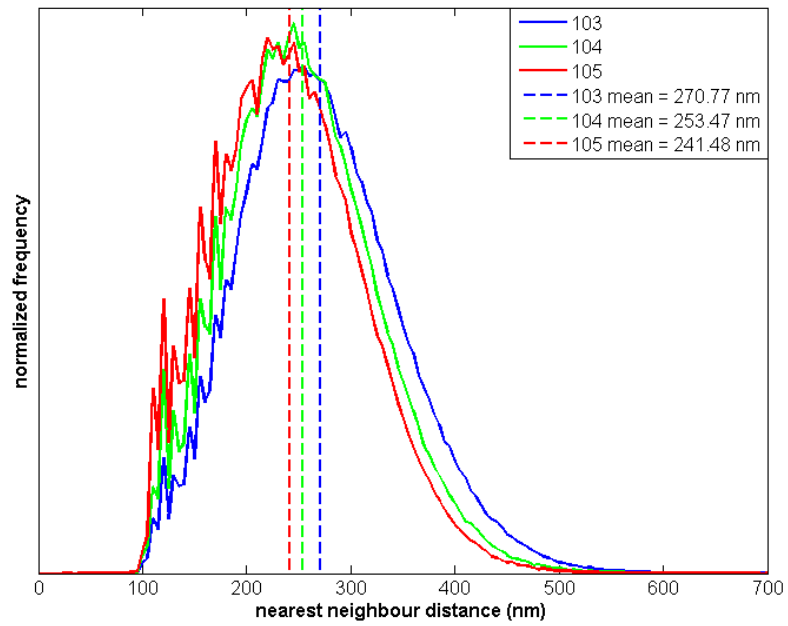
The primary motivation for this analysis was to establish any additional dependence of microscopic properties on the spreadability of the paint coatings. The NN distributions of the samples are calculated and shown in figure 4.7(a). Figure 4.7(b) shows the fitted PDF curves whose shape and scale factors are displayed in table 4.2 alongside the number density, mean NN values and clustering factors for each sample.

The mean values demonstrate a reduction in the spacing of the TiO_2 particles alongside an increase in clustering with increasing extender size. This is a consequence of the increased number density of the TiO_2 particles.

The series of peaks shown in the small values of the NN distribution in figure 4.7(a) are the consequence of the discretization of allowable distances between barycentres in the voxelized image. The distribution is smoother with increasing distance due to the voxel size being small in comparison.

A plot of spreadability against the mean NN distance and the clustering factor R_n is shown in figure 4.8. This increased clustering allows for a larger spreadability owing to the additional

(a)



(b)

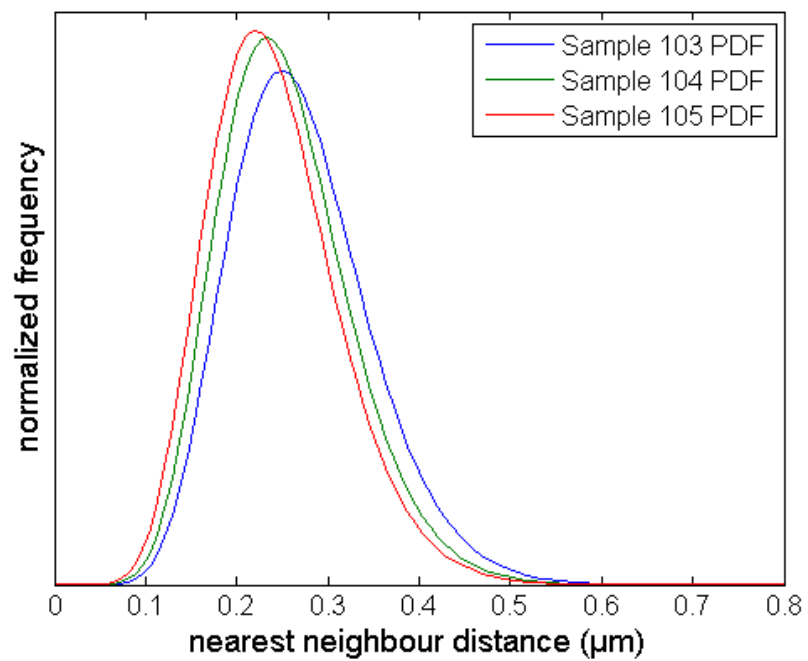


FIGURE 4.7. (a) Histogram of the NN distribution of the 3View images at the lowest magnification. (b) Fitted PDFs of the histogram data in (a).

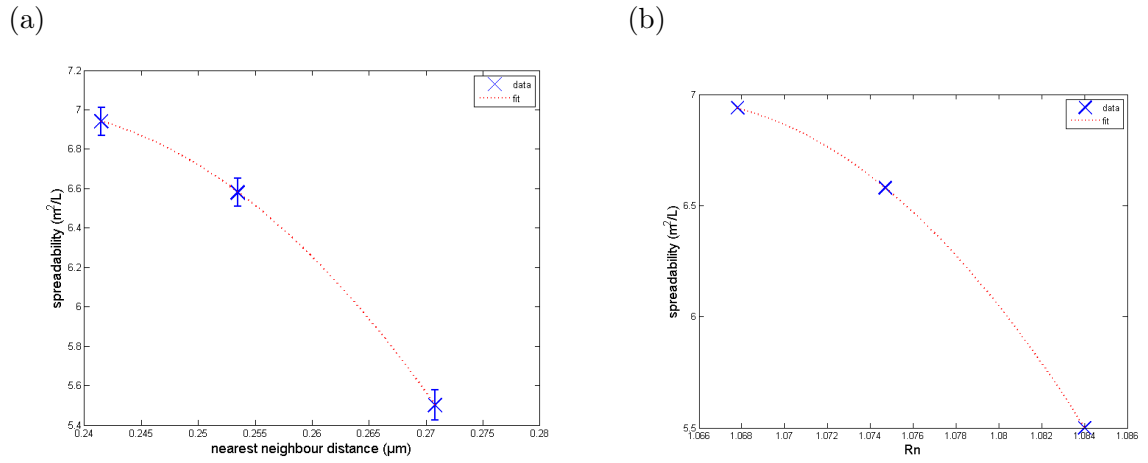


FIGURE 4.8. (a) Mean NN distance plotted against spreadability. (b) Clustering factor R_n plotted against spreadability.

hiding power of a tightly packed distribution of pigment. With increasing size of extender, the free space for the pigment is reduced whilst the volume fraction of pigment remains constant.

The limited number of data points will limit the degree of the polynomial capable of fitting the data as many polynomials of higher order will not have unique solutions. The quadratic fit for the data takes the form:

$$S = -1.106 \times 10^3 \langle D \rangle^2 + 5.1739 \times 10^2 \langle D \rangle - 53.504 \quad (4.2)$$

where S is the spreadability in m^2L^{-1} and $\langle D \rangle$ is the mean NN distance in μm . This function has a maximum at $0.234 \mu\text{m}$, which is very close to the desired effective diameter of the TiO_2 . Assuming identical spherical particles, this maximum in spreadability coincides with the physical lower limit of the NN distance.

Comparing the clustering factor with the spreadability can also be modelled with a quadratic equation of the form:

$$S = -3947.8R_n^2 + 8406.1R_n - 4467.8263232 \quad (4.3)$$

Additional samples and scans may reveal a weaker correlation than is presented here, although the sample size compares a very large number of particles ($\sim 10^5$) that should account for a representative volume of the material. Validations using both high magnification scans of the 103 sample in the 3View as well as even higher magnification in a FIBSEM are performed. Increasing the magnification is done to ensure consistency in the lower length scales, but also to reduce the slicing artefacts produced which disallow adequate quantification of the volume and shape distributions. These artefacts arise from an inability of the ultramicrotome to slice the TiO_2 particles. The particles are ‘swept’ along the slicing direction as demonstrated in figure 4.9(a), which shows a cross section, and figure 4.9(b), which shows how the sweeping motion imposes an elongated shape and misleading orientation. It is, however, quite realistic to posit that the quantified barycentres are simply translated by a similar amount which could have very little effect on the distances between the barycentres at the quantification stage.

2D slices of the high magnification 3View and FIBSEM data are shown in figure 4.10, which reveals a substantial increase in detail and, with the FIBSEM, very clear porosity within the epoxy matrix.

Quantification of the NN distributions, as shown in figure 4.11, for all 3 scans reveals a linear decrease of mean NN with length scale. This is due to the additional resolving power at higher magnifications both in the image itself, but also in the segmentation where particle profiles are more distinguishable and are labelled adequately as shown in figure 4.12.

Downsampling the FIBSEM data and quantifying the NN distribution reveal a good agreement with the low magnification 3View data as shown in figure 4.13. This suggests that the smaller sample size of the FIBSEM data is still a representative volume, which can be used to quantify volume fraction, size, shape, NN orientation and PCF as shown in figure 4.14. The volume fraction is found to be 22% and in figure 4.14(a), the effective diameter distribution is

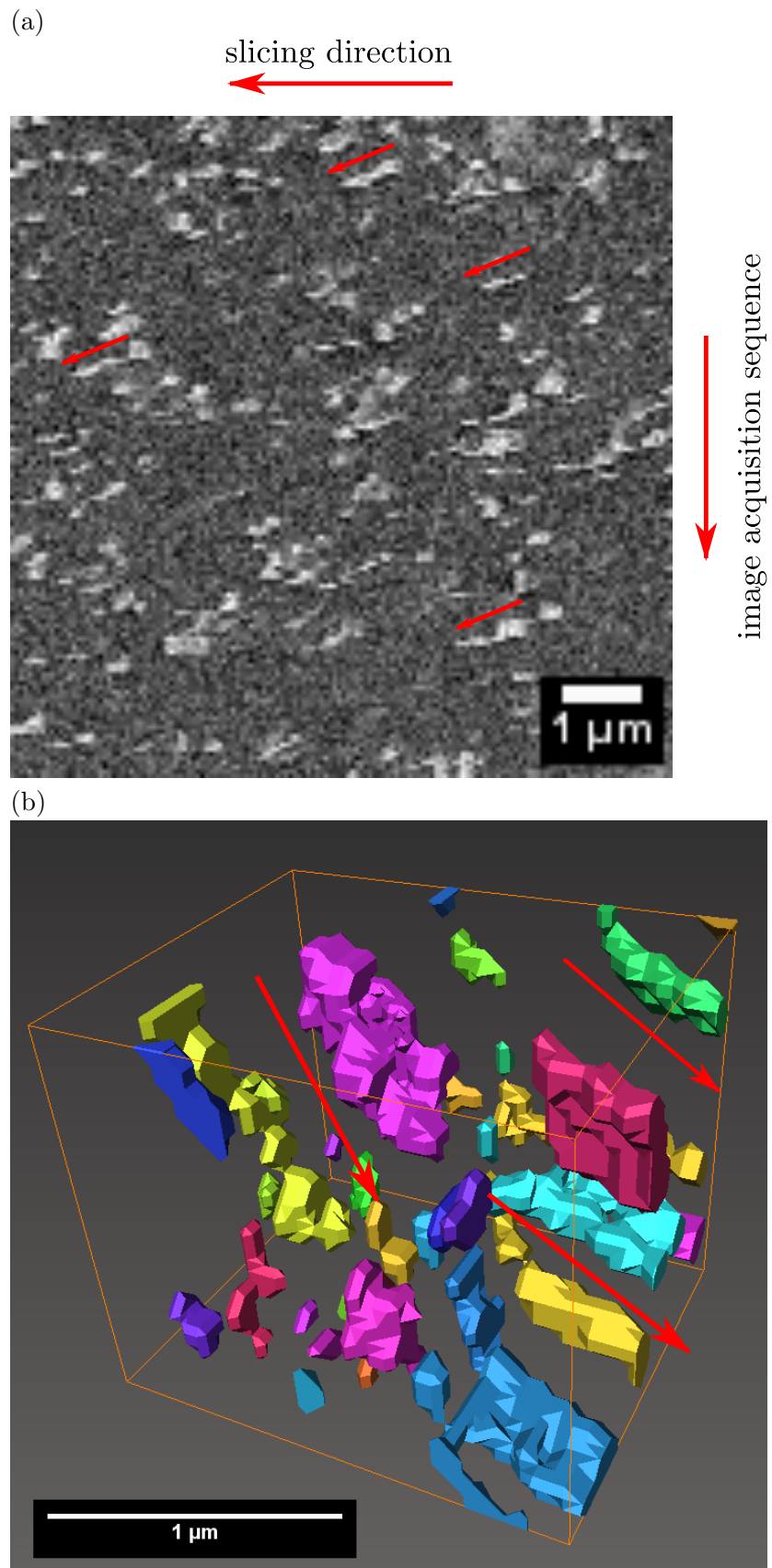


FIGURE 4.9. (a) Cross section showing the sweeping of TiO_2 by the ultramicrotome. (b) Surface rendering of the labelled low magnification 3View settings showing the impact on particle shapes. The scale bars are $1\mu\text{m}$.

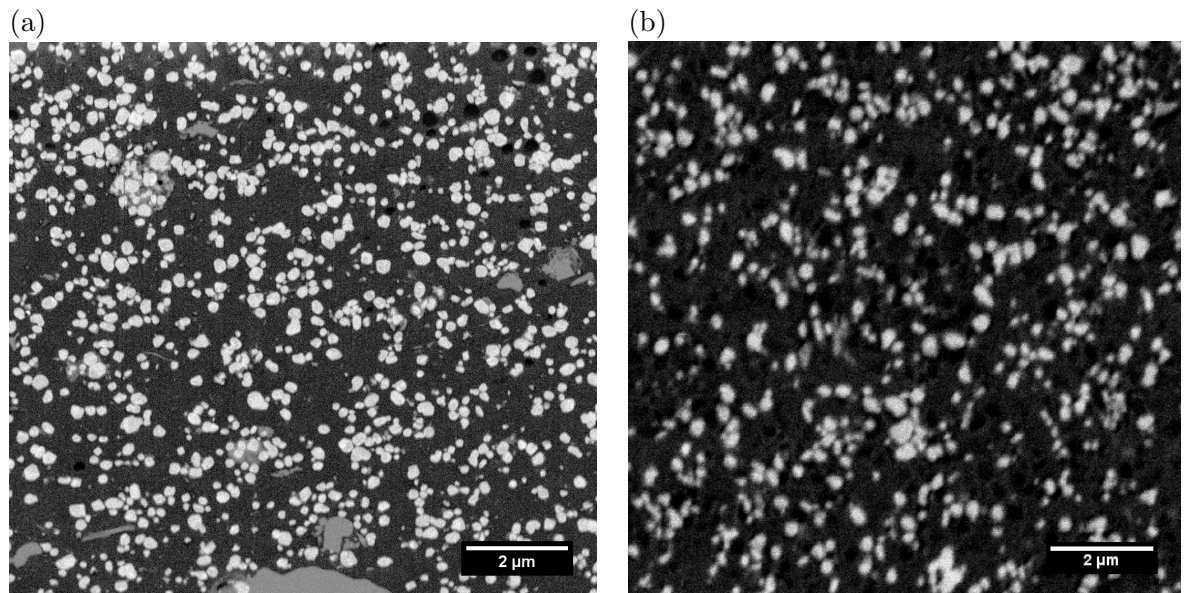


FIGURE 4.10. (a) Single slice of sample 103 as acquired by FIBSEM. (b) Single slice of sample 103 as acquired by 3View using the high magnification settings. The scale bars are $2\mu\text{m}$.

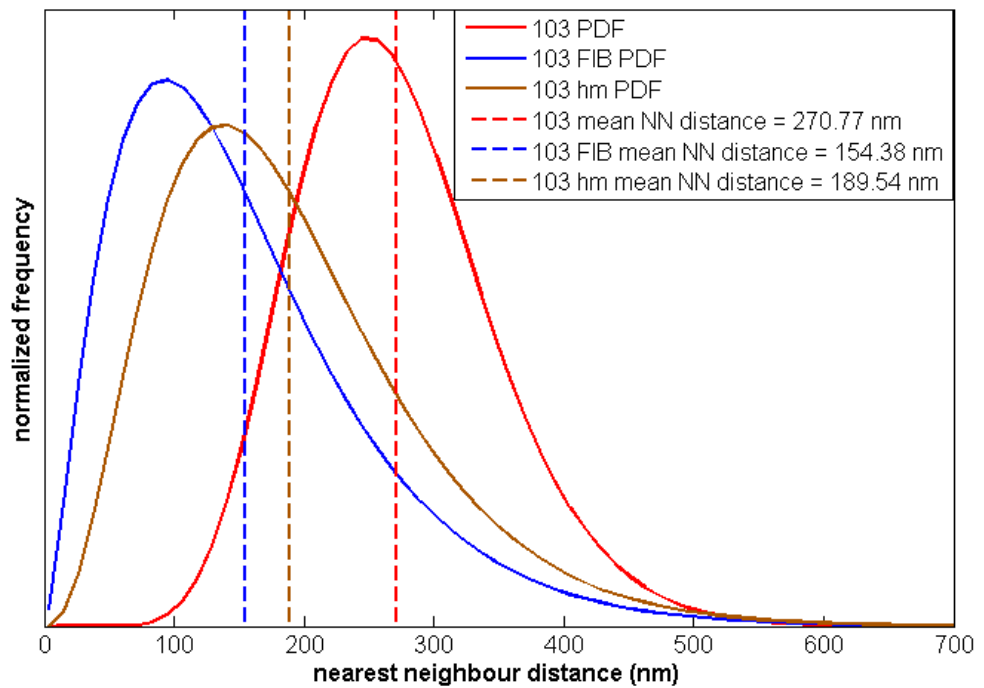


FIGURE 4.11. Quantification of NN distribution using both magnifications used in the 3View as well as the FIBSEM data.

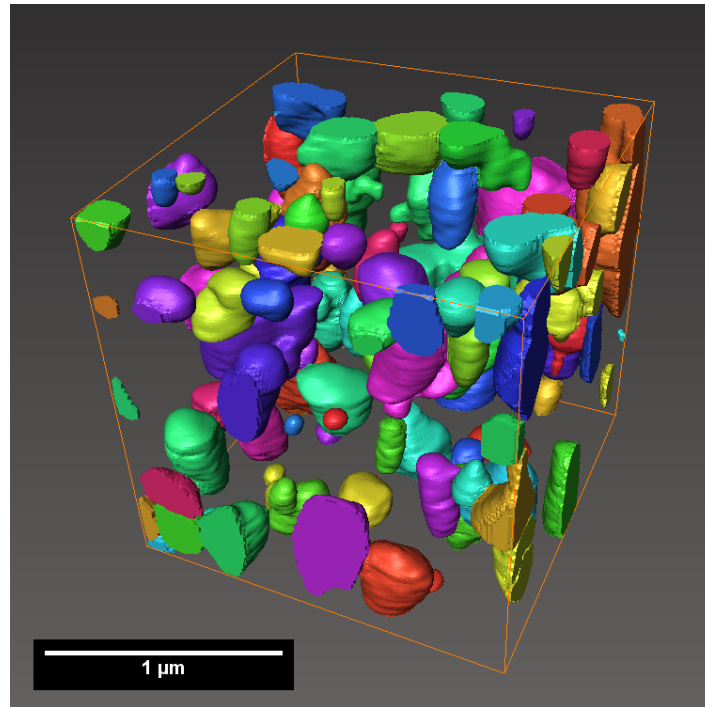


FIGURE 4.12. Surface rendering of the labelled FIBSEM data.

shown to peak below the optimum $0.23 \mu\text{m}$ size. Plotting NN against the effective diameter distribution for the data, as shown in figure 4.14(b), reveals some particles having a larger effective diameter than the NN distance. These points lie above the black line indicating the equality of NN and effective diameter. This can arise due to small particles being adjacent to larger particles, or due to the shape of one or both neighbouring particles allowing the effective diameter to extend beyond the actual boundaries of the particle. Figure 4.14(c) is a scatter on a unit sphere, showing the direction of the NNs coloured by the distance. Overall, an isotropic orientation is observed with the discretization becoming apparent at the poles of the plot for the low values of distance. Figure 4.14(d) shows the global PCF of the particles exhibiting peaks at regions of increased particle density. The PCF exponentially decreases and tends to 1 for large distances; in this case, distances $\gtrsim 0.15 \mu\text{m}$.

Figure 4.15 shows a simplified 3D structure composed of ellipsoids that correspond precisely with the 3D quantification results from the FIBSEM data. Such information can be used to produce simplified FE meshes of real systems that can simulate light scattering by the

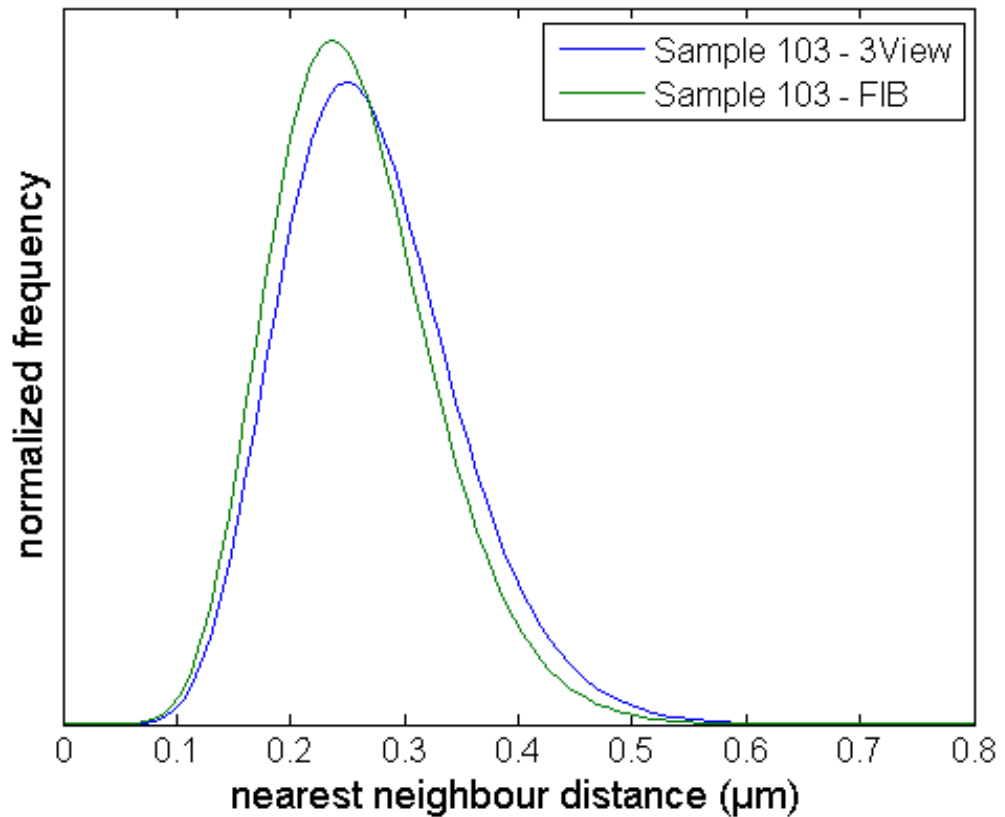


FIGURE 4.13. Comparison of the 3D NN distributions as calculated from the 3View data and the down-sampled FIBSEM data.

Moment Method (see 4.2.3). This approach may be advantageous due to the simplified nature of the mesh, ensuring a quicker convergence time and, therefore, allowing a larger system for the same computing time.

TABLE 4.2. The shape and scale factors of the fitted PDFs alongside the number density, mean NN distances and clustering ratio R_n of the NN distributions for the low magnification 3View images.

Sample name	Shape (a)	Scale (b)	Number density (nm^{-3})	Mean NN (nm)	R_n
103	12.4512	21.7462	1.09×10^{-8}	271	1.0840
104	12.3587	20.5093	1.30×10^{-8}	253	1.0747
105	11.4608	21.0702	1.47×10^{-8}	241	1.0678

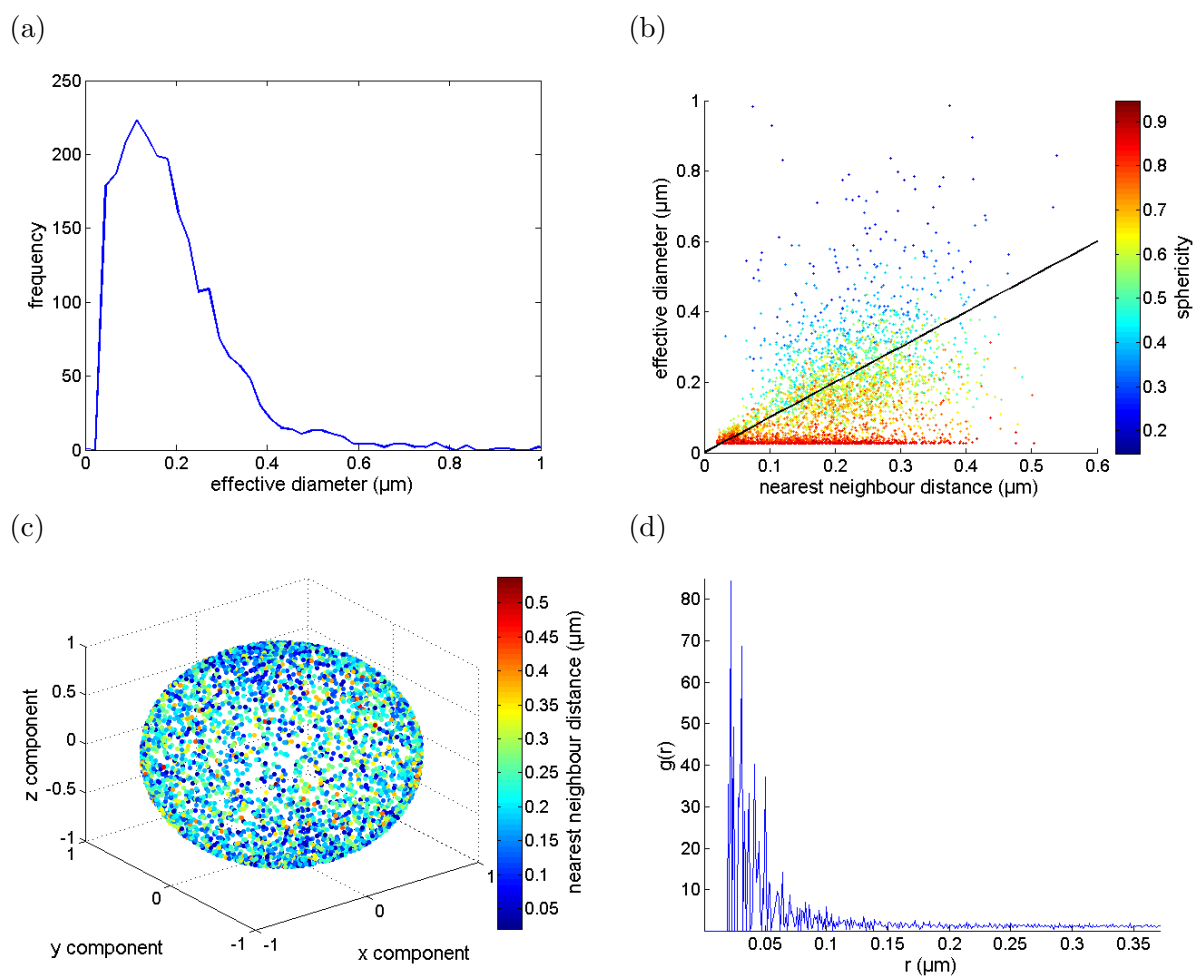


FIGURE 4.14. Quantification of the FIBSEM data: (a) The effective diameter distribution. (b) NN versus effective diameter scatter. (c) NN isoplot. (d) PCF.

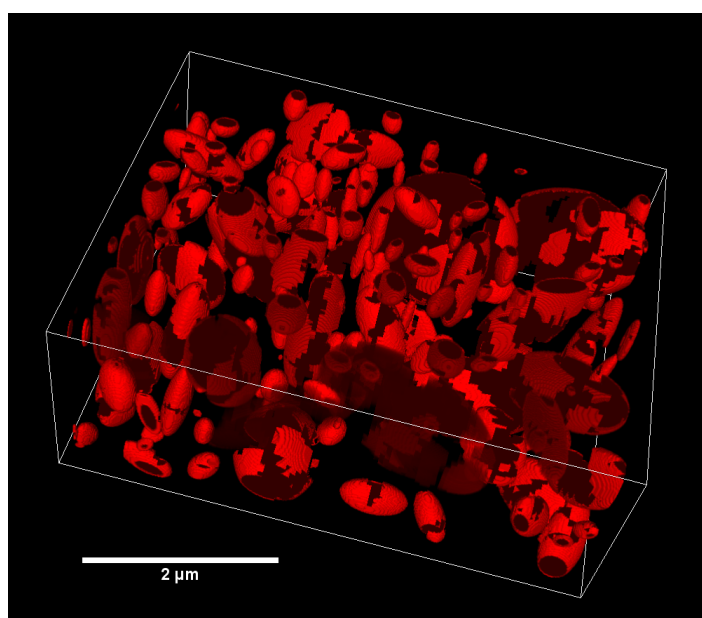


FIGURE 4.15. Fitted ellipsoids generated from the FIBSEM image data.

4.8 Conclusions

Three domestic paint samples have been quantitatively characterized using 3D imaging techniques with particular interest in the relationship between spreadability and the respective NN distributions. In principle, this information can also be related to opacity of the coatings due to the relationship between hiding power and spreadability.

It is clear from the investigation that 2D imaging techniques are not sufficient to determine the particle spacings accurately, particularly with respect to the NN distributions, but also the PCFs and shape distributions. All systems showed a clustering factor (R_n) close to a random arrangement of particles, but with a variation in line with the proposed analytical model (equation 4.3). A potential dependence of spreadability with mean NN distance is shown (figure 4.8) and an analytical model has been used to fit the data (equation 4.2). The proposed analytical model is one of many possible models for the available data and, with respect to extrapolation, further systems should be quantified that fall outside the limits of the current data.

Results for NN distributions obtained from the 3View system have been validated at lower lengths scales by using 3D images obtained in a FIBSEM. In addition to the NN distributions, a variety of other quantification data to fully characterize the TiO_2 particles has been produced (figure 4.14). The FIBSEM overcomes certain issues associated with the mechanical slicing of the paint samples so that size and shape distributions are reliable.

Chapter 5

Multi-scale Tomographic Characterization of Inhibitors in Protective Aerospace Coatings

5.1 An introduction to corrosion inhibition

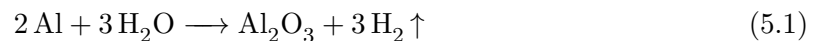
5.1.1 Corrosion

In general, corrosion is defined as “*a heterogeneous redox reaction at a metal-nonmetal interface in which the metal is oxidized and the nonmetal reduced*” [148]. This can be written in the following manner:

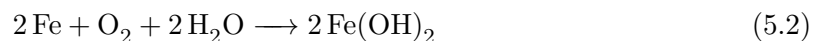


In this respect, corrosion can be seen as the oxidation of a metal and the simultaneous reduction of a non-metal. It is noted that such reactions take place in the presence of an electrolyte to allow for an ionic current on the metal surface. This is necessary for the continuation of the electrochemical reactions that constitute corrosion (see later).

For aluminium, some possible corrosion reactions are the formation of alumina (Al_2O_3) which can be considered as the oxidized metal *and* reduced non-metal:



For iron, there is the production of ferrous hydroxide by the following:



These reactions, however, do not happen spontaneously and rely on two ‘half-reactions’ which occur at the so-called anodic and cathodic sites [119]. At the anode we have the dissolution of a metal which, in general, can be expressed as:

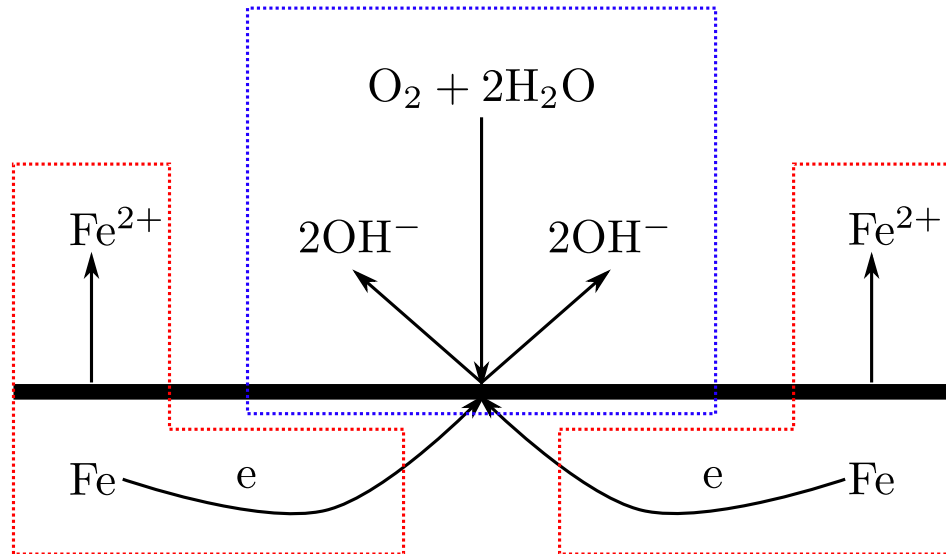
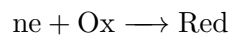


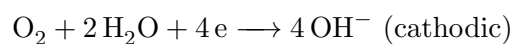
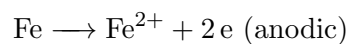
FIGURE 5.1. The two half reactions involved in the corrosion of iron with the anodic reactions in red and the cathodic reactions in blue.



At the cathode, we have a reduction reaction which may be expressed in the following generalized manner [149]:



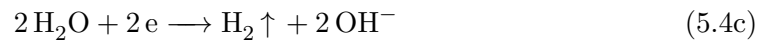
The commonly illustrated example of how iron corrodes is reproduced here in figure 5.1 [150], which shows how equation 5.2 is divided into the two half reactions below:



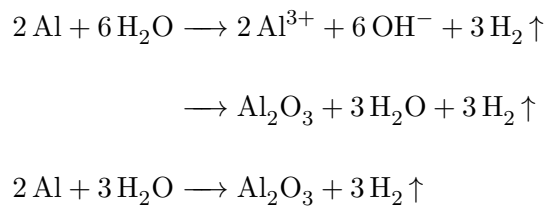
For aluminium (Al) we have the following anodic reaction:



There are also a number of corresponding cathodic reactions as follows:



Combining the anodic and cathodic reactions, for example, equations 5.3 & 5.4c, it is possible to derive equation 5.1 showing the production of alumina from the corrosion of aluminium as follows:



Approaches to corrosion inhibition are either to control the rates of the anodic or cathodic reactions or both, which determine the classification of the inhibitor material [149, 151].

5.1.2 Inhibition of corrosion

As defined by BS EN ISO 8044:2000 [152], ‘a corrosion inhibitor is a chemical substance that, when added in small concentration to an environment, effectively decreases the corrosion rate

without significantly changing the concentration of any corrosive agent.’ Some other definitions are more general, for example, simply ‘any compound that suppresses corrosion’ [149]. All corrosion inhibitors (CIs) operate by affecting one or both of the half reactions discussed in section 5.1.1. As both the anodic and cathodic half-reactions are required for corrosion to continue, CIs can be categorized by which of the two half-reactions are affected.

Therefore, anodic inhibitors are ones that directly affect the rate of the anodic half-reaction and, conversely, cathodic inhibitors affect the rate of the cathodic half-reaction. So-called mixed inhibitors act both at anodic and cathodic electrode sites to reduce corrosion rates as shown in figure 5.2. The reduction in corrosion rate at the electrodes shifts the corrosion potential to provide protection. How the corrosion rate is reduced is either by [149]:

1. lowering the rate of dissolution of metal ions into the solution (‘polarization’)
2. reducing the size of the electrode (‘passivation’).

Specifically, anodic inhibitors react with the corrosion products (M^{n+}) to produce an insoluble, adhesive film known as a passivation layer [153]

It is noted that cathodic inhibitors can only reduce corrosion rates by decreasing rates of: (i) oxygen ionization, (ii) transport of oxygen (iii) discharge of hydrogen ions. Cathodic inhibitors cannot passivate cathodic sites [149].

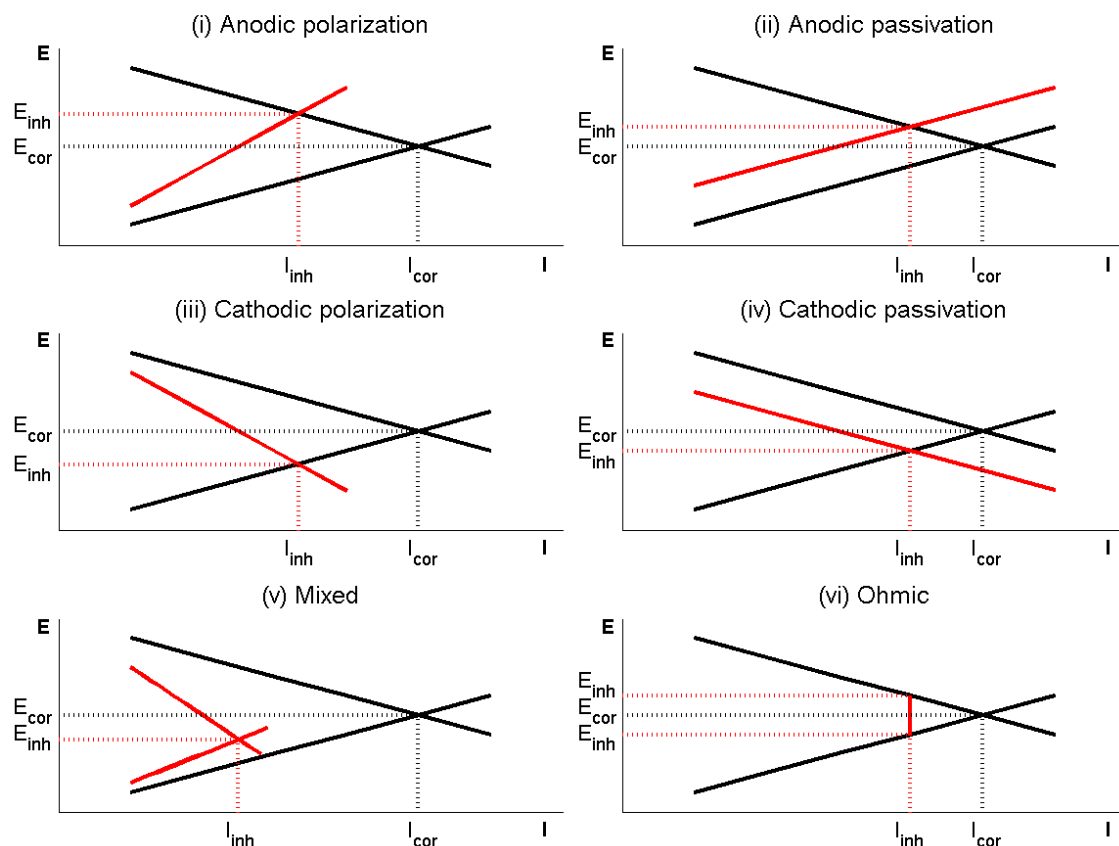


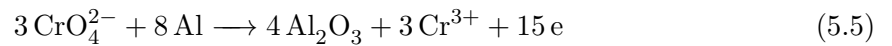
FIGURE 5.2. Evans diagrams showing how CIs influence the corrosion rates by affecting the anodic and/or the cathodic reactions [2].

5.2 Mechanism of Chromate Inhibition

Owing to the strong oxidizing ability of dichromate ions (CrO_4^{2-}) [154, 155], chromates have long been used as a CI for a large variety of metals [2, 149, 150, 156–159]. Early investigations have found chromates to be cathodic inhibitors in acidic environments and anodic in neutral and alkaline environments [160]. Additionally, chromates are ‘dangerous’ such that they are required in sufficient quantities to prevent localized corrosion, which can be accelerated in suboptimal concentrations of inhibitor [161].

Two main mechanisms of corrosion inhibition by chromates are proposed in the literature [159, 162–164], but both involve the formation of a passivation layer. The first proposed mechanism involves the reaction of chromate species with soluble metal salts to provide a protective film

of hydrated metal and chromic oxides. For aluminium this occurs by reactions 5.5 [162] and 5.6 [164].



Reaction 5.5 and 5.6 both show the formation of an alumina film with the additional formation of chromium(III) oxide in reaction 5.6. This passivation film adheres to the metal surface and slows or prevents the formation of corrosion products at anodic sites. The alternate proposed mechanism involves the adsorption of chromate ions on the metal surface, thus reducing the activity of the metal at the anodic site [159].

Owing to the carcinogenic nature of hexavalent chromium, its use has become diminished with the exception of cases where chromate replacement materials have not been established. Particularly, its use in the aerospace industry as an inhibitor pigment in primer layers applied to aluminium alloys is ongoing. Typically, a full coating system for such applications involves a conversion coating, a primer coating and a top coat [165] with the primer containing strontium chromate (SrCrO_4) particles.

Figure 5.3 shows a simplified system with just the primer and the metal substrate. The process of forming a passivation layer to protect the metal substrate at a created defect site involves both the transport of the inhibitor material in addition to the chemical interactions that take place at the defect site. The transport mechanism of inhibitors as pigments in organic coatings is a relatively new area of investigation, but it is critical in determining the performance of

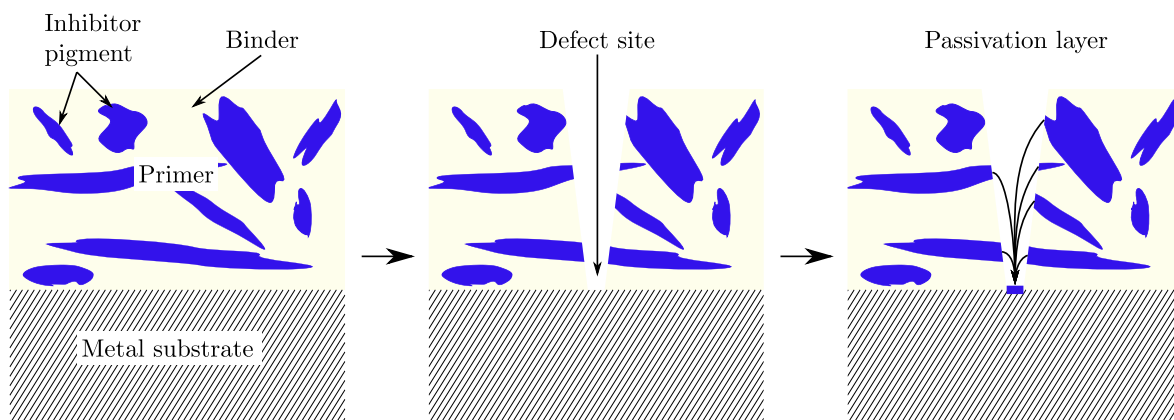


FIGURE 5.3. The formation of a defect site in a primer layer coating applied to a metal substrate followed by the formation of a passivation layer at the defect site.

the coating. For example, release kinetics can be used to estimate concentrations at potential corrosion sites to avoid accelerated localized corrosion as well as to inform lifetime estimates and maintenance regimes.

5.3 Transport of Chromate Inhibitors

Investigation into the transport behaviour of inhibitors in epoxy primer coatings is a relatively new area of research. Initial investigations involve immersing primer systems in a so-called leaching solution (also known as the ‘leachate’) to allow the dissolution and subsequent egress of inhibitor material from the epoxy matrix within the leachate. A number of experiments have focused on the study of the leachate and the change in its composition over time [4, 166–169]. For example, Prosek and Thierry investigated the release rates of chromate species as a function of temperature and pH as a model of inhibitor transport using ion chromatography to measure the release of chromate into the leachate [166]. The transport behaviour is assumed to be dominated by “diffusion of water and chromate solution through the ... primer” [166]. In contrast, Sellaiyan et al. have used radio-tracers to observe the cessation of chromate release after 6 days, which coincides with a substantial drop in the free volume as determined by Positron Annihilation Lifetime Spectroscopy (PALS). This investigation also coupled SEM to

observe depletion profiles of the coating, which showed non-uniform leaching of the inhibitor material [169].

Analytical models can be used to fit data obtained during leaching experiments to model the quantity of released inhibitor material. Doing so may hint at the specific physical mechanism(s) taking place during inhibitor release. Kim et al. provided a review of analytical models describing the release of Low and Intermediate Level Waste (LILW) from nuclear power plants [170]. As with SrCrO_4 particles distributed in an epoxy binder, the LILW forms ‘cells’ in a binder that can allow some transport of the LILW. A shrinking core model (SCM) was found to accurately describe the results for the release rates of LILW and it has also been used to describe the release kinetics of SrCrO_4 in organic coatings [171].

Furman et al. compared real leaching data from coated panels of aluminium alloy (AA2024-T3) with a selection of models used by Kim et al. [4, 170]. The first model is a simple power law of the form

$$M(t) = kD_{\text{eff}}t^n \tag{5.7}$$

where M is the molar quantity released after time, t . D_{eff} is the effective diffusion coefficient, k is a constant and $n = 0.5$ for Fickian diffusion. Under this mathematical model, the proposed mechanism is firstly the saturation of the epoxy with water. Following this, chromate dissolves into the solution until it is saturated allowing for a high concentration gradient to form at the primer/solute interface.

Furman et al. observed a behaviour of $n = 0.25$, implying a non-Fickian leaching behaviour. The skin layer* of the primer in addition to changes in porosity and tortuosity were not regarded as being responsible for this observed ‘sub-diffusion’ behaviour [4].

*That is to say, the layer of epoxy *not* containing any pigment typically found at the interface of pigmented organic coatings.

An alternative to the aforementioned power model (equation 5.7) is a generalized empirical model of the form:

$$M(t) = \sum_{i=0}^n A_i t^{i/2} \quad (5.8)$$

where A_i are empirically determined constants (see equation 5.9 for examples).

A third order empirical model physically corresponds to a number of effects that can take place during leaching, which extends the power law model above. The equation governing this model is of the following form:

$$M(t) = A_0 + A_1 t^{1/2} + A_2 t \quad (5.9)$$

Each term of equation 5.9 corresponds to a different physical process. The A_0 term represents the quantity of material immediately in contact with the solution which is dissolved instantaneously on commencement of leaching. The A_1 term represents the diffusive aspect of the kinetics by Fickian diffusion. The A_2 term represents chemical reactions “such as dissolution, corrosion, or solubility control” [170].

In addition, a Shrinking Core Model (SCM) that was first used to describe the combustion of carbon particles [172, 173] is used as a model for the release data. The SCM for both spherical and cylindrical particles is described by equations 5.10 and 5.11 respectively. The release fraction $\alpha(t) = M(t)/M(0)$ is a function of time, t , and k is an experimentally determinable constant [4, 174].

$$\alpha(t) + (1 - \alpha(t))\ln(1 - \alpha(t)) = kt \quad (5.10)$$

$$1 + 2(1 - \alpha(t)) - 2(1 - \alpha(t))^{2/3} = kt \quad (5.11)$$

The physical correspondence of the model to a hypothesized shrinking of an inhibitor particle appears sensible although it would seem that the analogue for the ‘ash’ layer in the case of a SrCrO_4 particle is not present.

Furman et al. did not find appreciable differences in the goodness of fit between these three models and the experimental data. The respective χ^2 values for each tested model is reproduced in table 5.1, showing that the polynomial model (equation 5.9) is the best fit with the data and it is followed very closely by the power law model (equation 5.7).

TABLE 5.1. Analytical models and their respective χ^2 values for the leaching data [4].

Analytical model	χ^2 (10^{-4})
Polynomial	7
Power ($t^{0.275}$)	8
SCM (spherical)	10
SCM (cylindrical)	44

Following on from this work, it is, therefore, necessary to not only fit experimentally obtained leaching data with selected analytical models, but to also observe the small scale behaviour and distribution of the inhibitor particles by imaging. Although Sellaiyan et al. [169] have used 2D SEM to observe the non-uniform depletion of inhibitor material in cross sections of primer systems, Hughes et al. have initiated the exploration of this problem using 3D imaging techniques utilizing both XRT and SBFSEM to quantitatively characterize the SrCrO_4 particles during leaching [175, 176]. These techniques can reveal the connectivity of the inhibitor material and explain the observed non-uniform depletion as being the result of connected transport paths through the primer. This connectivity can be through contact points of the inhibitor particles allowing the formation of clusters, or through voids that can be pre-existing or be created by the dissolution of an inhibitor particle/cluster.

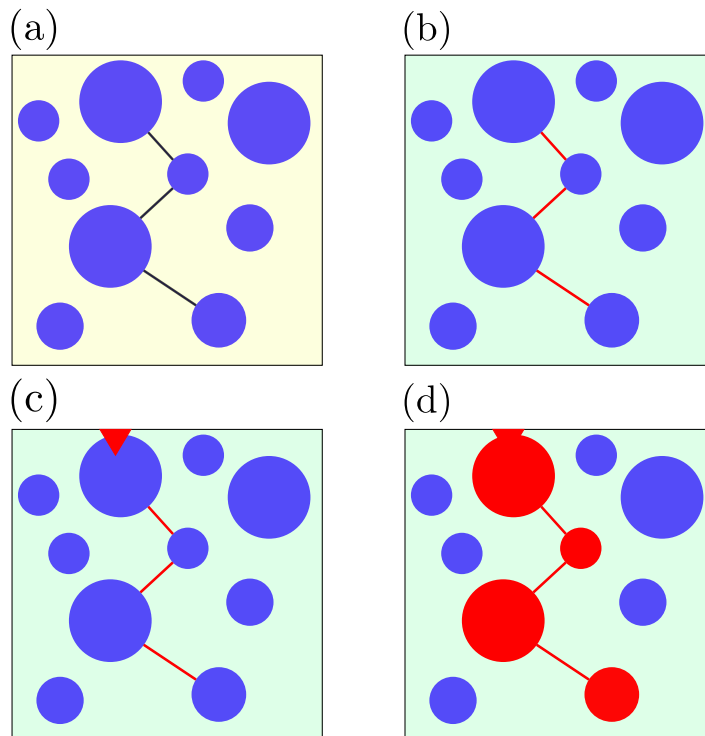


FIGURE 5.4. A schematic of the transport mechanism by connected clusters. (a) An epoxy matrix (yellow) with inhibitor material (blue) and connectivity between particles by void space (shown in black). (b) An epoxy matrix saturated with water (green) and void spaces filled with water (red). (c) The creation of a defect in an aqueous environment. (d) The depletion of inhibitor material connected to the defect site with the depleted inhibitor material replaced with water-filled void (red).

In line with the proposed transport mechanism discussed in the literature, figure 5.4 shows a series of events which take place during a leaching experiment. Initially, the primer system is saturated with water (figure 5.4(b)); however, no material is released[†] until a defect site is created (figure 5.4(c)). A transport route from the defect site will then form allowing the full depletion of any connected clusters of inhibitor material (figure 5.4(d)).

With respect to the final stage in figure 5.4, it is important to understand the dissolution rates of the inhibitor material followed by the diffusion of the inhibitor-containing solute out of the system through a connected transport route. Hughes et al. proposed a relationship between the self-similar structure of the inhibitor clusters and the dissolution and diffusion rates of the inhibitor material. To this end, 3D imaging has been performed and the inhibitor clusters quantitatively characterized. One such quantity is the Minkowski-Bouligard dimension [177]

[†]With the exception of material immediately in contact with the external aqueous environment.

(herein referred to as the ‘fractal dimension’) of the clusters, which allows data collected at a particular length scale to be converted into a scale invariant quantity. Hughes et al. analysed the 5 largest clusters and, using the Box Counting Method (BCM) [178], found them to have fractal dimensions between 2.24 and 2.36 [175, 176].

The fractal dimensions of the clusters, m , relate the spatial extent of an object, L , to its volume V in the following manner:

$$V(L) \sim L^m \tag{5.12a}$$

$$\log(V) = \log(a) + m\log(L) \tag{5.12b}$$

where a is some constant related to the proportionality of V with L^m .

It is suggested that the leaching behaviour of the system is related to the fractal dimensions of the inhibitor clusters such that a relationship between n (equation 5.7) and m is proposed.

5.4 Experimental and Analytical Methods

Ex-situ sXRT leaching experiments have been undertaken at I13 Imaging beamline at DLS to reveal the distribution of inhibitor pigment before and after exposure to 5% sodium chloride (NaCl) solution for 24 hours. In order to prevent excessive damage to the sample, sXRT was performed close to the k-edge of Sr (16.105 keV) to reduce the dose to the epoxy. The k-edge was found by performing radiography whilst incrementally altering the Bragg angle of the monochromator (thus, altering the beam energy) and measuring the transmission as shown in figure 5.5.

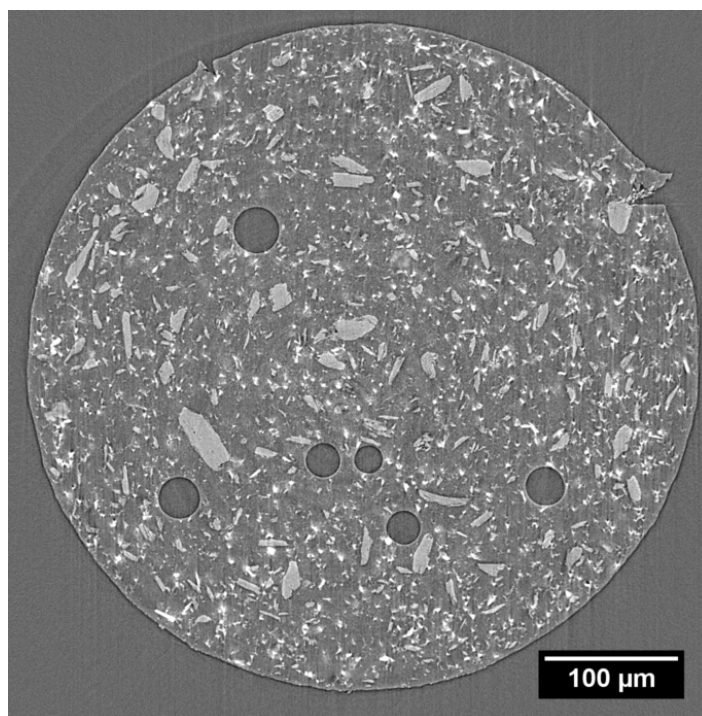


FIGURE 5.6. A single reconstructed slice showing two defect sites at the interface. Highly spherical porosity is also observed alongside SrCrO_4 particles (small & bright particles) and the CaSO_4 particles (large & grey particles.)

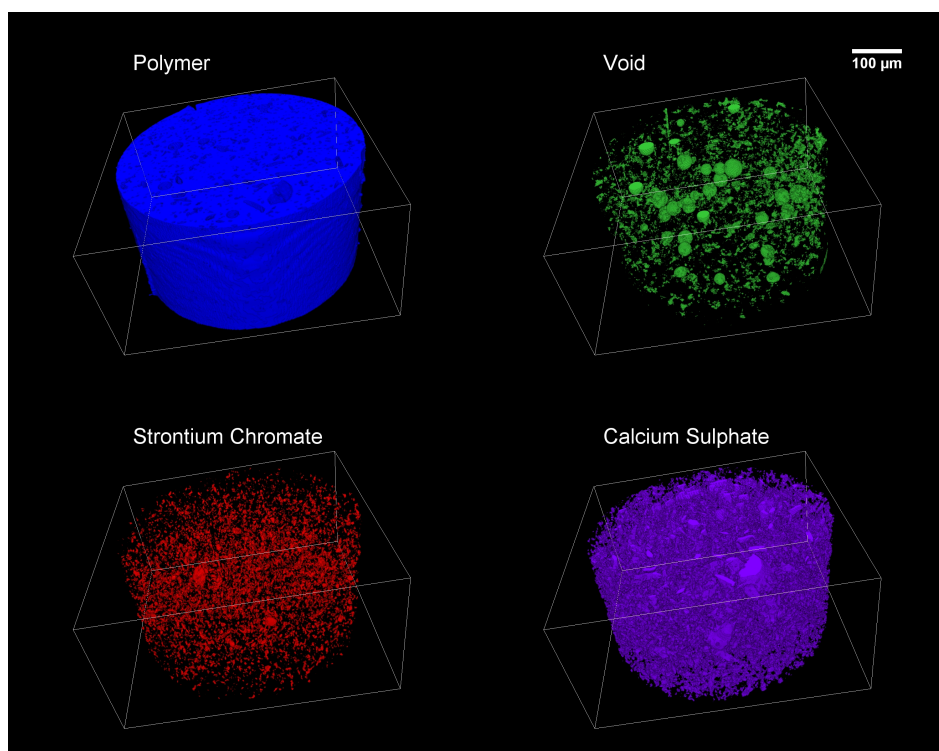


FIGURE 5.7. Segmentation of the phases for quantification.

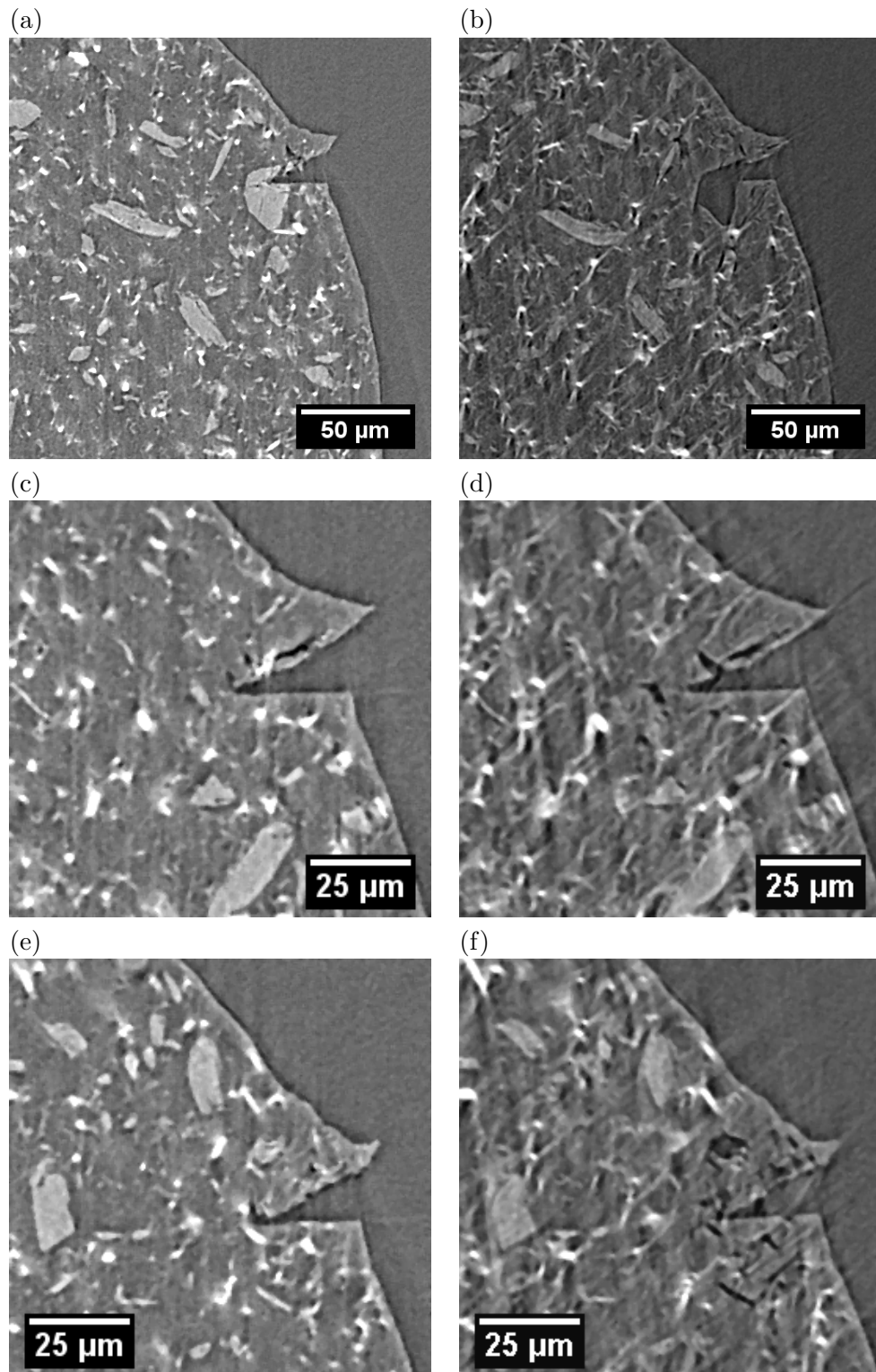


FIGURE 5.8. Slices through the 3D image before (left) and after (right) leaching. Slices correspond to the same ROI as determined by 3D image registration.

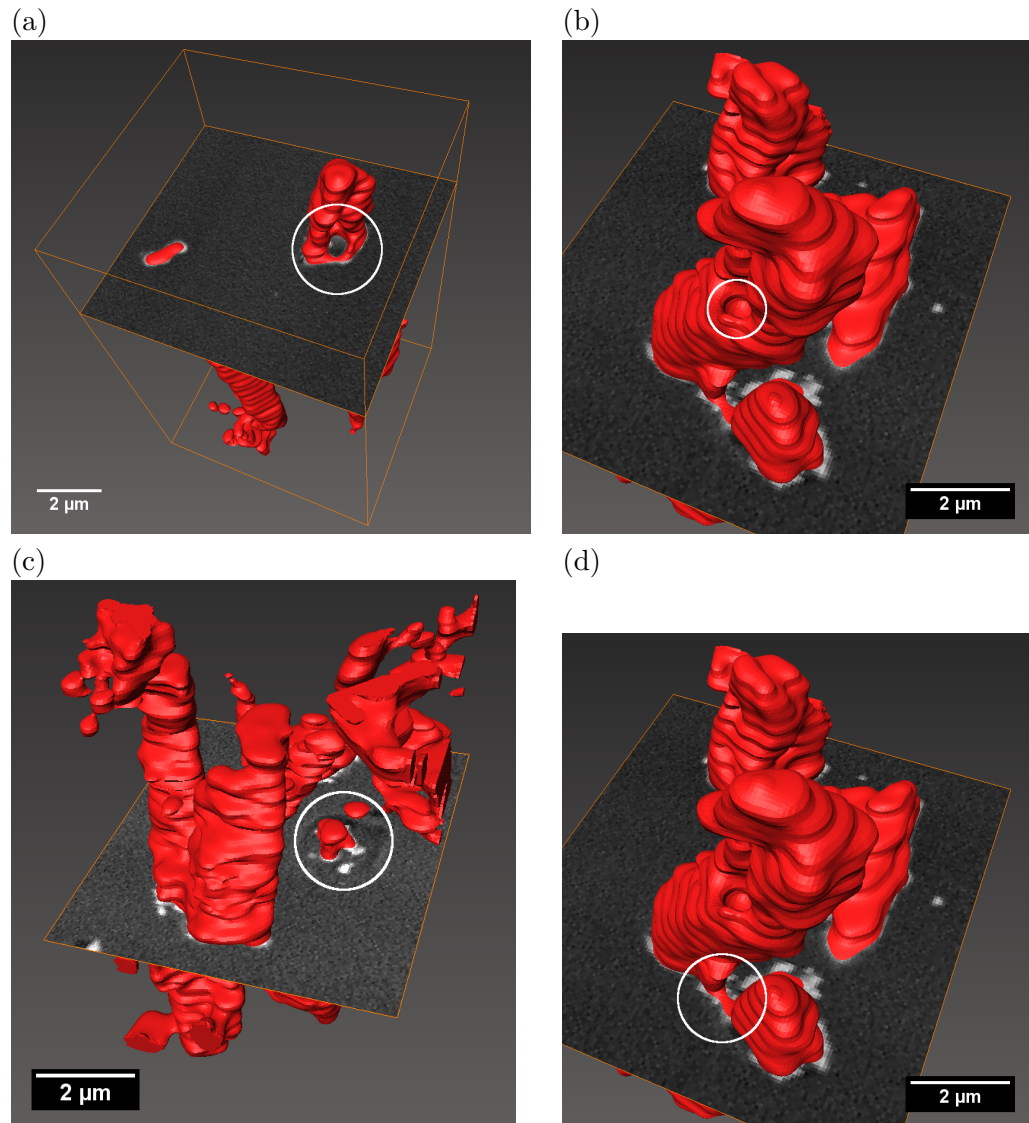


FIGURE 5.9. SBFSEM data showing the depletion of clusters of SrCrO_4 by (a & b) holes as well as (c) shrinking cores; (d) contact points between clusters are also observed.

Volume fractions can be determined by the segmentation of the reconstructed image shown in figure 5.7. Table 5.2 gives an overview of the volume fractions before and after leaching for 24 h as well as the change in volume fraction. The change in epoxy volume could be the result of swelling due to the uptake of water. More interestingly, the egress of CaSO_4 exceeds that of the SrCrO_4 as shown by the image quantification. This result has been validated using ICP-AES showing a leachate concentration of 0.068 mg l^{-1} for calcium and 0.013 mg l^{-1} for strontium.

Figure 5.8 shows slices through 3 different ROIs before and after leaching. The reconstruction

TABLE 5.2. The volume fractions of the respective segmented phases before and after leaching

Material	% Vol. ($t = 0$)	% Vol. ($t = 24$ h)	Change
Epoxy	93.7	94.5	0.8
SrCr	2.17	1.57	-0.6
CaSO ₄	3.47	0.40	-3.07
Pore	0.64	3.54	2.90

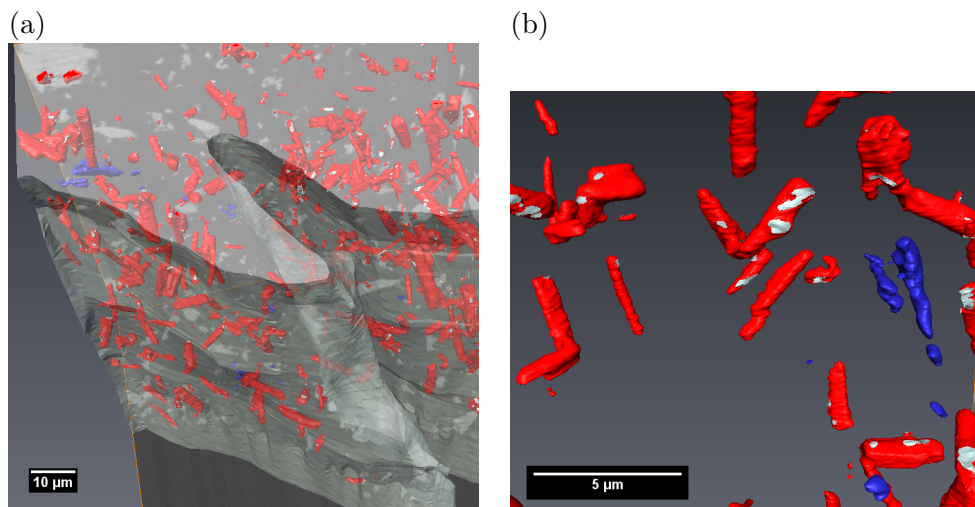


FIGURE 5.10. (a) SBFSEM data of the defect site. The transparent epoxy layer can be seen where the larger SrCrO₄ particles (red) and the voids (blue) are shown. (b) A close-up, rotated view of the largest void shown in (a), demonstrating the transition from SrCrO₄ to void.

in the post-leaching samples does contain artefacts due to a combination of possible factors that all relate to the deformation and movement of the sample during the second scan. Firstly, the heterogeneous removal of inhibitor material changes the internal structure of the coating by replacement of this material with porosity. An instance of this process is shown in figure 5.10. It is also observed that the shape of the leached CaSO₄ particle (figure 5.8a) and the corresponding shape of the pore (figure 5.8b) do not completely match as the structural integrity of the coating has been compromised around the defect site. Secondly, due to the high X-ray absorption cross section of water and the saturation of the epoxy with water after leaching, the dose received by the sample is increased. This is revealed by the differences in contrast between figures 5.8 a, c & e and figures 5.8 b, d & f.

The non-homogeneous leaching behaviour observed by Sellaiyan et al. [169] by SEM is reproduced in figure 5.8. The regions in figures 5.8(e-f) demonstrate almost a complete egress of the inhibitor material within a 25 μm radius from the defect site. However, the other two regions figure 5.8(a-d) show SrCrO_4 particles remaining sometimes very close to the defect site itself, suggesting that a transport path for the egress of the material is not present even in regions of very close proximity.

In line with the SCM suggested by Furman et al. [4], figure 5.9d does reveal an instance of a shrinking SrCrO_4 particle surrounded by void space. However, other leaching behaviour is also observed such as the formation of holes within the SrCrO_4 clusters. This suggests that the dissolution of chromate ions into the solution occurs only at particle-void interfaces. Despite the presence of water saturating the epoxy matrix, dissolution can only take place if the void space is sufficient in size for the transport of chromate.

Fractal dimensions have been calculated from the inhibitor clusters in the 3View and sXRT data, which are displayed in table 5.3. The means by which the data points are fit substantially impacts on the final value for the fractal dimension. Referring back to the proportionality proposed in equation 5.12a, it is worth noting that $\log(a)$ may be non-zero. Therefore, fitting the BCM data (shown in figure 5.11) can be done with a straight line of the form $Y = MX + C$, where $Y \rightarrow \log(N)$, $X \rightarrow \log(l)$, $C \rightarrow \log(a)$ and $M \rightarrow m$. It is noted that using $a = 1$, $\log(a) = 0$, $C = 0$ leads to substantial differences in calculating fractal dimension of the clusters with a mean difference of 0.154 for the 3View data and 0.044 for the sXRT data compared to using a non-zero intercept.

TABLE 5.3. The fractal dimensions of the largest clusters

3View (Y=MX fit)	3View (Y=MX+C fit)	sXRT (Y=MX fit)	sXRT (Y=MX+C fit)
2.2955	2.5863	2.92	2.7681
2.9202	2.7698	2.6021	2.9317
2.657	2.833	2.7711	2.7091
2.6458	2.8849	2.6705	2.5174
2.7371	2.9537	2.7178	2.9744

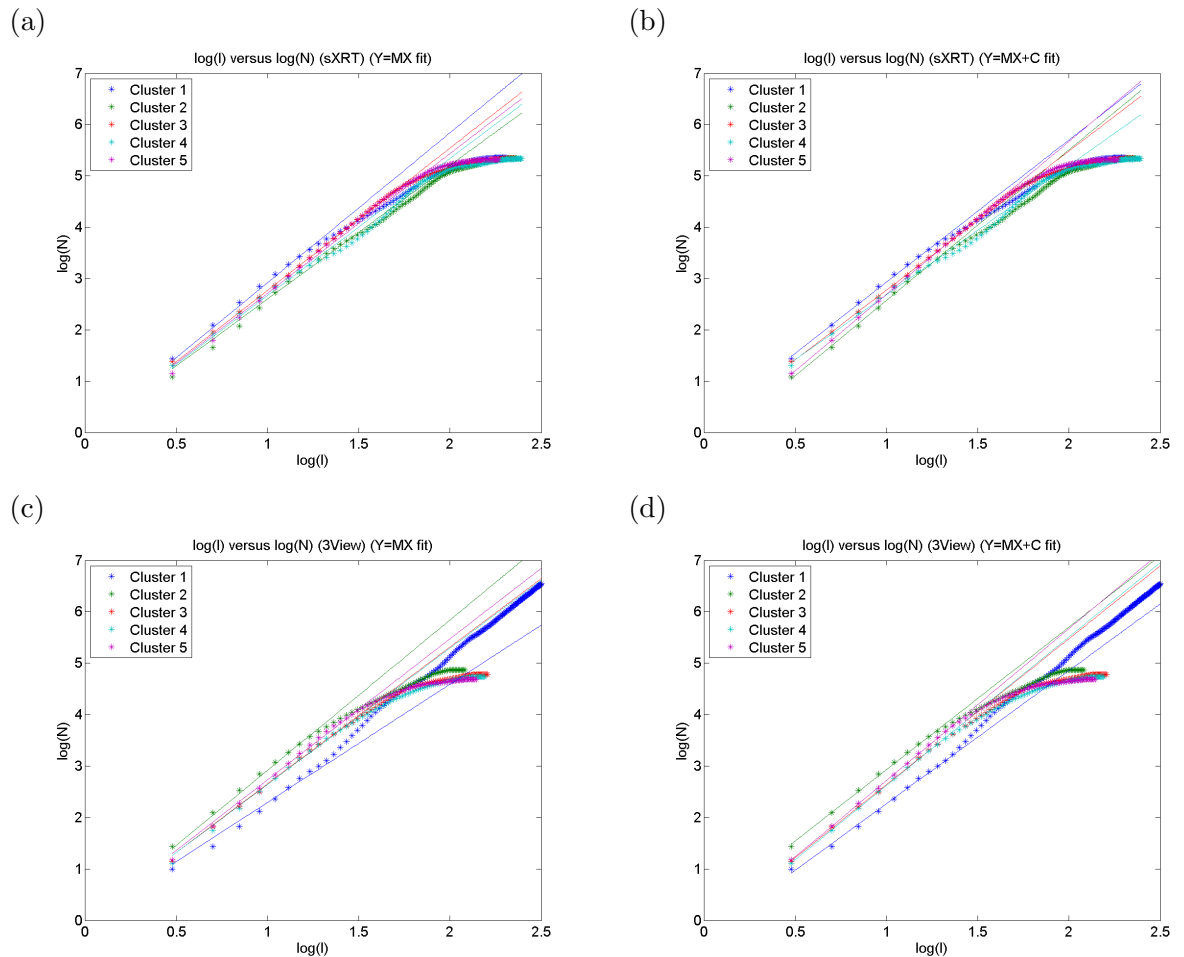


FIGURE 5.11. Fractal dimensions of the largest inhibitor clusters as determined by the box counting method on the segmented sXRT data (a & b) and the 3View data (c & d).

A clear increase in the volume fraction corresponds directly with the effective diameter distribution shown in figure 5.12a. In combination with this, an approximately constant value for the number density ($1929 \rightarrow 2026$) reveals an increase in pore agglomeration and the formation of larger networks. In addition, isolated porous networks, which have corresponding low NN distances, form continuous networks with their NNs, thus increasing the NN distribution generally between other more distant networks. The clustering factor is also shown to evolve from a clustered distribution of pores to a more random distribution as shown in figure 5.12b.

A reduction in the number of SrCrO_4 clusters is observed particularly in the $0.5 \mu\text{m} - 2 \mu\text{m}$ range, which dominate the reduction in volume fraction observed, although larger clusters are also shown to leach (figure 5.13a). The number density is observed to decrease

by approximately one-half (1929 \rightarrow 980), which necessarily implies an increase in the NN distance as shown in figure 5.13b. A slight decrease in the clustering factor reflects the localized depletion of inhibitor surrounding the defect site.

A very large reduction in the volume fraction of the CaSO_4 inhibitor is observed with some larger clusters ($\gtrsim 1 \mu\text{m}$) remaining (figure 5.14a).

The PCF for the CaSO_4 clusters in figure 5.15a exhibits an increased amplitude of the peaks as a result of the reduction in number density. The peaks correspond to high probabilities of finding further clusters for a given distance from an ‘average cluster’. In line with the increased homogeneity of the spatial distribution of the porosity, the PCF in figure 5.15b peaks at a higher distance than the original distribution.

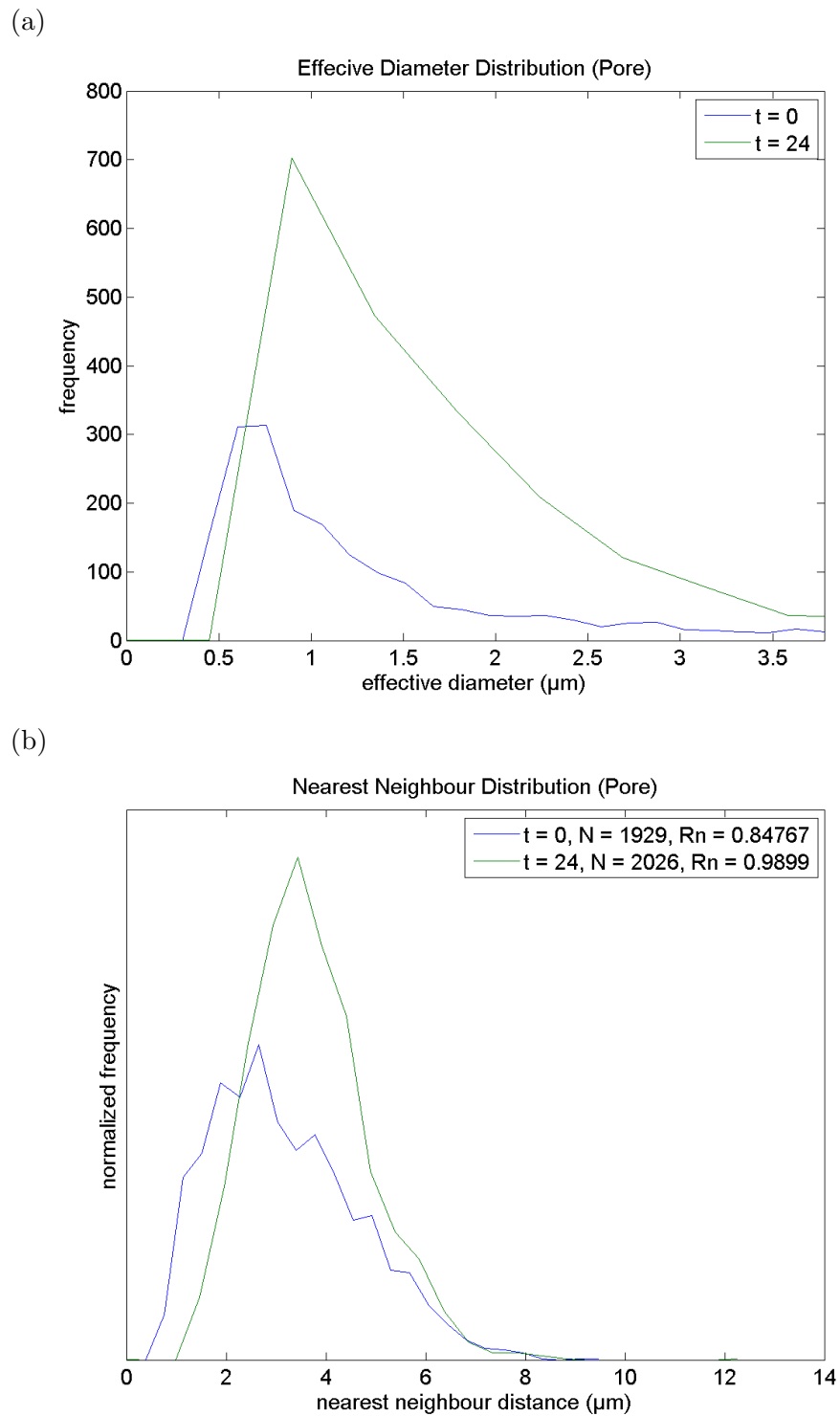


FIGURE 5.12. The effective diameter distribution (a) and NN distribution (b) of the pores before (blue) and after (green) leaching.

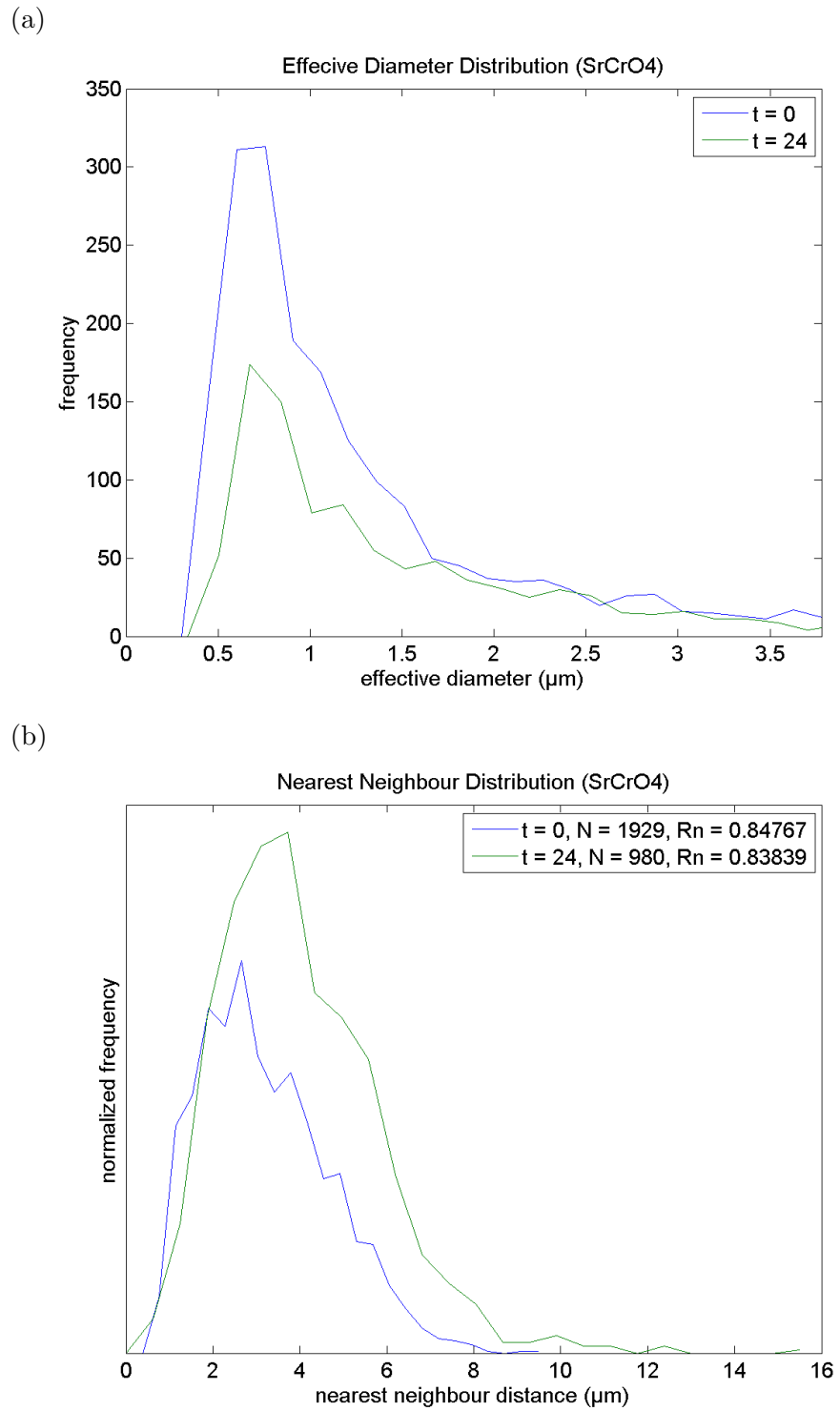


FIGURE 5.13. The effective diameter distribution (a) and NN distribution (b) of the SrCrO₄ before (blue) and after (green) leaching.

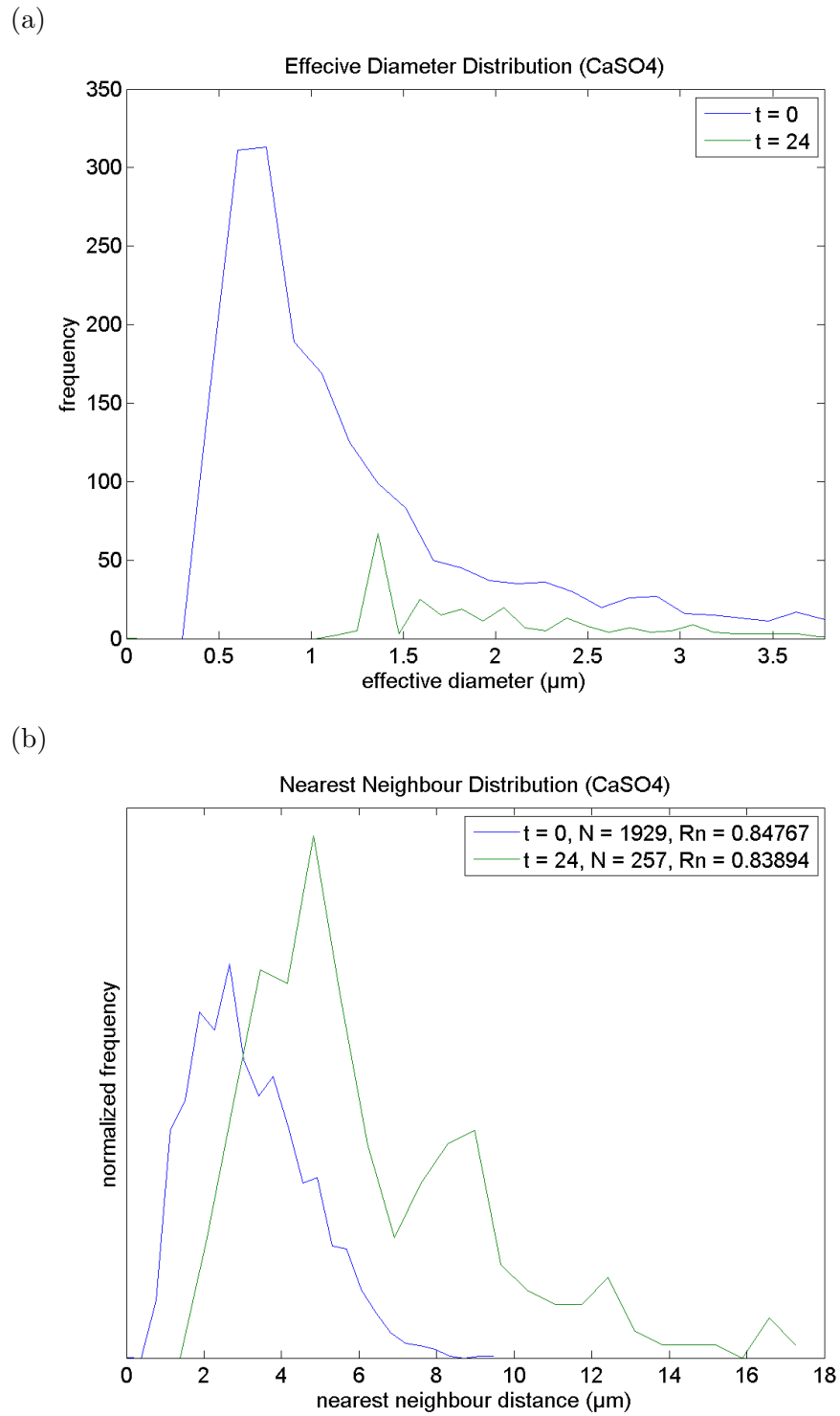


FIGURE 5.14. The effective diameter distribution (a) and NN distribution (b) of the CaSO₄ before (blue) and after (green) leaching.

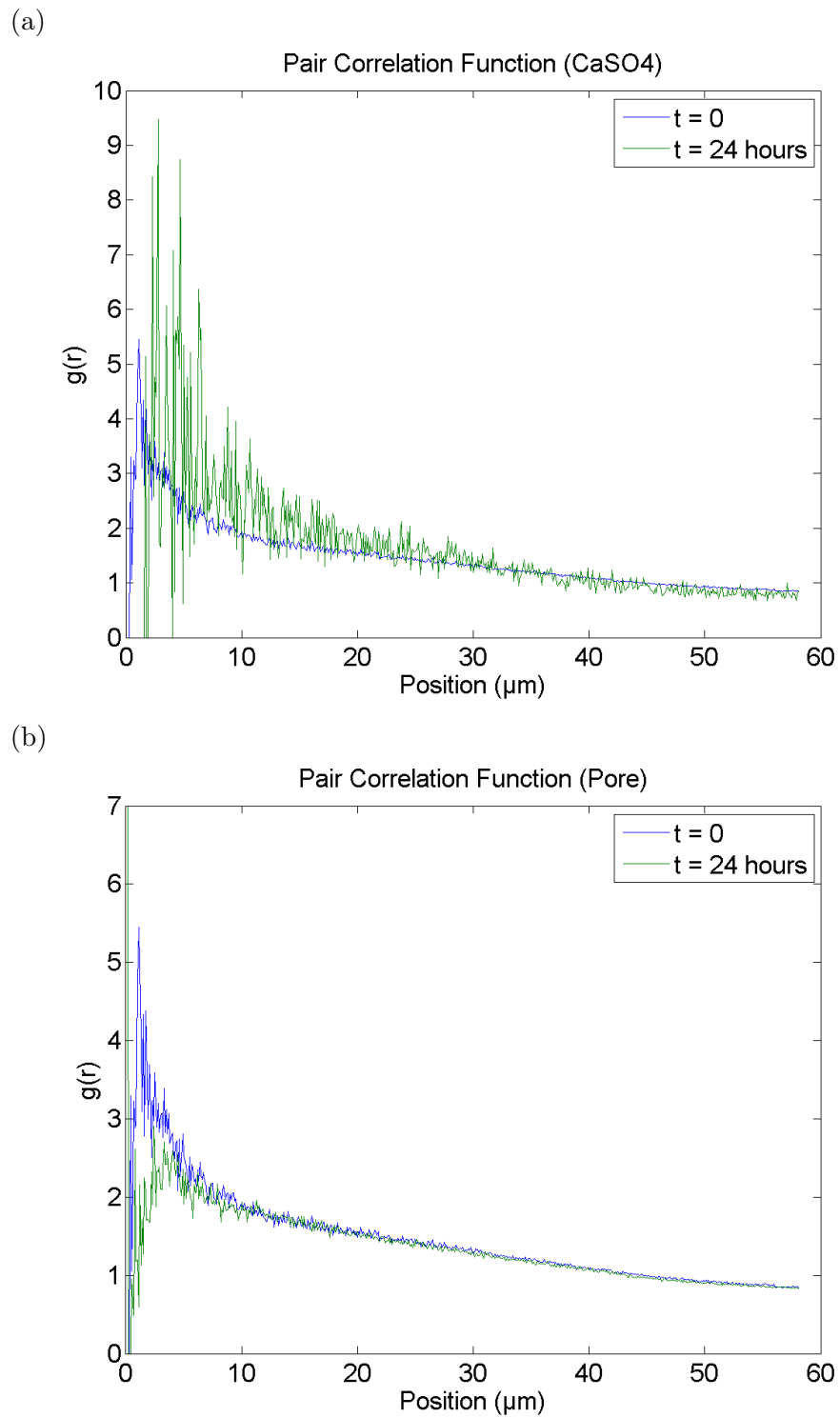


FIGURE 5.15. The PCFs for the CaSO₄ (a) and pores (b) before (blue) and after (green) leaching.

5.6 Conclusions

An ex-situ leaching experiment has been undertaken and imaged in 3D using sXRT on a aerospace primer with SrCrO_4 and CaSO_4 inhibitor particles. Additionally, multi-scale information is obtained in 3D by SBFSEM, which provides indications of the specific mechanisms involved during the leaching process. This is achieved by direct observation of the partially depleted inhibitor particles. These observations imply that the operation of a combination of mechanisms is involved in the leaching of inhibitor material from organic coatings. It is observed that porous networks remain following dissolution of an inhibitor particle, suggesting complete egress of inhibitor material from the clusters and the increasing availability of more material that can transport via these depleted clusters. Following 24 h of immersion, a depletion radius of approximately 25 μm from the defect site was observed. However, clusters still remain intact in close proximity to the defect site, thus providing redundancy in the event of further defects. Fractal dimensions of the clusters for both sXRT and SBFSEM data were found to be similar in value and range from 2.5 to 3, which may imply an increased leaching rate for this particular system. Quantification of the size and spatial distributions of the particle clusters are consistent with a transport behaviour through connected clusters of depleted inhibitor material as well as pre-existing porous networks.

Chapter 6

Quantitative Characterization of Porosity and Determination of Elastic Modulus for Sintered Micro-silver Joints

Preface

This chapter is based on a submitted manuscript entitled ‘*Quantitative Characterization of Porosity and Determination of Elastic Modulus for Sintered Micro-silver Joints*’.

The paper presents the first nano-scale 3D imaging of a lead free replacement joining technology for power electronics. This unique imaging technique allowed new insights into the connectivity and distribution of the porous networks within the joints in addition to establishing direct correlation of the processing-microstructure-properties relationship in this important new system. The authors demonstrate the changes in the porous structure with ageing and from this novel data develop an IBM that simulates the elastic performance of the joint on the sub-micron scale. These models have been validated by experimental results and agree with the overarching treatise on the elastic properties of porous solids.

The solders were synthesized and aged at École Nationale Supérieure de Mécanique et d’Aéro-technique (ENSMA), Poitiers, France and sent to Manchester for analysis. The experimental validation of the elasticity model was also performed independently at ENSMA.

6.1 Introduction

The requirement for reducing the use of harmful materials in convenience goods has prompted investigation into alternative solutions. Along with the need to drastically limit the emission of greenhouse gases, the increase of electric or hybrid vehicles in the market relies on their dependability with a specific focus on reliability of the embedded power electronics. The study of alternative materials to lead or lead-based alloys for die bonding is a critical step towards realising an environmentally-friendly solution. Sintered micro-silver joints are good candidates to replace lead-based alloys for die bonding of power electronics due to their excellent electrical properties and high melting temperature [179].

6.1.1 Background to Sintered Micro-Silver Joints

The synthesizing methodology, based on the sintering of silver paste, provides a material with significant porosity that is known to alter the mechanical properties when compared to the non-porous material. Although the mechanical properties of sintered micro-silver pastes can be found in the literature, little information is available on the relationship between mechanical properties and porosity. For example, Panin et al. demonstrated the reduction of hardness with increasing grain size by nano-indentation in addition to observing little change in the Young's modulus [180]. Bai et al. provided macroscopic measurements of density as well as electrical and thermal conductivities, which are found to be higher than alternative solder alloys [181]. Chen et al. used a dynamic mechanical analyzer to determine changes in elastic modulus and tensile strength as a function of temperature [182]. Furthermore, no work has been done on the impact of ageing the material Caccuri [3]. With respect to the elastic behaviour, Panin et al. [180] concluded that an increase in grain size due to annealing had no effect on the elastic properties as determined by nano-indentation.

Lifetime prediction of the entire system requires characterizing the evolution of the porous structure during thermal ageing in order to understand the modification of mechanical properties dominated by the porous structure of the joint material.

6.1.2 Elastic behaviour of porous solids

Several analytical models are proposed that link porosity with the elastic moduli of porous materials [183]. Mackenzie [184] states that the Young's modulus, E , as a function of the pore fraction, P , is of the form:

$$E = E_0(1 - aP + bP^2) \quad (6.1)$$

where E_0 is the Young's modulus of the solid material and a & b depend on the shape of the pores, although the exact form of this dependence is unknown [183]. The work of Ashby et al. [185] on foams takes into account how E scales with P as shown below:

$$E = cE_0(1 - P)^n \tag{6.2}$$

where $0.1 \leq c \leq 4$ and $n \approx 2$.

Ramakrishnan and Arunachalam [186] provide a model consistent with equation 6.2, but further demonstrate that it is possible to predict the Young's modulus of a porous solid as a function of pore fraction knowing only the Young's modulus and Poisson ratio of the solid material, i.e. E_0 and ν_0 respectively, by

$$c = \frac{1}{1 + (2 - 3\nu_0)P} \tag{6.3}$$

where ν_0 is the Poisson ratio of the solid material. Ramakrishnan and Arunachalam [186] verified this analytical model using a 2D idealized finite element (FE) models.

Following advancements in computing power, synthetic 3D FE meshes based on statistical models of porous solids were simulated. Roberts and Garboczi [187] used such an approach to model elasticity of porous ceramics and show their results to be consistent with the analytical model proposed by Bert [188]. Advancements in 3D imaging have allowed the replacement of such synthetic meshes with real image-based meshes, which fully describe the complicated geometry of porous solids. Knackstedt et al. [189] and Hardin and Beckermann [190] used image-based 3D FE models of foams obtained by XRT and used the analytical model proposed by Bert [188] to fit their results.

6.1.3 Aims

This investigation represents a first step toward addressing the lack of information concerning the porosity-elasticity relationship in this new joining technology by using complementary 2D and 3D imaging techniques in order to quantitatively analyse the porous structure on ‘as-sintered’ and aged materials. In addition, Finite Element (FE) meshes have been produced from the tomographic datasets as a means to predict the Young’s modulus of the sintered joint. This approach has been compared with experimental data obtained by a Dynamical Resonance Method (DRM).

6.2 Materials and Methods

6.2.1 Specimen Production

Heraeus LTS 043 04P2[®] Ag paste was sintered using an alternative processing route to the one recommended by the producer (recommended route: 150°C for 3 min then 240°C for 10 min under 10 MPa), allowing generation of the bulk specimen with the same microstructure as a real sintered joint [3]. The paste is composed of micro silver powder containing silver particles of 4 µm average size and mixed with various solvents. These solvents are necessary in order to facilitate the sintering process by avoiding agglomeration and aggregation of the particles. The elaboration process (illustrated in figure 6.1) includes a final sintering step at 240°C for 3 min under 10 MPa. Using this elaboration route, sintered bulk specimens with dimensions close to 30 mm × 5 mm × 0.5 mm were obtained.

Ageing was performed at 125°C for 1500 h in air. The density of the specimens prior to and after ageing were obtained from the weight to volume ratio using a high precision Sartorius MZ1 balance (accuracy better than 10 mg) and a micrometer (accuracy better than 1 µm).

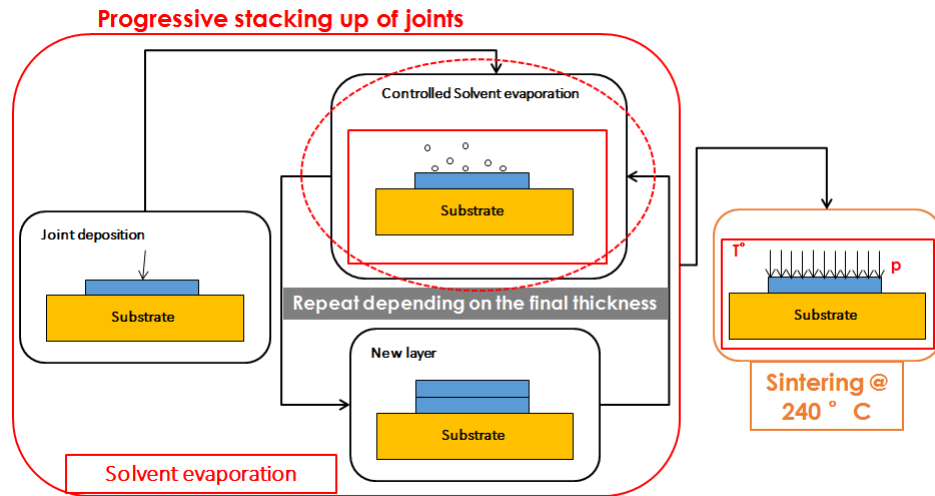


FIGURE 6.1. The methodology for producing the sintered joint material [3].

The specimen's 2D microstructure was observed by SEM, using a JEOL 6400 instrument operating at 25 kV after suitable surface preparation to reveal the porosity. Image analysis was performed using a specific in-house routine developed for MATLAB[®].

6.2.2 Experimental Determination of Young's Modulus

The Young's modulus has been obtained using a dynamical resonant method (DRM). It is based on the bending vibration of a beam under continuous frequency excitation [191]. The sample is maintained horizontally between steel wires located at the vibration nodes. Excitation and detection are performed using an electrostatic device (capacitance created between the sample and a unique electrode). This set-up allows experiments to be performed at 1 K min^{-1} under high vacuum (10^{-4} Pa) from 150 K up to 1400 K, without harmful contact.

The Young's modulus, E , can be directly determined by the relation (longitudinal modulus):

$$E = 0.9464\rho F_F^2 \frac{L^4}{h^2} T \quad (6.4)$$

where F_F is the flexural resonance frequency, ρ is the density, h is the beam thickness (0.5 to 2 mm), L is the span length (20 to 30 mm) and T is a correction factor close to 1.

6.2.3 SBFSEM

Sectioning is performed with an ultramicrotome to generate slices of 75 nm thickness, and an accelerating voltage of 2 keV in high vacuum mode is used to obtain BSE images of the block-face in the SEM. Monte Carlo simulations of the electron interaction volume in pure silver at 2 keV give depth penetrations not exceeding 35 nm as shown in figure 6.2, thus eliminating the possibility of oversampling the sections during image acquisition [192]. Magnification settings on the SEM give a pixel size of 37.5 nm.

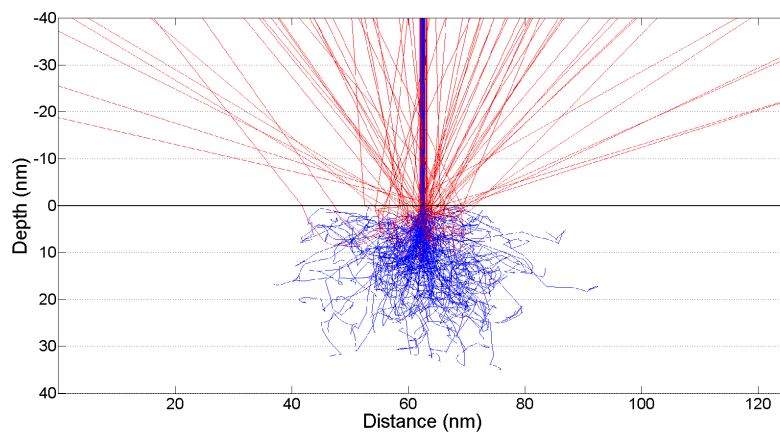


FIGURE 6.2. Monte Carlo simulation of the interaction volume in pure silver.

6.2.4 Image Processing and Quantification Methodology

The image stacks are imported into an open source software package for image processing. Local deformation of the observed porosity and matrix due to sectioning was not appreciable at the current length scale [193]. Therefore, the stack series is initially aligned using a rigid translation stack registration algorithm designed to compensate for sample drift during serial sectioning [194]. The image volume is interpolated onto a regular grid to produce cubic voxels for ease of processing. Owing to the high degree of contrast between the matrix and the porosity, the resulting volume is segmented using an automatic, histogram based, global thresholding algorithm [76]. A CCL algorithm is then applied using a 6 voxel neighbourhood to quantify the pore clusters, and isolate individual pores [195].

Depth profiles are achieved by consideration of the pore area fraction as a function of a selected orthogonal direction within the image volume (in this case, depth) and, thus, the entire porosity within the volume is considered for evaluation. The quantification of size and spatial distributions considers N pores (shown in blue in Figure 6.3) unconnected to the large singular porous network (shown in red in Figure 6.3) observed in all sample volumes.

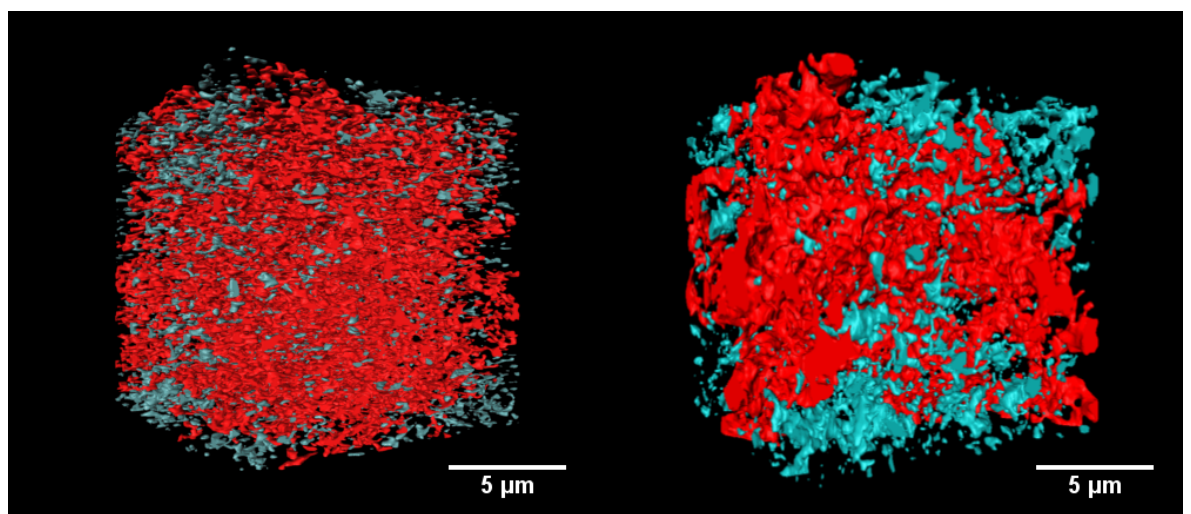


FIGURE 6.3. The reconstructed porosity for the as-sintered (left) and aged (right) solders. A single pore network shown in red is observed in both samples. Pore clusters shown in blue are quantified in isolation to observe size and spatial distributions of the unconnected porosity and its subsequent impact on performance.

Quantification of the i^{th} connected pores, i.e. pore volumes, effective diameters, NN distances and clustering factors are calculated as detailed in Chapter 3.

6.2.5 Finite Element Image Based Modelling

Segmented sub-volumes of the tomographic datasets acquired from the SBFSEM data were used to produce IBMs of the specimens. FE meshes were produced by forming STL surfaces at the free surface interfaces in Avizo (FEI) and meshing using snappyHexMesh as detailed in section 3.10.1. An example mesh is shown in figure 6.4 revealing the refinement implemented to capture the complex geometries of the interface. Boundary conditions are applied to the mesh via the case directory structure to simulate a linear-elastic, small strain compression test. A traction of 10 Pa is applied normally to the face of the mesh and the adjacent face is kept at a fixed displacement. Known physical parameters for pure silver, reproduced in table 6.1, are inserted into the simulation's mechanical properties dictionary. The 'solid-DisplacementFoam' solver was used to run simulations and convergence criteria were set to 10^{-10} . Values for Young's modulus are obtained from the stress-strain relationship after convergence, by measuring the mean displacement of the surface with the applied traction. The simulations were performed on meshes with a range of densities in order to reveal the relationship to Young's modulus.

TABLE 6.1. Known physical parameters of pure silver.

Parameter	Value
Density	10,490 g cm ⁻³
Poisson ratio	0.37
Young's modulus	83 GPa

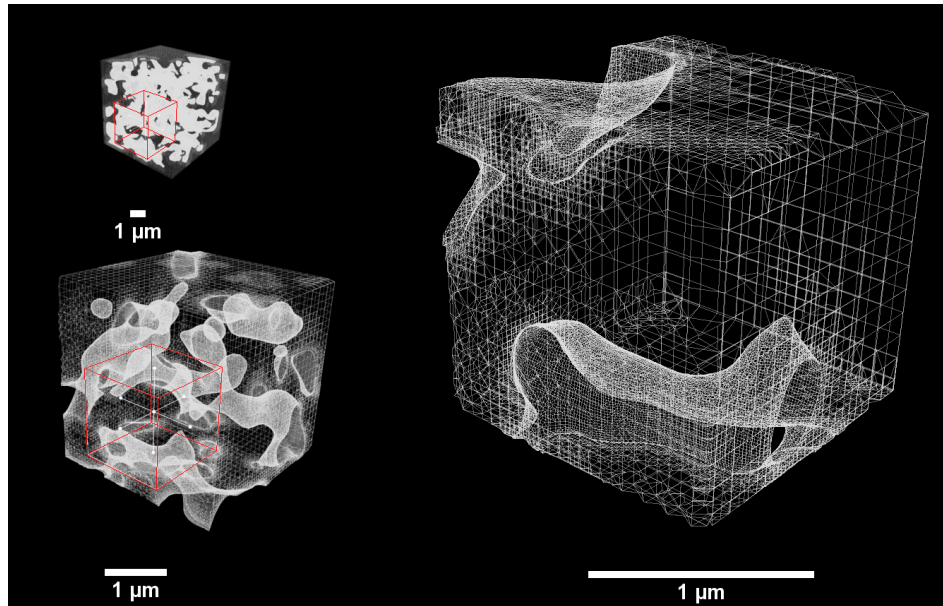


FIGURE 6.4. Wire-frame mesh of the pore-silver interface used for the FEA.

6.3 Results and Discussion

6.3.1 Quantification

Figure 6.5 shows a 2D comparison of the pore distribution of the same sample immediately after sintering (Figure 6.5a) and after ageing for 1500 h at 125°C (Figure 6.5b). A clear evolution of the microstructure is observed; the pores after sintering are homogeneously distributed while, after ageing, the pores are relatively heterogeneous and the pore size has increased substantially. Consequently, some areas of the aged material are almost free of pores, while some other areas display large pores. After direct measurement (weight/volume) or after using the pore surface fraction to density ratio established previously [3], the density of the material, measured before and after ageing at 125°C, remains identical, i.e. close to 8 g cm^{-3} in this case. While measurements in two dimensions (2D) give an insight of the pore microstructure evolution upon ageing, a three dimensional (3D) study is valuable in giving the actual spatial distribution, pore shape and size as well as the pore connectivity, and, critically, the evolution of connectivity [196]. Since 3D experiments using the 3View are destructive, two different specimens, with densities as close as possible to the as-sintered

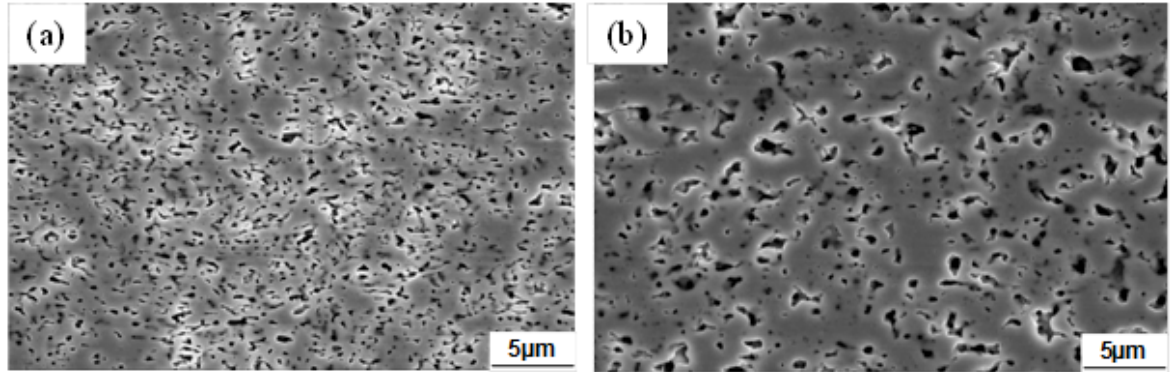


FIGURE 6.5. Scanning electron micrographs of the polished surface, highlighting the evolution of the porosity from the as-sintered specimen (a) to the aged specimen (b).

state, $7.8 \pm 0.2 \text{ g cm}^{-3}$ and $8.0 \pm 0.2 \text{ g cm}^{-3}$ respectively, were used to investigate the 3D evolution of the pore distribution. Reconstructed volumes are displayed in Figure 6.3, where the silver matrix has been made transparent and only the porosity is visible. Initial quantification of the depth profile of the pore density, as revealed in Figure 6.6a, shows a root mean squared (RMS) deviation of 1% implying a high level of homogeneity in the density as a function of depth for the as-sintered solder. In comparison, the aged solder is found to have an increase in RMS deviation by a factor of 2.4. Additionally, Fourier transforms of the depth profiles (figure 6.7) reveal a dominance in the lower spatial frequency domain. As observed qualitatively for the 2D analysis in Figure 6.5b, the quantification of the pore spatial distribution in 3D is less homogeneous after ageing than in the as-sintered state.

Both the size distributions (Figure 6.6b) of the image volumes and the spatial distribution (Figure 6.6c) of the pore clusters show a positive shift and an increase in frequency of the mid-sized pores leading to a higher mean value. Clustering ratios also reveal a move from an approximately random distribution (0.9629) of pore clusters to a more clustered distribution (0.8773).

A reduction in the number of pore clusters, in addition to both the spatial and size distributions of the pore clusters, is indicative of an agglomeration of pores that provides larger clusters with more distant NNs.

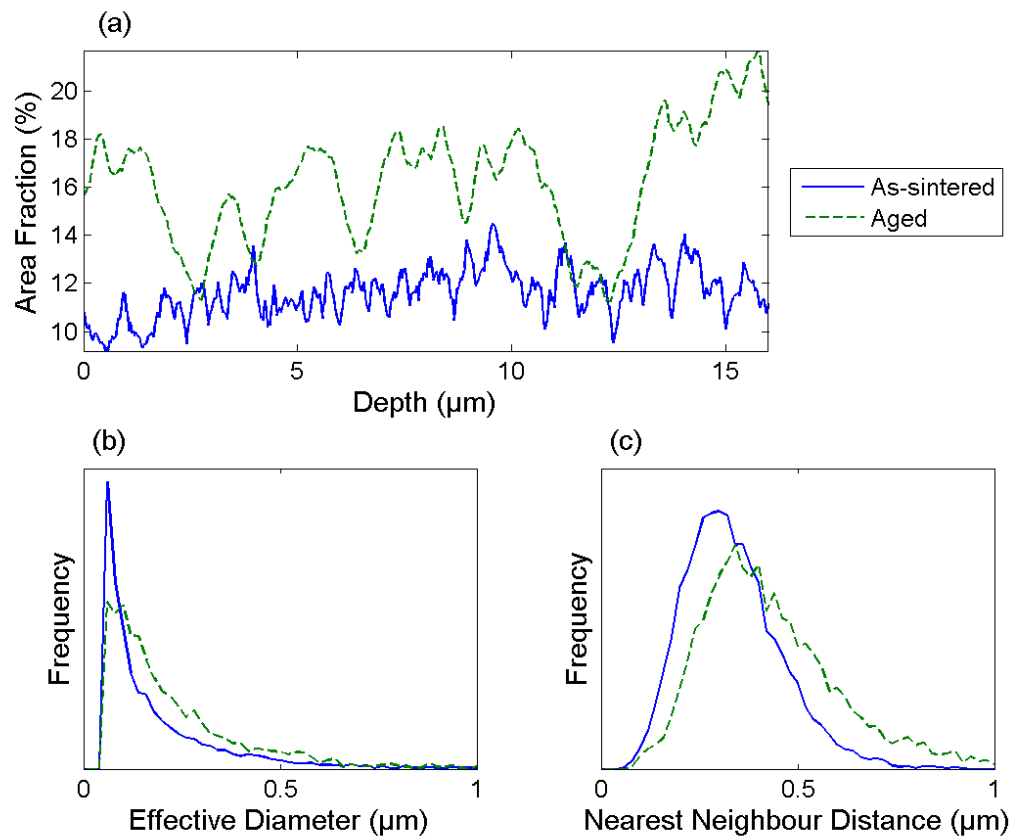


FIGURE 6.6. (a) The pore area fraction as a function of depth from the segmented volume; (b) the effective diameter distribution. The mean effective diameter is 95 nm for the as-sintered sample and 140 nm for the aged sample. Frequency is normalized with pore number density; (c) the NN distributions. For the as-sintered and aged samples respectively, the mean NN distances are 289 nm and 366 nm, and the clustering ratios are 0.9629 and 0.8773. The frequency is normalized with pore number density.

In other words, ageing tends to favour the disappearance of the smaller pores by either agglomeration or growth, leading to an increase of the average pore size, a shift of the distribution towards larger sizes and a larger distance between the NNs. This minimises both the amount of interfacial surface area between the phases, and also the curvature of this interface.

A further interesting feature stands in the evolution of the sphericity as illustrated in figure 6.8. While it has been estimated close to 0.7 just after sintering, it evolves towards 1 after ageing. All these factors tend to account for the surface energy reduction to be the main driving force for pore evolution during ageing. This may be helped by vacancy diffusion along the material grain boundaries.

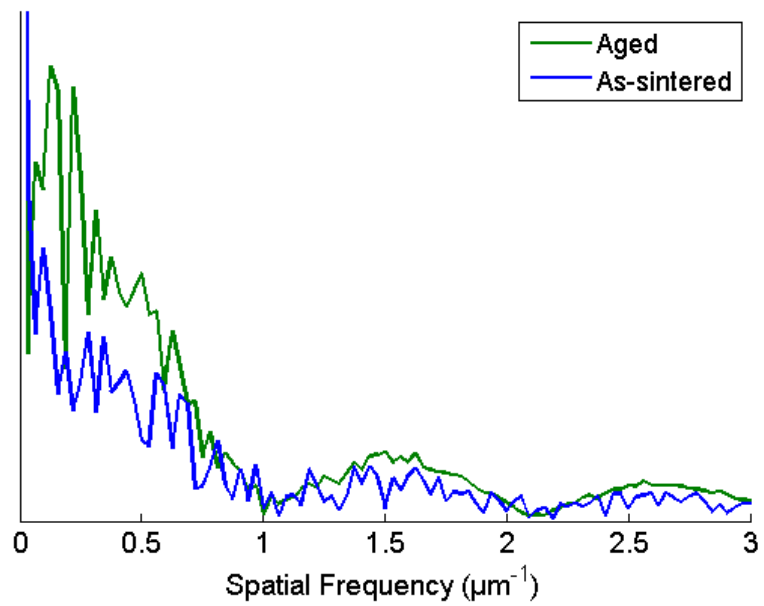


FIGURE 6.7. FFT of the area fraction data (figure 6.6a) revealing a dominance of the low spatial frequency of the pores in the aged specimen.

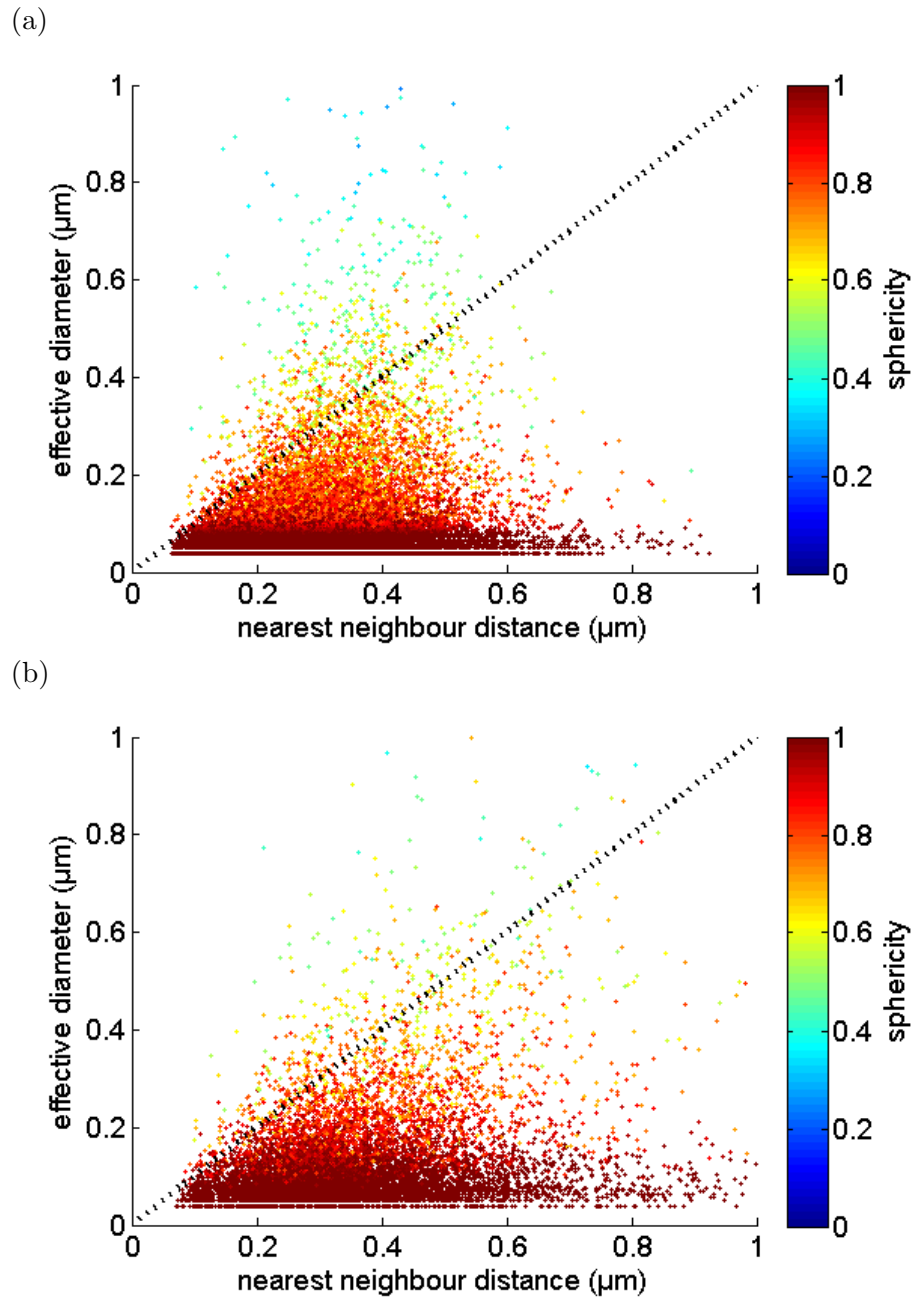


FIGURE 6.8. Effective diameters plotted against NN distances for each connected pore for the (a) as-sintered and (b) aged specimens. Plots are colour coded by sphericity.

6.3.2 Influence on the Elastic Properties

The dramatic evolution of the porosity during ageing may substantially alter the mechanical properties of sintered micro-silver joints since certain regions exhibit a high level of porosity while others are almost pore free. Upon ageing, the material structure tends to become heterogeneous and the local load bearing surface may vary substantially. The effect of the pore distribution on the mechanical properties of sintered micro-silver joints during ageing is one of the key parameters for modelling the mechanical behaviour of the entire electronic system in operating conditions.

The Young's modulus as a function of the pore density has been modelled using the reconstructed 3D images. Validation of the model has been achieved by comparison with experimentally determined data.

Solutions for the displacement fields in the produced FE meshes converged for a total of 7 cases. Example cases are shown for both the as-sintered and aged specimens in Figure 6.9. Qualitatively, it is plain to see a larger displacement field associated with the aged specimen across the face, indicating a reduced elastic performance. It is also apparent that the maximum displacements occur around porous regions, thus indicating that the elastic mechanical performance is a function of the distribution of the porosity. The increased heterogeneity, which impacts on elasticity will also play a part in determining induced failure at regions with the greatest agglomeration of porosity.

Comparing the values for Young's modulus with the quantified pore fraction (i.e. specimen density) agrees strongly with the proposed empirical model by Ramakrishnan and Arunachalam [186]. This model has been validated using DRM experimental measurements on as-sintered materials obtained with various sintering loads, i.e. as-sintered specimens with a large spectrum of densities and bulk silver (density 10.4 g cm^{-3}). As seen in Figure 6.10,

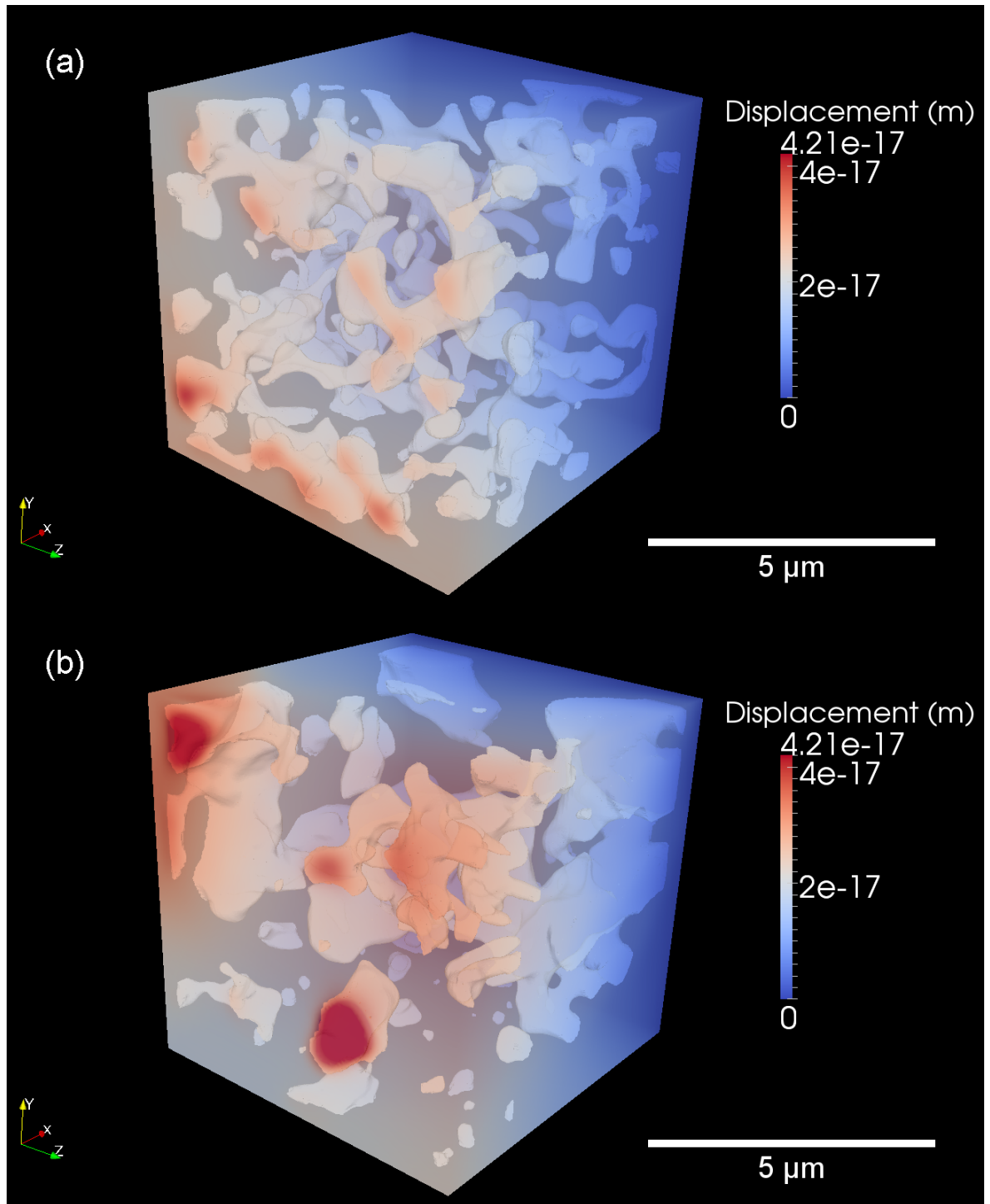


FIGURE 6.9. Images showing the solution of the displacement field within sub volumes of the as-sintered (a) and aged (b) specimens. Pressure is applied along the positive x direction.

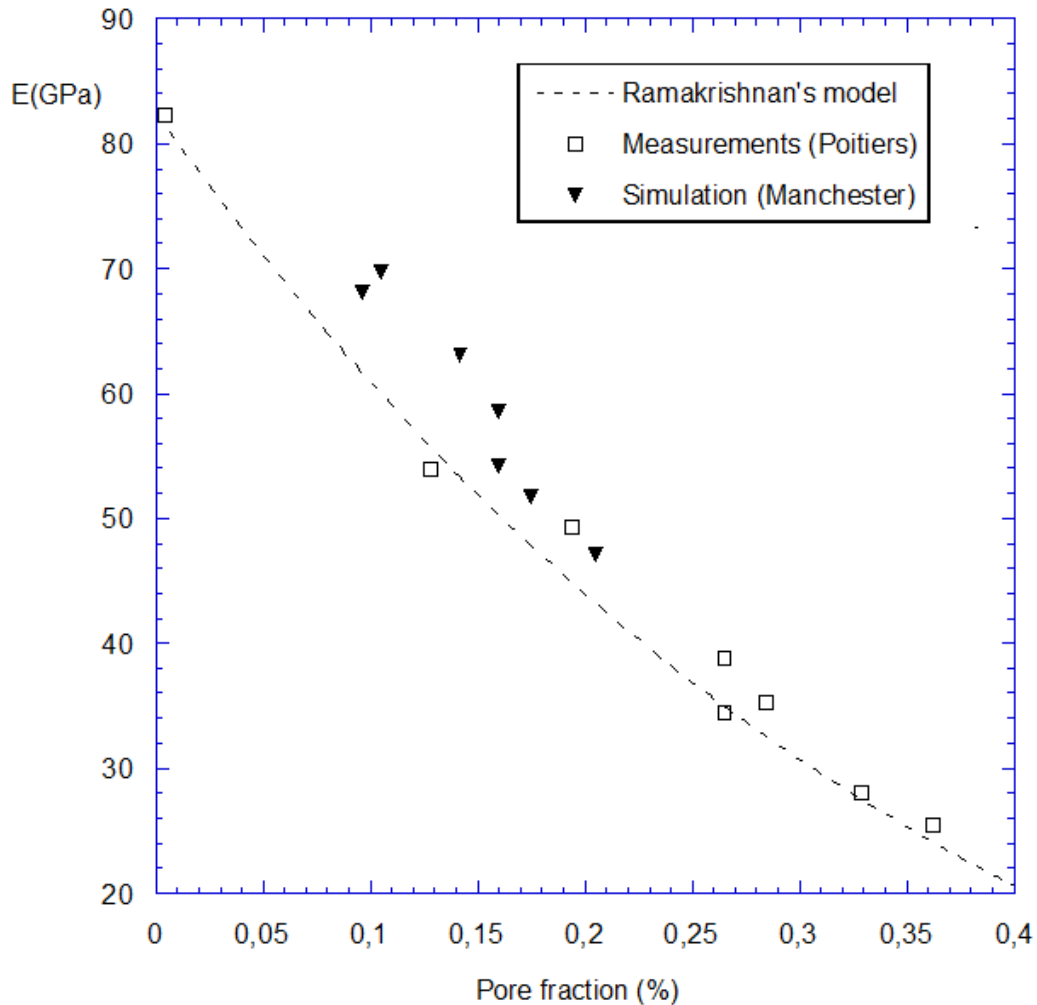


FIGURE 6.10. A combination of results for both the FE modelling and direct elasticity measurements plotting Young's modulus against pore fraction. The fit shows an agreement of the data with the proposed empirical model.

the Young's modulus predicted by the model is not a function of the pore distribution and geometry. The Young's modulus is, to a good approximation, only a function of the material density and is not altered or modified by ageing globally. Locally, however, significant variation in the porous structure is observed in the aged samples. The reduced elasticity in regions of high porosity is, therefore, a likely candidate for sites of initial failure of the sintered joint. The size and curvature of the porosity are also important for the fatigue properties of the material [197]. It is anticipated that these regions also significantly impact on the plastic behaviour of the material. Work is currently ongoing to evaluate a failure model,

which incorporates both the plastic and elastic behaviour during ageing.

6.4 Conclusions

For the first time, sintered micro-silver pastes have been successfully imaged in high resolution 3D to observe the evolution of the porous networks during ageing. Quantification of the size and distribution of the porous networks is consistent with Ostwald ripening. The model proposed by Ramakrishnan and Arunachalam [186] is validated for silver foams of porosity $\leq 20\%$, implying that the elastic properties are only a function of density. The porosity becomes increasingly heterogeneous after ageing, the local variation of pore fraction corresponds to a local variation of the elastic behaviour. Global density variations were not appreciable during ageing, implying a constant value for elasticity over time. This is consistent with Panin et al.'s conclusions that the global elastic behaviour is unaffected by annealing.

Chapter 7

Conclusions and Suggestions for Further Work

It is clear that SBFSEM is a versatile and powerful method for obtaining large ROI, high resolution datasets. A number of research ideas associated with 3D imaging have been explored in the previous chapters to reveal quantifiable 3D microstructural features and geometries.

With respect to understanding the spatial distribution of pigmented domestic coatings, a primary disadvantage was quickly identified. It was found that hard, dispersed phases in relatively soft matrices can be shifted and plucked out during slicing. Identifying these situations in the data is straightforward but, depending on the use of the data, accounting for these effects can have mixed results. In the case of understanding the spatial distribution of the particles, the results obtained in the 3View were found to agree strongly with those obtained using FIBSEM data where it can be easily shown to not suffer from these kinds of image defects due to slicing. However, other information such as size and shape distributions are not reliable due to these defects. Further work in this area should involve the acquisition of more data with varying amounts of filler which could be used to refine the proposed analytical model.

In Chapter 5, SBFSEM was utilized to obtain multi-scale information. Specifically, the fractal dimensions of the particle clusters have a similar distribution for both length scales indicating that these clusters are true fractals and, therefore, their transport behaviour could be described through this kind of characterization. Difficulties arose in identifying the same ROI for correlative microscopy due to the different sample preparation techniques associated with XRT and SBFSEM. Identifying a ROI in the XRT facility such that samples can then be transferred to the SBFSEM facility and rescanned in close proximity to that region is highly desirable. This would allow the acquisition of multi-scale information of the same ROI. Direct comparison of the same particle clusters could then be made to shed further light on the fractal nature of the inhibitor clusters. Further effort could also be directed in reducing the radiation damage and subsequent deformation during sXRT. Such improvements

could allow acquisition of polychromatic sXRT datasets, which could provide more refined information on elemental distribution of phases in the coatings instead of using advanced filtering and semi-automatic segmentation methods to identify the phases.

A very straightforward approach to modelling the elastic behaviour of porous solids has been demonstrated in Chapter 6. Good agreement with experimental data, and a well established analytical model for porous solids, demonstrate the power of this approach. Further work in this area should be directed towards in-situ loading and ageing tests in a high resolution sXRT. Such information could be used to directly validate the deformation model and reveal departure from elastic behaviour.

Finally, other applications have been explored briefly, an example of which can be found in Appendix B. The imaging of shale rock to model the transport of gas through fractured porous organic material is undertaken. The complexity associated with this multi-scale and multi-physics problem is approached from consideration of unfractured samples undergoing Fickian diffusion as a first step. Further work should involve the coupling of Stokes flow in the porous regions of the material and developing a multi-scale IBM utilizing both SBFSEM and XRT data.

Appendix A

Nearest Neighbour Code

This appendix is intended to describe in full the code presented in section 3.9.3.2 reproduced below for convenience. It is assumed that the reader has basic knowledge of MATLAB [100] formalism such as array notation and basic functions. The author recommends ‘Essential MATLAB for Engineers and Scientists’ [198] as an introduction to the MATLAB programming language and interface.

```

1 % calculate number of coordinates
2 N = size(x,1);
3
4 % preallocate nearest neighbour distances
5 nn.distance = zeros(N,1);
6
7 % each loop calculates the ith element of nn.distance
8 for i=1:N
9
10         % a Nx3 matrix containing all the displacements between ...
11         % the ith particle and all other particles
12         displacement_vectors = cat(2, x(:,1)-x(i,1), x(:,2)-x(i,2), ...
13         x(:,3)-x(i,3));
14
15         % a Nx1 vector containing all the distances achieved by ...
16         % applying pythagoras to displacement_vectors
17         distances = sqrt(sum(displacement_vectors.^2,2));
18
19         % sort the distances such that sorted_distances = ...
20         % [0, NN, 2nd NN, 3rd NN, ...]
21         sorted_distances = sort(distances);
22
23         % populate the nearest neighbour distance
24         % neighbour = 1 for nearest neighbour, 2 for 2nd nearest ...
25         % neighbour etc.
26         nn_distance(i) = sorted_distances(1+neighbour);
27
28 end

```

PROGRAM 2. MATLAB code designed to calculate NN distance.

This code requires two variables as inputs. The first variable is x which is an N by 3 matrix, where the i^{th} row contains 3 columns containing the x , y and z coordinates of the barycentres respectively. The second variable `neighbour` is a scalar, which is defined by the user and describes which neighbour to select. Typically `neighbour = 1` which is when the NN is required but any positive integer which is less than the number of coordinates can be entered to find the n^{th} NN.

The output of the code is a vector called `nn_distance`, which corresponds to the n^{th} NN of the coordinates described by the variable `x`. For example, the value of `nn_distance(4)` will be the distance of the NN from the 4th coordinate, i.e. `x(4,:)`.

Firstly, because a loop is used to populate the `nn_distance` variable, it is good practice to ‘preallocate’ the variable so that the amount of RAM required to run the code does not increase with each iteration of the loop. It is then necessary to run a single loop for each coordinate or, equivalently, each row of `x`.

The notation in table A.1 is used to describe a single loop of the code where we have the loop variable `i = a`.

TABLE A.1. Variables and their definitions used in the NN code.

Code Variable	Mathematical Variable	Description
<code>N</code>	N	Number of coordinates
<code>x</code>	\vec{R}_i	An array of 3-vectors describing the i^{th} coordinate
<code>x(:,1)</code>	x_i	The x-component of the i^{th} coordinate
<code>x(:,2)</code>	y_i	The y-component of the i^{th} coordinate
<code>x(:,3)</code>	z_i	The z-component of the i^{th} coordinate
<code>nn_distance</code>	D_i	The NN distance of the i^{th} coordinate
<code>displacement_vectors</code>	\vec{v}_i	A vector describing the NN displacement of the i^{th} coordinate
<code>neighbour</code>	n	The n^{th} neighbour required for the computation

We begin with the position of the a^{th} coordinate

$$\vec{R}_a = (x_a, y_a, z_a)$$

Subsequently, we compute the vectors pointing from the a^{th} coordinate to all the other coordinates in \vec{x}_i (as illustrated in figure A.1:

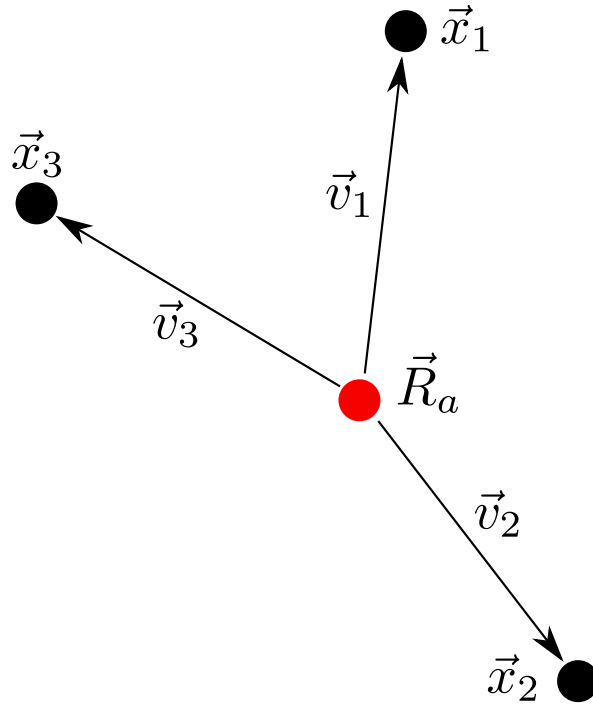


FIGURE A.1. A small system of particles illustrating the calculated vectors in 2D.

$$\vec{v}_a = \begin{pmatrix} \vec{R}_1 - \vec{R}_a \\ \vec{R}_2 - \vec{R}_a \\ \vec{R}_3 - \vec{R}_a \\ \vdots \\ \vec{R}_N - \vec{R}_a \end{pmatrix} = \left[\begin{pmatrix} x_1 - x_a \\ x_2 - x_a \\ x_3 - x_a \\ \vdots \\ x_N - x_a \end{pmatrix}, \begin{pmatrix} y_1 - y_a \\ y_2 - y_a \\ y_3 - y_a \\ \vdots \\ y_N - y_a \end{pmatrix}, \begin{pmatrix} z_1 - z_a \\ z_2 - z_a \\ z_3 - z_a \\ \vdots \\ z_N - z_a \end{pmatrix} \right] \quad (\text{A.1})$$

Although this is a rather verbose way of representing the calculation, MATLAB is particularly fast at performing vectorized subtractions as shown in the right hand side of equation A.1. It is also possible to compute this problem using a nested loop within the loop produced above, but the amount of computing time required using this method increases exponentially with N .

The distances between the a^{th} coordinate and all the other coordinates in \vec{R}_i are computed by taking $|\vec{v}_a|$.

Finally, $|\vec{v}_a|$ is sorted in ascending numerical order and the $(n + 1)^{\text{th}}$ term is the NN distance for the a^{th} coordinate*. The loop is thus repeated for all coordinates so that the variable `nn_distance` (D_i) is fully populated.

*The first term is always zero because it is the distance between the a^{th} coordinate and itself

Appendix B

Transport Modelling in Shale

B.1 Background

Recent developments in the process of hydraulic fracturing of unconventional gas reservoirs has led to a rapid increase in shale gas production. This rise is anticipated to continue over the first half of the century as conventional domestic supplies dwindle and countries avoid reliance on imported fuel. Shale gas is dispersed throughout the mud rock within micro and nano porosities; it is surrounded by organic material which is very low in permeability, thereby presenting a significant challenge for its retrieval. Shale is a highly heterogeneous material, with large variations in composition over length scales from the nanometre to the kilometre. The transport of shale gas within the organic component of the material is not well understood due to the high heterogeneity and low permeability of the material. It is hoped that modelling the flow of the gas will shed light on how to best optimise production procedures.

This appendix is intended to provide a feasibility study on the application of IBM to SBFSEM data to further understand the transport of gas through the organic material.

B.2 Motivation

Using the 3View to obtain SBFSEM is ideal for geological materials owing to its high ROI to resolution ratio. At 50 nm, a 40 μm ROI can be achieved allowing for a large dataset to be obtained relatively quickly and easily at high resolutions. In addition, the ESEM allows non-conductive materials to be scanned without the application of a conductive coating to avoid charging.

B.3 Methods

B.3.1 Experimental

The samples were first roughly cut to approximate dimensions of 1.5×0.5 cm and then embedded in epoxy resin. The sample was then ground to produce a tip which was ultramicrotomed (see 2.3.1) to produce a finer tip of approximately 50×300 μm .

B.3.2 Computational

The organic material is the only permeable phase within shale. This can be easily segmented by thresholding and meshing the resulting binary image as described in 3.10.1.

A diffusion solver has been created by altering a standard OpenFOAM solver to satisfy Fick's second law:

$$\frac{\partial \Phi(\vec{r}, t)}{\partial t} = \nabla \cdot (D \nabla \Phi(\vec{r}, t)) \quad (\text{B.1})$$

where $\Phi(\vec{r}, t)$ is the concentration of gas at position \vec{r} in the organic phase at time, t . D is the diffusivity of the organic phase which is assumed to be a scalar*.

Boundary conditions placed on the mesh should encourage the diffusion of gas through the organic phase. Therefore, a single face of the mesh is set to be saturated with gas, for example $\Phi((0, y, z), 0) = 1$.

*It is possible that the diffusivity of the organic material is not isotropic in which case, D would become a vector.

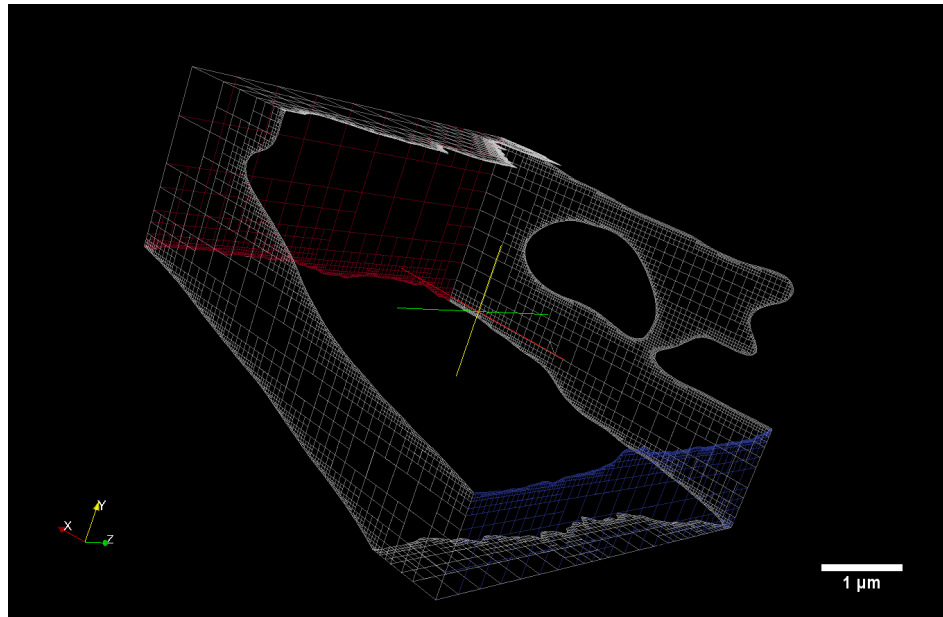


FIGURE B.1. The faces of an example mesh showing the applied boundary conditions.

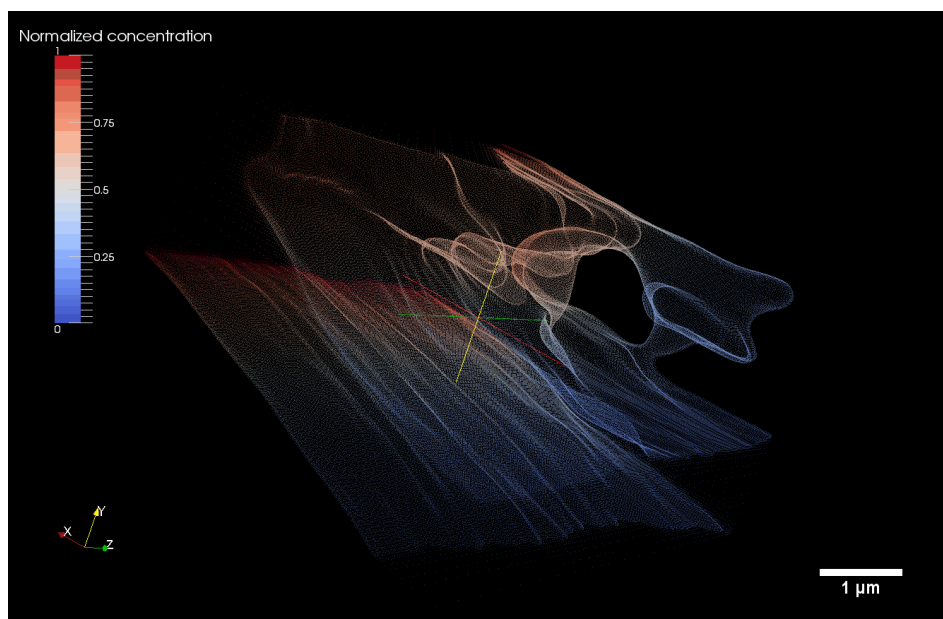


FIGURE B.2. A mesh undergoing diffusion and coloured by normalized concentration.

B.4 Results

Small meshes have been simulated for the feasibility study, but it is anticipated that much larger meshes can be simulated with relative ease. The application of boundary conditions is illustrated in figure B.1 and the resulting wireframe mesh undergoing simulated diffusion is shown in figure B.2.

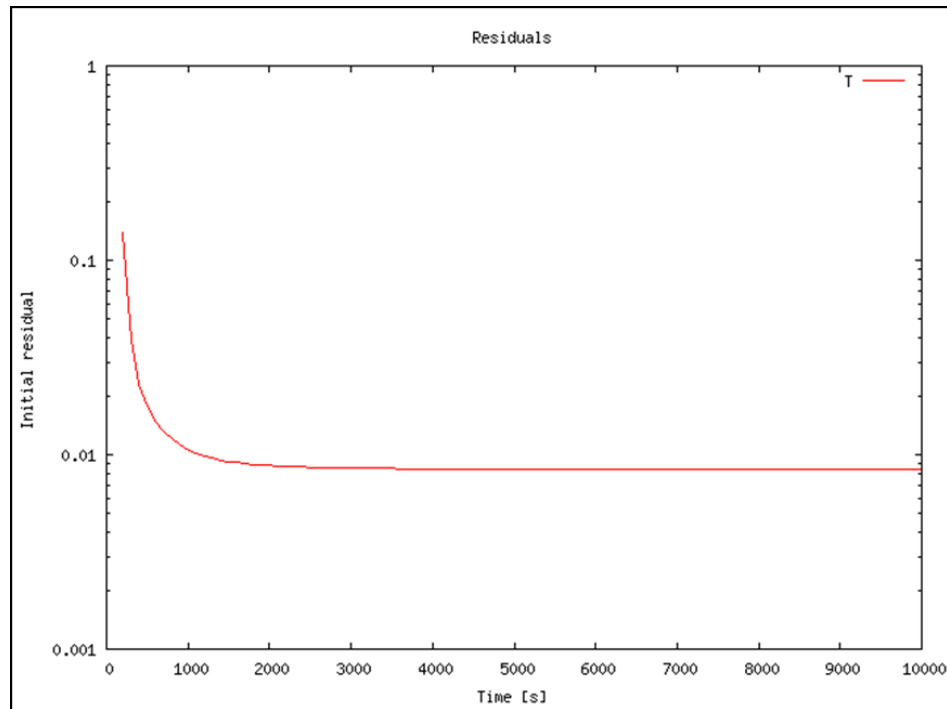


FIGURE B.3. The sum of the element residuals plotted as a function of time step.

Owing to the simple nature of the solver, the solution converges quickly as shown in figure B.3. Data for the global concentration of the mesh as a function of time are plotted in figure B.4, showing the anisotropy of the permeability owing to the different characteristic saturation times along each of the major axes. Data for the linear transport of gas along a particular axis for each time step are shown in figure B.5, where each plot corresponds to the concentration profile at a particular time step.

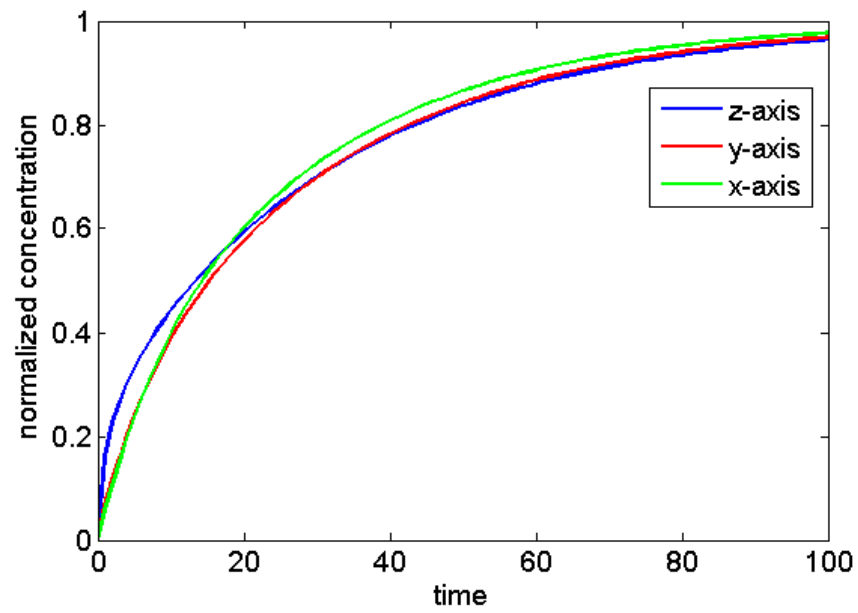


FIGURE B.4. A plot of the global mesh concentration as a function of time time.

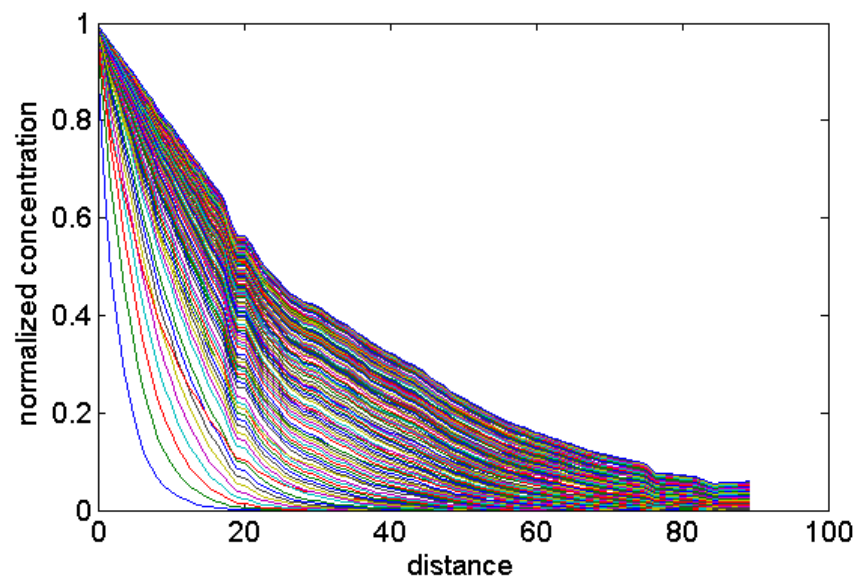


FIGURE B.5. A plot of the concentration along a single axis of the data. Each plot is a differing time step showing the evolution of the concentration field over time. Distance is not scaled.

B.5 Conclusions and Further Work

The combination of SBFSEM and IBM has been shown to provide reasonable results for the understanding of transport of gas within shale rock. Images obtained are representative of the geometry of the organic material and the solver is sufficiently simple to allow for a large increase in the number of elements for further work. The software can be run on large computer clusters at very low cost.

The effective permeability can be calculated from the application of Darcy's law to the resulting simulation [199]. These values can be directly compared with experimental means of evaluating the effective permeability.

Interfacial effects between pores and organic material have yet to be fully developed in the simulation. A two-phased mesh coupling both diffusive flow in the organic regions with Stokes flow in the porous regions is the next step in adequately simulating the transport through the media [200].

To meet the requirement for modelling the multi-scale transport behaviour, a large number of small scale simulations should be produced. These will provide statistics on the variation of effective permeability at higher length scales. Larger scale models could then be produced by the guided arrangement of these smaller simulations in line with data obtained at these length scales (i.e. XRT data) where a compensation can be made for the reduced resolving power.

Bibliography

- [1] J. I. Goldstein, D. E. Newbury, and P. Echlin. *Scanning Electron Microscopy and X-Ray Microanalysis*. Springer, 3rd edition, 2003.
- [2] D. Harrop. Chemical Inhibitors for Corrosion Control. In B. G. Clubleby, editor, *Chemical Inhibitors for Corrosion Control*, page 9. Royal Society of Chemistry, 1990.
- [3] Caccuri. *Ca*. PhD thesis, ENSMA, France, 2014.
- [4] S.A. Furman, F.H. Scholes, A.E. Hughes, and D. Lau. Chromate leaching from inhibited primers. *Progress in Organic Coatings*, 56(1):33–38, May 2006. ISSN 03009440. doi: 10.1016/j.porgcoat.2006.01.016. URL <http://www.sciencedirect.com/science/article/pii/S0300944006000270>.
- [5] A. Zankel, B. Kraus, P. Poelt, M. Schaffer, and E. Ingolic. Ultramicrotomy in the ESEM, a versatile method for materials and life sciences. *Journal of microscopy*, 233(1):140–8, January 2009. ISSN 1365-2818. doi: 10.1111/j.1365-2818.2008.03104.x. URL <http://www.ncbi.nlm.nih.gov/pubmed/19196420>.
- [6] P. J. Goodhew and F. J. Humphreys. *Electron Microscopy and Analysis*. Taylor & Francis, 1988. ISBN 0-85066-414-4.
- [7] T. E. Everhart and R. F. M. Thornley. Wide-band detector for micro-microampere low-energy electron currents. *Journal of Scientific Instruments*, 37(7):246–248, July 1960. ISSN 0950-7671. doi: 10.1088/0950-7671/37/7/307. URL <http://stacks.iop.org/0950-7671/37/i=7/a=307>.
- [8] P. F. Weller. An analogy for elementary band theory concepts in solids. *Journal of Chemical Education*, 44(7):391, July 1967. ISSN 0021-9584. doi: 10.1021/ed044p391. URL <http://dx.doi.org/10.1021/ed044p391>.
- [9] L. Meitner. Über die Entstehung der β -Strahl-Spektren radioaktiver Substanzen. *Zeitschrift für Physik*, 9(1):131–144, 1922. ISSN 0044-3328. doi: 10.1007/BF01326962. URL <http://dx.doi.org/10.1007/BF01326962>.
- [10] P. Auger. Sur les rayons β ; secondaires produits dans un gaz par des rayons X. *C.R.A.S.*, 177, 1923.

- [11] O. G. Wells. *Scanning Electron Microscopy*. McGraw-Hill Inc., 1974.
- [12] P. Echlin, C. E. Fiori, J. Goldstein, D. C. Joy, and D. E. Newbury. *Advanced Scanning Electron Microscopy and X-Ray Microanalysis*. Springer, 1986.
- [13] R. C. Furneaux, G. E. Thompson, and G. C. Wood. The application of ultramicrotomy to the electronoptical examination of surface films on aluminium. *Corrosion Science*, 18(10):853–881, January 1978. ISSN 0010938X. doi: 10.1016/0010-938X(78)90009-4. URL <http://www.sciencedirect.com/science/article/pii/0010938X78900094>.
- [14] K. Shimizu, K. Kobayashi, P. Skeldon, G. E. Thompson, and G. C. Wood. An atomic force microscopy study of the corrosion and filming behaviour of aluminium. *Corrosion Science*, 39(4):701–718, April 1997. ISSN 0010938X. doi: 10.1016/S0010-938X(97)89337-7. URL <http://www.sciencedirect.com/science/article/pii/S0010938X97893377>.
- [15] K. Shimizu, G. M. Brown, K. Kobayashi, P. Skeldon, G. E. Thompson, and G. C. Wood. Ultramicrotomy route towards the enhanced understanding of the corrosion and filming behaviour of aluminium and its alloys. *Corrosion Science*, 40(7):1049–1072, July 1998. ISSN 0010938X. doi: 10.1016/S0010-938X(98)00006-7. URL <http://www.sciencedirect.com/science/article/pii/S0010938X98000067>.
- [16] K. Shimizu, H. Fujitani, H. Habazaki, P. Skeldon, and G. E. Thompson. Examination of surface films on aluminium and its alloys by low-voltage scanning and scanning transmission electron microscopy. *Corrosion Science*, 46(10):2549–2561, October 2004. ISSN 0010938X. doi: 10.1016/j.corsci.2004.02.004. URL <http://www.sciencedirect.com/science/article/pii/S0010938X04000514>.
- [17] P. Bouguer. *Essai d'optique sur la gradation de la lumière*. s.n., 1729.
- [18] J. H. Lambert. *Photometria, sive De mensura et gradibus luminus, colorum et umbrae*. Leipzig: W. Engelmann, 1760.
- [19] J. C. Poggendorff. *Annalen der Physik*. J.A. Barth, 1852.
- [20] R. T. DeHoff. Quantitative serial sectioning analysis: preview. *Journal of Microscopy*, 131(3):259–263, September 1983. ISSN 00222720. doi: 10.1111/j.1365-2818.1983.tb04254.x. URL <http://doi.wiley.com/10.1111/j.1365-2818.1983.tb04254.x>.
- [21] M. A. Mangan, P. D. Lauren, and G. J. Shiflet. Three-dimensional reconstruction of Widmanstätten plates in Fe-12.3Mn-0.8C. *Journal of Microscopy*, 188(1):36–41, October 1997. ISSN 0022-2720. doi: 10.1046/j.1365-2818.1997.2380799.x. URL <http://doi.wiley.com/10.1046/j.1365-2818.1997.2380799.x>.

- [22] T. Wolfsdorf. The morphology of high volume fraction solid-liquid mixtures: An application of microstructural tomography. *Acta Materialia*, 45(6):2279–2295, June 1997. ISSN 13596454. doi: 10.1016/S1359-6454(96)00338-2. URL [http://dx.doi.org/10.1016/S1359-6454\(96\)00338-2](http://dx.doi.org/10.1016/S1359-6454(96)00338-2).
- [23] M. Li, S. Ghosh, O. Richmond, H. Weiland, and T. N. Rouns. Three dimensional characterization and modeling of particle reinforced metal matrix composites part II: damage characterization. *Materials Science and Engineering: A*, 266(1-2):221–240, June 1999. ISSN 09215093. doi: 10.1016/S0921-5093(98)01133-2. URL [http://dx.doi.org/10.1016/S0921-5093\(98\)01133-2](http://dx.doi.org/10.1016/S0921-5093(98)01133-2).
- [24] M. Li, S. Ghosh, O. Richmond, H. Weiland, and T.N. Rouns. Three dimensional characterization and modeling of particle reinforced metal matrix composites: part I. *Materials Science and Engineering: A*, 265(1-2):153–173, June 1999. ISSN 09215093. doi: 10.1016/S0921-5093(98)01132-0. URL [http://dx.doi.org/10.1016/S0921-5093\(98\)01132-0](http://dx.doi.org/10.1016/S0921-5093(98)01132-0).
- [25] J. Alkemper and P. W. Voorhees. Three-dimensional characterization of dendritic microstructures. *Acta Materialia*, 49(5):897–902, March 2001. ISSN 13596454. doi: 10.1016/S1359-6454(00)00355-4. URL [http://dx.doi.org/10.1016/S1359-6454\(00\)00355-4](http://dx.doi.org/10.1016/S1359-6454(00)00355-4).
- [26] J. Alkemper and P. W. Voorhees. Quantitative serial sectioning analysis. *Journal of Microscopy*, 201(3):388–394, March 2001. ISSN 0022-2720. doi: 10.1046/j.1365-2818.2001.00832.x. URL <http://doi.wiley.com/10.1046/j.1365-2818.2001.00832.x>.
- [27] M. V. Kral, M. A. Mangan, G. Spanos, and R. O. Rosenberg. Three-dimensional analysis of microstructures. *Materials Characterization*, 45(1):17–23, July 2000. ISSN 10445803. doi: 10.1016/S1044-5803(00)00046-2. URL [http://dx.doi.org/10.1016/S1044-5803\(00\)00046-2](http://dx.doi.org/10.1016/S1044-5803(00)00046-2).
- [28] N. Chawla, V. V. Ganesh, and B. Wunsch. Three-dimensional (3D) microstructure visualization and finite element modeling of the mechanical behavior of SiC particle reinforced aluminum composites. *Scripta Materialia*, 51:161–165, 2004. URL <http://www.scopus.com/inward/record.url?eid=2-s2.0-2342454411&partnerID=40&md5=734fcf42478918837c04f16d22b2c5f4>.
- [29] L. E. Ostroff, J. C. Fiala, B. Allwardt, and K. M. Harris. Polyribosomes redistribute from dendritic shafts into spines with enlarged synapses during LTP in developing rat hippocampal slices. *Neuron*, 35:535–545, 2002. URL <http://www.scopus.com/inward/record.url?eid=2-s2.0-0036685668&partnerID=40&md5=aa057e7f8446bd77502f35308a274cd2>.

- [30] J. E. Spowart, H. M. Mullens, and B. T. Puchala. Collecting and analyzing microstructures in three dimensions: A fully automated approach. *JOM*, 55:35, 2003. ISSN 1047-4838, 1047-4838.
- [31] J. E. Spowart. Serial Sectioning in the Micron-plus Range and Modern Techniques for Automation. *Microscopy and Microanalysis*, 12(S02):90–91, August 2006. ISSN 1435-8115. URL http://journals.cambridge.org/abstract_S1431927606069637.
- [32] L. Babout, E. Maire, J. Y. Buffière, and R. Fougères. Characterization by X-ray computed tomography of decohesion, porosity growth and coalescence in model metal matrix composites. *Acta Materialia*, 49:2055–2063, 2001. URL <http://www.scopus.com/inward/record.url?eid=2-s2.0-0035933664&partnerID=40&md5=c2ee8f46eda61c609d02e745be5e6bd8>.
- [33] R. K. Everett, K. E. Simmonds, and A. B. Geltmacher. Spatial distribution of voids in HY-100 steel by X-ray tomography. *Scripta Materialia*, 44:165–169, 2001. URL <http://www.scopus.com/inward/record.url?eid=2-s2.0-0035097391&partnerID=40&md5=43be85b396be12618cca73b451c75d22>.
- [34] S. F. Nielsen. X-ray diffraction and absorption tomography for three dimensional measurements in bulk material. In *Advanced X-ray Techniques in Research and Industry*, pages 143–171. IOS Press, Amsterdam, The Netherlands, 2005.
- [35] S. Schmidt, S. F. Nielsen, C. Gundlach, L. Margulies, X. Huang, and D. J. Jensen. Watching the growth of bulk grains during recrystallization of deformed metals. *Science (New York, N.Y.)*, 305(5681):229–32, July 2004. ISSN 1095-9203. doi: 10.1126/science.1098627. URL <http://www.sciencemag.org/content/305/5681/229.abstract>.
- [36] M. Uchic, M. Groeber, R. Wheeler IV, R. Kerns, F. Scheltens, and D. Dimiduk. Microstructural Characterization of Aerospace Materials via Serial Sectioning Using the Dual Beam FIB-SEM. *Microscopy and Microanalysis*, 11:666–667, 2005.
- [37] J. E. Spowart. Automated serial sectioning for 3-D analysis of microstructures. *Scripta Materialia*, 55(1):5–10, July 2006. ISSN 13596462. doi: 10.1016/j.scriptamat.2006.01.019. URL <http://dx.doi.org/10.1016/j.scriptamat.2006.01.019>.
- [38] F. H. Garzon, S. H. Lau, J. R. Davey, and R. Borup. Micro And Nano X-Ray Tomography Of PEM Fuel Cell Membranes After Transient Operation. *ECS Transactions*, 11(1):1139–1149, September 2007. ISSN 1938-5862. doi: 10.1149/1.2781026. URL <http://ecst.ecsdl.org/content/11/1/1139.abstract>.
- [39] S. H. Lau, W. K. S. Chiu, F. Garzon, H. Chang, A. Tkachuk, M. Feser, and W. Yun. Non invasive, multiscale 3D X-Ray characterization of porous functional composites and membranes, with resolution from MM to sub 50 NM. *Journal of Physics: Conference*

- Series*, 152(1):012059, March 2009. ISSN 1742-6596. doi: 10.1088/1742-6596/152/1/012059. URL <http://stacks.iop.org/1742-6596/152/i=1/a=012059>.
- [40] Z. Yan, O. Guillon, S. Wang, C. L. Martin, C. Lee, and D. Bouvard. Synchrotron x-ray nano-tomography characterization of the sintering of multilayered systems. *Applied Physics Letters*, 100(26):263107, June 2012. ISSN 00036951. doi: 10.1063/1.4730625. URL <http://link.aip.org/link/?APPLAB/100/263107/1>.
- [41] Y. Wang, Y. K. Chen, and W. K. Chiu. In Situ 3D Imaging and Characterization of Nano-Structures with X-ray Nano-CT Technique. *ECS Transactions*, 35(24):21–29, October 2011. ISSN 1938-5862. doi: 10.1149/1.3643331. URL <http://ecst.ecsdl.org/content/35/24/21.abstract>.
- [42] W. Chao, J. Kim, S. Rekawa, P. Fischer, and E. H. Anderson. Demonstration of 12 nm Resolution Fresnel Zone Plate Lens based Soft X-ray Microscopy. *Optics Express*, 17(20):17669, September 2009. ISSN 1094-4087. doi: 10.1364/OE.17.017669. URL <http://www.opticsexpress.org/abstract.cfm?URI=oe-17-20-17669>.
- [43] S. B. Leighton. SEM images of block faces, cut by a miniature microtome within the SEM - a technical note. *Scanning electron microscopy*, ~ (Pt 2):73–6, January 1981. ISSN 0586-5581. URL <http://www.ncbi.nlm.nih.gov/pubmed/7323733>.
- [44] W. Denk and H. Horstmann. Serial block-face scanning electron microscopy to reconstruct three-dimensional tissue nanostructure. *PLoS biology*, 2(11):e329, November 2004. ISSN 1545-7885. doi: 10.1371/journal.pbio.0020329. URL <http://www.pubmedcentral.nih.gov/articlerender.fcgi?artid=524270&tool=pmcentrez&rendertype=abstract>.
- [45] M. P. Echlin, N. S. Hussein, J. A. Nees, and T. M. Pollock. A new femtosecond laser-based tomography technique for multiphase materials. *Advanced materials (Deerfield Beach, Fla.)*, 23(20):2339–42, May 2011. ISSN 1521-4095. doi: 10.1002/adma.201003600. URL <http://www.ncbi.nlm.nih.gov/pubmed/21608045>.
- [46] J. H. Macke, N. Maack, R. Gupta, W. Denk, B. Schölkopf, and A. Borst. Contour-propagation algorithms for semi-automated reconstruction of neural processes. *Journal of neuroscience methods*, 167(2):349–57, January 2008. ISSN 0165-0270. doi: 10.1016/j.jneumeth.2007.07.021. URL <http://dx.doi.org/10.1016/j.jneumeth.2007.07.021>.
- [47] Gatan. Gatan Inc. 3View, 2007. URL http://www.gatan.com/products/sem_products/products/3View_landing.php.
- [48] Gatan. Gatan, Inc: Imaging Software DigitalMicrograph, 2007. URL http://www.gatan.com/imaging/dig_micrograph.php.

- [49] G. E. Thompson, T. Hashimoto, X. L. Zhong, M. Curioni, X. Zhou, P. Skeldon, P. J. Withers, J. Carr, and A. G. Monteith. Revealing the 3D Internal Structure of Aluminium and its Alloys. In *Aluminium Surface Science & Technology VI*, Sorrento, Italy, 2012.
- [50] B. Girod, H. Niemann, and G. Greiner. *Principles of 3D Image Analysis and Synthesis*. Kluwer Academic Publishers, Norwell, MA, USA, 2000. ISBN 0792378504.
- [51] O. Lezoray. Graph theory concepts and definitions used in image processing and analysis. In *Image Processing and Analysis with Graphs*, Digital Imaging and Computer Vision. CRC Press, June 2012. ISBN 978-1-4398-5507-2. doi: doi:10.1201/b12281-2. URL <http://dx.doi.org/10.1201/b12281-2>.
- [52] A. Michael, J. Orteu, and H. W. Schreier. Introduction. In *Image Correlation for Shape, Motion and Deformation Measurements SE - 1*, pages 1–12. Springer US, 2009. ISBN 978-0-387-78746-6. doi: 10.1007/978-0-387-78747-3_1. URL http://dx.doi.org/10.1007/978-0-387-78747-3_1.
- [53] A. C. Kak and M. Slaney. *Principles of Computerized Tomographic Imaging*. Society of Industrial and Applied Mathematics, 2001.
- [54] W. H. Press, S. A. Teukolsky, W. T. Vetterling, and B. P. Flannery. Minimization or maximization of functions. In *Numerical Recipes in C*, pages 394–455. Cambridge University Press, December 1992. ISBN 0-521-43108-5. URL <http://dl.acm.org/citation.cfm?id=148286>.
- [55] F. Grund. Herman, G. T. (Ed.), Image Reconstruction from Projections. Implementation and Applications. Topics in Applied Physics 32. Berlin-Heidelberg-New York, Springer-Verlag 1979. XII, 284 S., 120 Abb., 10 Tab., DM 98., US \$53.90. ISBN 3-540-09417-2. *ZAMM - Journal of Applied Mathematics and Mechanics / Zeitschrift für Angewandte Mathematik und Mechanik*, 60(11):643–644, January 1980. ISSN 1521-4001. doi: 10.1002/zamm.19800601139. URL <http://dx.doi.org/10.1002/zamm.19800601139>.
- [56] K. Van Laere, M. Koole, I. Lemahieu, and R. Dierckx. Image filtering in single-photon emission computed tomography: principles and applications. *Computerized medical imaging and graphics : the official journal of the Computerized Medical Imaging Society*, 25(2):127–33, 2001. ISSN 0895-6111. URL <http://www.ncbi.nlm.nih.gov/pubmed/11137789>.
- [57] A. M. Cormack. Representation of a Function by Its Line Integrals, with Some Radiological Applications. *Journal of Applied Physics*, 34(9):2722, June 1963. ISSN 00218979. doi: 10.1063/1.1729798. URL <http://scitation.aip.org/content/aip/journal/jap/34/9/10.1063/1.1729798>.

- [58] A. M. Cormack. Representation of a Function by Its Line Integrals, with Some Radiological Applications. II. *Journal of Applied Physics*, 35(10):2908, July 1964. ISSN 00218979. doi: 10.1063/1.1713127. URL <http://scitation.aip.org/content/aip/journal/jap/35/10/10.1063/1.1713127>.
- [59] G. Gindi, M. Lee, A. Rangarajan, and I. G. Zubal. Bayesian reconstruction of functional images using anatomical information as priors. *IEEE transactions on medical imaging*, 12(4):670–80, January 1993. ISSN 0278-0062. doi: 10.1109/42.251117. URL <http://www.ncbi.nlm.nih.gov/pubmed/18218461>.
- [60] B. A. Ardekani, M. Braun, B. F. Hutton, I. Kanno, and H. Iida. Minimum cross-entropy reconstruction of PET images using prior anatomical information. *Physics in Medicine and Biology*, 41(11):2497–2517, November 1996. ISSN 0031-9155. doi: 10.1088/0031-9155/41/11/018. URL <http://stacks.iop.org/0031-9155/41/i=11/a=018>.
- [61] A. P. Dempster, N. M. Laird, and D. B. Rubin. Maximum Likelihood from Incomplete Data via the EM Algorithm, 1976. URL <http://dash.harvard.edu/handle/1/3426318>.
- [62] K. Lange and R. Carson. EM reconstruction algorithms for emission and transmission tomography. *Journal of computer assisted tomography*, 8(2):306–16, April 1984. ISSN 0363-8715. URL <http://www.ncbi.nlm.nih.gov/pubmed/6608535>.
- [63] L. A. Shepp and Y. Vardi. Maximum likelihood reconstruction for emission tomography. *IEEE transactions on medical imaging*, 1(2):113–22, January 1982. ISSN 0278-0062. doi: 10.1109/TMI.1982.4307558. URL <http://www.ncbi.nlm.nih.gov/pubmed/18238264>.
- [64] P. P. Bruyant. Analytic and Iterative Reconstruction Algorithms in SPECT. *J. Nucl. Med.*, 43(10):1343–1358, October 2002. URL <http://jnm.snmjournals.org/content/43/10/1343.long>.
- [65] A. Kyrieleis, M. Ibson, V. Titarenko, and P. J. Withers. Image stitching strategies for tomographic imaging of large objects at high resolution at synchrotron sources. *Nuclear Instruments and Methods in Physics Research Section A: Accelerators, Spectrometers, Detectors and Associated Equipment*, 607(3):677–684, August 2009. ISSN 01689002. doi: 10.1016/j.nima.2009.06.030. URL <http://www.sciencedirect.com/science/article/pii/S0168900209012406>.
- [66] V. Titarenko, R. Bradley, C. Martin, P. J. Withers, and S. Titarenko. Regularization methods for inverse problems in x-ray tomography. In *SPIE 7804, Developments in X-Ray Tomography VII*, volume 7804, pages 78040Z–78040Z–10, 2010. URL <http://dx.doi.org/10.1117/12.860260>.

- [67] A. Kyrieleis, V. Titarenko, M. Ibison, T. Connolley, and P. J. Withers. Region-of-interest tomography using filtered backprojection: assessing the practical limits. *Journal of Microscopy*, 241(1):69–82, January 2011. ISSN 1365-2818. doi: 10.1111/j.1365-2818.2010.03408.x. URL <http://dx.doi.org/10.1111/j.1365-2818.2010.03408.x>.
- [68] S. R. Deans. *The Radon Transform and Some of Its Applications*. Dover, 2007.
- [69] A. Rosenfeld and A. C. Kak. *Digital Picture Processing*. Academic Press, Inc., New York, second edition, 1982.
- [70] B. Jahne. *Digital Image Processing*. Springer-Verlag, Berlin/Heidelberg, 2005. ISBN 3-540-24035-7. doi: 10.1007/3-540-27563-0. URL <http://link.springer.com/10.1007/3-540-27563-0>.
- [71] J. C. Russ. *The Image Processing Handbook*. CRC Press, Boca Raton, sixth edition, 2011.
- [72] S. B. Damelin and W. Miller. *The Mathematics of Signal Processing*. publisherNameCambridge University Press, 2011. URL <http://dx.doi.org/10.1017/CB09781139003896>.
- [73] G. Sapiro. *Geometric Partial Differential Equations and Image Analysis*. Cambridge University Press, 2006. ISBN 0521685079. URL <http://books.google.com/books?hl=en&lr=&id=LFzGwdi0KtsC&pgis=1>.
- [74] A. Fick. Ueber Diffusion. *Annalen der Physik und Chemie*, 170(1):59–86, 1855. ISSN 00033804. doi: 10.1002/andp.18551700105. URL <http://doi.wiley.com/10.1002/andp.18551700105>.
- [75] J. Serra. *Image Analysis and Mathematical Morphology*. Academic Press, Inc., January 1983. ISBN 0126372403. URL <http://dl.acm.org/citation.cfm?id=1098652>.
- [76] N. Otsu. A Threshold Selection Method from Gray-Level Histograms, 1979.
- [77] R. Yager. ON THE MEASURE OF FUZZINESS AND NEGATION Part I: Membership in the Unit Interval. *International Journal of General Systems*, 5(4):221–229, January 1979. ISSN 0308-1079. doi: 10.1080/03081077908547452. URL <http://dx.doi.org/10.1080/03081077908547452>.
- [78] A. Magid, S. R. Rotman, and A. M. Weiss. Comments on Picture thresholding using an iterative selection method, 1990.
- [79] J. R. Parker. *Algorithms for Image Processing and Computer Vision*. John Wiley & Sons, second edition, 2010.

- [80] M. Sezgin and B. Sankur. Survey over image thresholding techniques and quantitative performance evaluation. *Journal of Electronic Imaging*, 13(1):146–168, 2004. ISSN 1017-9909. URL <http://dx.doi.org/10.1117/1.1631315>.
- [81] S. Beucher and C. Lantuejoul. Use of Watersheds in Contour Detection. In *International Workshop on Image Processing: Real-time Edge and Motion Detection/Estimation, Rennes, France.*, 1979. URL [citeulike-article-id:2335595](http://dx.doi.org/10.1117/1.1631315).
- [82] C. Lantuejoul and S. Beucher. On the use of the geodesic metric in image analysis. *Journal of Microscopy*, 121(1):39–49, January 1981. ISSN 1365-2818. doi: 10.1111/j.1365-2818.1981.tb01197.x. URL <http://dx.doi.org/10.1111/j.1365-2818.1981.tb01197.x>.
- [83] H. Q. Sun and Y. J. Luo. Adaptive watershed segmentation of binary particle image. *Journal of microscopy*, 233(2):326–30, February 2009. ISSN 1365-2818. doi: 10.1111/j.1365-2818.2009.03125.x. URL <http://www.ncbi.nlm.nih.gov/pubmed/19220699>.
- [84] R. C. Gonzalez and R. E. Woods. *Digital Image Processing*. Prentice Hall, 3rd edition, 2008.
- [85] Y. Han and R. A. Wagner. An efficient and fast parallel-connected component algorithm. *Journal of the ACM*, 37(3):626–642, July 1990. ISSN 00045411. doi: 10.1145/79147.214077. URL <http://dl.acm.org/citation.cfm?id=79147.214077>.
- [86] K. Suzuki, I. Horiba, and N. Sugie. Linear-time connected-component labeling based on sequential local operations. *Computer Vision and Image Understanding*, 89(1):1–23, January 2003. ISSN 10773142. doi: 10.1016/S1077-3142(02)00030-9. URL [http://dx.doi.org/10.1016/S1077-3142\(02\)00030-9](http://dx.doi.org/10.1016/S1077-3142(02)00030-9).
- [87] M. B. Dillencourt, H. Samet, and M. Tamminen. A general approach to connected-component labeling for arbitrary image representations. *Journal of the ACM*, 39(2):253–280, April 1992. ISSN 00045411. doi: 10.1145/128749.128750. URL <http://dl.acm.org/citation.cfm?id=128749.128750>.
- [88] H. Samet and M. Tamminen. Efficient component labeling of images of arbitrary dimension represented by linear bintrees. *IEEE Transactions on Pattern Analysis and Machine Intelligence*, 10(4):579–586, July 1988. ISSN 01628828. doi: 10.1109/34.3918. URL <http://ieeexplore.ieee.org/lpdocs/epic03/wrapper.htm?arnumber=3918>.
- [89] D. Kleppner. *An introduction to mechanics*. Cambridge University Press, 2nd edition, 1973.
- [90] H. G. Merkus. *Particle Size Measurements: Fundamentals, Practice, Quality*. Springer, 2009.

- [91] M. L. Boas. *Mathematical Methods in the Physical Sciences*. Wiley, third edition, 2006. ISBN 0-471-36580-7.
- [92] H. Freeman. On the Encoding of Arbitrary Geometric Configurations. *IEEE Transactions on Electronic Computers*, EC-10(2):260–268, June 1961. ISSN 0367-7508. doi: 10.1109/TEC.1961.5219197. URL <http://ieeexplore.ieee.org/lpdocs/epic03/wrapper.htm?arnumber=5219197>.
- [93] J. Lindblad and I. Nyström. Surface Area Estimation of Digitized 3D Objects Using Local Computations. In Achille Braquelaire, Jacques-Olivier Lachaud, and Anne Vialard, editors, *Discrete Geometry for Computer Imagery SE - 24*, volume 2301 of *Lecture Notes in Computer Science*, pages 267–278. Springer Berlin Heidelberg, 2002. ISBN 978-3-540-43380-4. doi: 10.1007/3-540-45986-3_24. URL http://dx.doi.org/10.1007/3-540-45986-3_24.
- [94] C. Maple. Geometric design and space planning using the marching squares and marching cube algorithms, 2003.
- [95] W. E. Lorensen and H. E. Cline. Marching cubes: A high resolution 3D surface construction algorithm. *ACM SIGGRAPH Computer Graphics*, 21(4):163–169, August 1987. ISSN 00978930. doi: 10.1145/37402.37422. URL <http://dl.acm.org/citation.cfm?id=37402.37422>.
- [96] S. S. Chern. *Studies In Mathematics Volume 4 Studies In Global Geometry and Analysis*. Prentice Hall, 1967.
- [97] H. Wadell. Volume, Shape, and Roundness of Quartz Particles. *The Journal of Geology*, 43(3):250–280, April 1935. ISSN 00221376. doi: 10.2307/30056250. URL <http://www.jstor.org/stable/30056250>.
- [98] P. Hertz. Über den gegenseitigen durchschnittlichen Abstand von Punkten, die mit bekannter mittlerer Dichte im Raume angeordnet sind. *Mathematische Annalen*, 67(3): 387–398, 1909. ISSN 0025-5831. doi: 10.1007/BF01450410. URL <http://dx.doi.org/10.1007/BF01450410>.
- [99] S. Chandrasekhar. Stochastic Problems in Physics and Astronomy. *Reviews of Modern Physics*, 15(1):1–89, January 1943. ISSN 0034-6861. doi: 10.1103/RevModPhys.15.1. URL <http://link.aps.org/doi/10.1103/RevModPhys.15.1>.
- [100] MATLAB. *Version R2012a (7.14.0.739)*. The Mathworks Inc., Natick, Massachusetts, 2012. URL <http://www.mathworks.co.uk/>.
- [101] J. Holewinski, R. Ramamurthi, M. Ravishankar, N. Fauzia, L. Pouchet, A. Rountev, and P. Sadayappan. Dynamic trace-based analysis of vectorization potential of applications. In *Proceedings of the 33rd ACM SIGPLAN conference on Programming Language*

- Design and Implementation - PLDI '12*, volume 47, page 371, New York, New York, USA, June 2012. ACM Press. ISBN 9781450312059. doi: 10.1145/2254064.2254108. URL <http://dl.acm.org/citation.cfm?id=2254064.2254108>.
- [102] P. J. Clark and F. C. Evans. Distance to Nearest Neighbor as a Measure of Spatial Relationships in Populations. *Ecology*, 35:445–453, 1954. ISSN 00129658. URL <http://www.jstor.org/stable/1931034>.
- [103] The OpenFOAM Foundation, 2012. URL <http://www.openfoam.org/>.
- [104] H. Hege, M. Seebaß, and D. Stalling. A generalized marching cubes algorithm based on non-binary classifications. Technical report, Konrad-Zuse-Zentrum für Informationstechnik Berlin, 1997. URL <http://citeseerx.ist.psu.edu/viewdoc/summary?doi=10.1.1.90.1282>.
- [105] R. D. Cook, D. S. Malkus, M. E. Plesha, and R. J. Witt. *Concepts and Applications of Finite Element Analysis*. John Wiley & Sons, 4th edition, 2007. ISBN 0470088214.
- [106] I. M. Smith and D. V. Griffiths. *Programming the Finite Element Method*. John Wiley & Sons, Inc., New York, NY, USA, 3rd edition, 1998. ISBN 0471965421.
- [107] O. C. Zienkiewicz. *The Finite Element Method Set*, volume null. Elsevier, 2005. ISBN 9780750664318. doi: 10.1016/B978-075066431-8.50169-7. URL <http://dx.doi.org/10.1016/B978-075066431-8.50169-7>.
- [108] S. S. Rao. *The Finite Element Method in Engineering*. Elsevier, 2005. ISBN 9780750678285. doi: 10.1016/B978-075067828-5/50002-0. URL <http://www.sciencedirect.com/science/article/pii/B9780750678285500020>.
- [109] G. Strang and G. Fix. *An Analysis of the Finite Element Method*. Prentice Hall, 1st edition, 1973.
- [110] D. V. Griffiths. Stiffness matrix of the four-node quadrilateral element in closed form. *International Journal for Numerical Methods in Engineering*, 37(6):1027–1038, March 1994. ISSN 1097-0207. doi: 10.1002/nme.1620370609. URL <http://dx.doi.org/10.1002/nme.1620370609>.
- [111] E. Hecht. *Optics (4th Edition)*. Addison Wesley, August 2001. ISBN 0805385665. URL [citeulike-article-id:319275http://www.amazon.ca/exec/obidos/redirect?tag=citeulike09-20&path=ASIN/0805385665](http://www.amazon.ca/exec/obidos/redirect?tag=citeulike09-20&path=ASIN/0805385665).
- [112] M. Born. *Principles of optics : electromagnetic theory of propagation, interference and diffraction of light / by Max Born and Emil Wolf*. Pergamon Press, New York, 1959.
- [113] F. R. S. Rayleigh. XXXI. Investigations in optics, with special reference to the spectroscope. *Philosophical Magazine Series 5*, 8(49):261–274, October 1879. ISSN

- 1941-5982. doi: 10.1080/14786447908639684. URL <http://dx.doi.org/10.1080/14786447908639684>.
- [114] H. Yang, S. Zhu, and N. Pan. Studying the mechanisms of titanium dioxide as ultraviolet-blocking additive for films and fabrics by an improved scheme. *Journal of Applied Polymer Science*, 92(5):3201–3210, June 2004. ISSN 1097-4628. doi: 10.1002/app.20327. URL <http://dx.doi.org/10.1002/app.20327>.
- [115] Oil Association and Colour Chemists'. Extender Pigments. In *Surface Coatings SE - 28*, pages 344–351. Springer Netherlands, 1983. ISBN 978-94-011-6942-4. doi: 10.1007/978-94-011-6940-0_28. URL http://dx.doi.org/10.1007/978-94-011-6940-0_28.
- [116] J. C. Auger, R. G. Barrera, and B. Stout. Scattering efficiency of clusters composed by aggregated spheres. *Journal of Quantitative Spectroscopy and Radiative Transfer*, 79-80:521–531, June 2003. ISSN 00224073. doi: 10.1016/S0022-4073(02)00305-9. URL <http://www.sciencedirect.com/science/article/pii/S0022407302003059>.
- [117] J. C. Auger, B. Stout, R. G. Barrera, and F. Curiel. Scattering properties of rutile pigments located eccentrically within microvoids. *Journal of Quantitative Spectroscopy and Radiative Transfer*, 70(4-6):675–695, August 2001. ISSN 00224073. doi: 10.1016/S0022-4073(01)00037-1. URL <http://www.sciencedirect.com/science/article/pii/S0022407301000371>.
- [118] J. C. Maxwell. A Dynamical Theory of the Electromagnetic Field. [Abstract]. *Proceedings of the Royal Society of London*, 13:531–536, 1863. ISSN 03701662. URL <http://www.jstor.org/stable/112081>.
- [119] A. R. Jones. Light scattering for particle characterization. *Progress in Energy and Combustion Science*, 25:1–53, 1999. ISSN 0360-1285. doi: 10.1016/S0360-1285(98)00017-3. URL <http://www.sciencedirect.com/science/article/pii/S0360128598000173>.
- [120] L. Lorenz. Lysbevægelsen i og uden for en af plane Lysbølger belyst Kugle. *Vidensk. Selk. Skr.*, 6(6):1–62, 1890.
- [121] G. Mie. Beiträge zur Optik trüber Medien, speziell kolloidaler Metallösungen. *Leipzig Ann. Phys.*, 330(3):377, 1908.
- [122] R. M. Drake. Mie scattering. *American Journal of Physics*, 53(10):955, October 1985. ISSN 00029505. doi: 10.1119/1.14011. URL <http://link.aip.org/link/?AJPIAS/53/955/1>.
- [123] F. R. S. Rayleigh. X. On the electromagnetic theory of light. *Philosophical Magazine Series 5*, 12(73):81–101, August 1881. ISSN 1941-5982. doi: 10.1080/14786448108627074. URL <http://dx.doi.org/10.1080/14786448108627074>.

- [124] J. E. Hansen and L. D. Travis. Light scattering in planetary atmospheres. *Space Science Reviews*, 16:527–610, 1974. URL <http://www.scopus.com/inward/record.url?eid=2-s2.0-0001310874&partnerID=40&md5=bc9b6ea7dd220e7aca0ff5291f375056>.
- [125] S. Asano and G. Yamamoto. Light scattering by a spheroidal particle. *Applied Optics*, 14:29–49, 1975. URL <http://www.scopus.com/inward/record.url?eid=2-s2.0-0016767434&partnerID=40&md5=71190fd36578133123579ae9e68ac3ed>.
- [126] P. C. Waterman. Matrix formulation of electromagnetic scattering. *Proceedings of the IEEE*, 53(8):805–812, 1965. ISSN 0018-9219. doi: 10.1109/PROC.1965.4058. URL <http://ieeexplore.ieee.org/xpl/articleDetails.jsp?arnumber=1445988>.
- [127] M. I. Mishchenko, L. D. Travis, and D. W. Mackowski. T-matrix computations of light scattering by nonspherical particles: A review. *Journal of Quantitative Spectroscopy and Radiative Transfer*, 55(5):535–575, May 1996. ISSN 00224073. doi: 10.1016/0022-4073(96)00002-7. URL [http://dx.doi.org/10.1016/0022-4073\(96\)00002-7](http://dx.doi.org/10.1016/0022-4073(96)00002-7).
- [128] J. Bruning. Multiple scattering of EM waves by spheres part I—Multipole expansion and ray-optical solutions. *IEEE Transactions on Antennas and Propagation*, 19(3):378–390, May 1971. ISSN 0096-1973. doi: 10.1109/TAP.1971.1139944. URL <http://ieeexplore.ieee.org/xpl/articleDetails.jsp?arnumber=1139944>.
- [129] J. Bruning. Multiple scattering of EM waves by spheres part II—Numerical and experimental results. *IEEE Transactions on Antennas and Propagation*, 19(3):391–400, May 1971. ISSN 0096-1973. doi: 10.1109/TAP.1971.1139925. URL <http://ieeexplore.ieee.org/xpl/articleDetails.jsp?arnumber=1139925>.
- [130] B. Peterson and S. Ström. T Matrix for Electromagnetic Scattering from an Arbitrary Number of Scatterers and Representations of $E(3)$. *Physical Review D*, 8(10):3661–3678, November 1973. ISSN 0556-2821. doi: 10.1103/PhysRevD.8.3661. URL <http://link.aps.org/doi/10.1103/PhysRevD.8.3661>.
- [131] B. Peterson. Multiple scattering of waves by an arbitrary lattice. *Physical Review A*, 16(4):1363–1370, October 1977. ISSN 0556-2791. doi: 10.1103/PhysRevA.16.1363. URL <http://link.aps.org/doi/10.1103/PhysRevA.16.1363>.
- [132] E. H. Newman and K. Kingsley. An introduction to the method of moments. *Computer Physics Communications*, 68(1-3):1–18, November 1991. ISSN 00104655. doi: 10.1016/0010-4655(91)90191-M. URL [http://dx.doi.org/10.1016/0010-4655\(91\)90191-M](http://dx.doi.org/10.1016/0010-4655(91)90191-M).
- [133] W. C. Gibson. *The Method of Moments in Electromagnetics*. CRC Press, 2008.
- [134] E. Newman, P. Alexandropoulos, and E. Walton. Polygonal plate modeling of realistic structures. *IEEE Transactions on Antennas and Propagation*, 32(7):742–747, July 1984.

- ISSN 0096-1973. doi: 10.1109/TAP.1984.1143408. URL <http://ieeexplore.ieee.org/xpl/articleDetails.jsp?arnumber=1143408>.
- [135] W. A. Johnson, D. R. Wilton, and R. M. Sharpe. Modeling Scattering From and Radiation by Arbitrary Shaped Objects with the Electric Field Integral Equation Triangular Surface Patch Code. *Electromagnetics*, 10(1-2):41–63, January 1990. ISSN 0272-6343. doi: 10.1080/02726349008908228. URL <http://dx.doi.org/10.1080/02726349008908228>.
- [136] Y. M. Wang and W. C. Chew. Recursive T-matrix approach for the solution of electromagnetic scattering by many spheres. *IEEE Transactions on Antennas and Propagation*, 41:1633–1639, 1993. URL <http://www.scopus.com/inward/record.url?eid=2-s2.0-0027876061&partnerID=40&md5=b6579e4645e6dd0fc0ba6b8f723d86a0>.
- [137] Z. L. Wang, L. Hu, and W. G. Lin. A modified T-matrix formulation for multiple scattering of electromagnetic waves. *Journal of Physics D: Applied Physics*, 27(3):447–451, March 1994. ISSN 0022-3727. doi: 10.1088/0022-3727/27/3/003. URL <http://stacks.iop.org/0022-3727/27/i=3/a=003>.
- [138] D. W. Mackowski and M. I. Mishchenko. Calculation of the T matrix and the scattering matrix for ensembles of spheres. *Journal of the Optical Society of America A*, 13(11):2266, November 1996. ISSN 1084-7529. doi: 10.1364/JOSAA.13.002266. URL <http://josaa.osa.org/abstract.cfm?URI=josaa-13-11-2266>.
- [139] G. W. Kattawar and G. N. Plass. Radiance and Polarization of Multiple Scattered Light from Haze and Clouds. *Applied Optics*, 7(8):1519, August 1968. ISSN 0003-6935. doi: 10.1364/AO.7.001519. URL <http://ao.osa.org/abstract.cfm?URI=ao-7-8-1519>.
- [140] E. A. Bucher. Computer simulation of light pulse propagation for communication through thick clouds. *Applied Optics*, 12:2391–2400, 1973. URL <http://www.scopus.com/inward/record.url?eid=2-s2.0-0015673357&partnerID=40&md5=e3a5e79547fde0ba1f8235a024caf757>.
- [141] A. D. Code and B. A. Whitney. Polarization from scattering in blobs. *Astrophysical Journal Letters*, 441:400–407, 1995. URL <http://www.scopus.com/inward/record.url?eid=2-s2.0-11944273448&partnerID=40&md5=15434bcaedac489f825f1610c03d3048>.
- [142] L. Bergougnoux, J. Misguich-Ripault, J. Firpo, and J. Andre. Monte Carlo calculation of backscattered light intensity by suspension: comparison with experimental data. *Applied Optics*, 35:1735–1741, 1996. URL <http://www.scopus.com/inward/record.url?eid=2-s2.0-0030122725&partnerID=40&md5=f7dad01d4553ef381c81c71e6fdd8541>.

- [143] P. S. Mudgett and L. W. Richards. Multiple Scattering Calculations for Technology. *Applied Optics*, 10(7):1485, July 1971. ISSN 0003-6935. doi: 10.1364/AO.10.001485. URL <http://ao.osa.org/abstract.cfm?URI=ao-10-7-1485>.
- [144] P. Kubelka and F. Munk. Reflection Characteristics of Paints. *Zeitschrift fur Technische Physik*, 12:593–601, 1931.
- [145] R. Molenaar, J. J. ten Bosch, and J. R. Zijp. Determination of Kubelka-Munk Scattering and Absorption Coefficients by Diffuse Illumination. *Applied Optics*, 38(10):2068, April 1999. ISSN 0003-6935. doi: 10.1364/AO.38.002068. URL <http://ao.osa.org/abstract.cfm?URI=ao-38-10-2068>.
- [146] L. Silberstein. CXIV. The transparency of turbid media. *Philosophical Magazine Series 7*, 4(26):1291–1296, 1927. ISSN 1941-5982. doi: 10.1080/14786441208564428. URL <http://www.tandfonline.com/doi/abs/10.1080/14786441208564428>.
- [147] J. Ohser and K. Sandau. Considerations About the Estimation of the Size Distribution in Wicksells Corpuscle Problem. In Klaus R. Mecke and Dietrich Stoyan, editors, *Statistical Physics and Spatial Statistics SE - 7*, volume 554 of *Lecture Notes in Physics*, pages 185–202. Springer Berlin Heidelberg, 2000. ISBN 978-3-540-67750-5. doi: 10.1007/3-540-45043-2_7. URL http://dx.doi.org/10.1007/3-540-45043-2_7.
- [148] R.A. Cottis, M.J. Graham, R Lindsay, S.B. Lyon, J.A. Richardson, J.D. Scantlebury, and F.H. Stott, editors. *Shreir's Corrosion (Fourth Edition) Volume I: Basic Concepts, High Temperature Corrosion*. Elsevier, 2010.
- [149] I. L. Rozenfeld. *Corrosion Inhibitors*. McGraw-Hill Inc., 1981. ISBN 0070541701.
- [150] L. L. Shreir, R. A. Jarman, and G. T. Burstein. Corrosion (3rd Edition) Volumes 1-2, 1993. URL <http://app.knovel.com/hotlink/toc/id:kpCEV00003/corrosion-3rd-edition/corrosion-3rd-edition>.
- [151] R. E. Evans. *The Corrosion and Oxidation of Metals*. Edward Arnold (Publishers) Ltd., 1960.
- [152] Anon. *BS EN ISO 8044:2000, Corrosion of metals and alloys. Basic terms and definitions*. BSI, 2000. ISBN 0 580 32611 X.
- [153] S. Matsuda and H. H. Uhlig. Effect of pH, Sulfates, and Chlorides on Behavior of Sodium Chromate and Nitrite as Passivators for Steel. *Journal of The Electrochemical Society*, 111(2):156, February 1964. ISSN 00134651. doi: 10.1149/1.2426075. URL <http://jes.ecsdl.org/content/111/2/156.abstract>.

- [154] Y. F. Cheng, B. R. Rairdan, and J. L. Luo. Features of electrochemical noise generated during pitting of inhibited A516-70 carbon steel in chloride solutions. *Journal of Applied Electrochemistry*, 28(12):1371–1375, 1998. ISSN 0021-891X. doi: 10.1023/A:1003456009378. URL <http://dx.doi.org/10.1023/A:1003456009378>.
- [155] J. L. Dawson. *Electrochemical Noise Measurement for Corrosion Applications*. ASTM, West Conshohocken, PA, 1996.
- [156] Z. H. Dong, X. P. Guo, J. X. Zheng, and L. M. Xu. Investigation on inhibition of CrO₄²⁻ and MoO₄²⁻ ions on carbon steel pitting corrosion by electrochemical noise analysis. *Journal of Applied Electrochemistry*, 32(4):395–400, 2002. ISSN 0021-891X. doi: 10.1023/A:1016340421529. URL <http://dx.doi.org/10.1023/A:1016340421529>.
- [157] M. J. Pryor and M. Cohen. The Inhibition of the Corrosion of Iron by Some Anodic Inhibitors. *Journal of The Electrochemical Society*, 100(5):203, May 1953. ISSN 00134651. doi: 10.1149/1.2781106. URL <http://jes.ecsdl.org/content/100/5/203.abstract>.
- [158] W. R. Dunstan and J. R. Hill. The aerial oxidation (rusting) of metals. *Journal of the Chemical Society, Transactions*, 99:1835, January 1911. ISSN 0368-1645. doi: 10.1039/ct9119901835. URL <http://pubs.rsc.org/en/content/articlehtml/1911/ct/ct9119901835>.
- [159] H. H. Uhlig. Discussion of Effect of Adsorbed Polar Organic Compounds on Activity of Steel in Acid Solution [Norman Hackerman and E. L. Cook (pp. 19)]. *Journal of The Electrochemical Society*, 97(12):462, December 1950. ISSN 00134651. doi: 10.1149/1.2777909. URL <http://jes.ecsdl.org/content/97/12/462.1.abstract>.
- [160] E. Chyzewski and U. R. Evans. The Classification of Anodic and Cathodic Inhibitors. *Transactions of The Electrochemical Society*, 76(1):215, January 1939. ISSN 00964743. doi: 10.1149/1.3500263. URL <http://jes.ecsdl.org/content/76/1/215.abstract>.
- [161] G. G. Eldredge and R. B. Mears. Inhibitors of Corrosion of Aluminum. *Industrial & Engineering Chemistry*, 37(8):736–741, August 1945. ISSN 0019-7866. doi: 10.1021/ie50428a019. URL <http://dx.doi.org/10.1021/ie50428a019>.
- [162] C. Edeleanu and U. R. Evans. The causes of the localized character of corrosion on aluminium. *Transactions of the Faraday Society*, 47:1121, January 1951. ISSN 0014-7672. doi: 10.1039/tf9514701121. URL <http://pubs.rsc.org/en/content/articlehtml/1951/tf/tf9514701121>.
- [163] T. P. Hoar. The breakdown and repair of oxide films on iron. *Transactions of the Faraday Society*, 45:683, January 1949. ISSN 0014-7672. doi: 10.1039/tf9494500683. URL <http://pubs.rsc.org/en/content/articlehtml/1949/tf/tf9494500683>.

- [164] M. Koudelkova. On the Composition of the Passivating Films Formed on Aluminum in Chromate Solutions. *Journal of The Electrochemical Society*, 124(8):1165, August 1977. ISSN 00134651. doi: 10.1149/1.2133520. URL <http://jes.ecsdl.org/content/124/8/1165.abstract>.
- [165] A. Trueman, S. Knight, J. Colwell, T. Hashimoto, J. Carr, P. Skeldon, and G. E. Thompson. 3-D tomography by automated in situ block face ultramicrotome imaging using an FEG-SEM to study complex corrosion protective paint coatings. *Corrosion Science*, 75(null):376–385, October 2013. ISSN 0010938X. doi: 10.1016/j.corsci.2013.06.021. URL <http://dx.doi.org/10.1016/j.corsci.2013.06.021>.
- [166] T. Prosek and D. Thierry. A model for the release of chromate from organic coatings. *Progress in Organic Coatings*, 49(3):209–217, April 2004. ISSN 03009440. doi: 10.1016/j.porgcoat.2003.09.012. URL <http://www.sciencedirect.com/science/article/pii/S0300944003002212>.
- [167] F.H. Scholes, S.A. Furman, A.E. Hughes, T. Nikpour, N. Wright, P.R. Curtis, C.M. Macrae, S. Intem, and A.J. Hill. Chromate leaching from inhibited primers. *Progress in Organic Coatings*, 56(1):23–32, May 2006. ISSN 03009440. doi: 10.1016/j.porgcoat.2006.01.015. URL <http://www.sciencedirect.com/science/article/pii/S0300944006000269>.
- [168] Anthony E Hughes, Ivan S Cole, Tim H Muster, and Russel J Varley. Designing green, self-healing coatings for metal protection. *NPG Asia Mater*, 2:143–151, October 2010. ISSN 1884-4049. URL <http://dx.doi.org/10.1038/asiamat.2010.136>.
- [169] S. Sellaiyan, A. E. Hughes, S. V. Smith, A. Uedono, J. Sullivan, and S. Buckman. Leaching properties of chromate-containing epoxy films using radiotracers, PALS and SEM. *Progress in Organic Coatings*, 77(1):257–267, January 2014. ISSN 03009440. doi: 10.1016/j.porgcoat.2013.09.014. URL <http://www.sciencedirect.com/science/article/pii/S0300944013002592>.
- [170] J. Y. Kim, C. L. Kim, and C. H. Chung. Modeling of nuclide release from low-level radioactive paraffin waste: a comparison of simulated and real waste. *Journal of Hazardous Materials*, 94(2):161–178, October 2002. ISSN 03043894. doi: 10.1016/S0304-3894(02)00062-6. URL <http://www.sciencedirect.com/science/article/pii/S0304389402000626>.
- [171] D. R. Jenkins and A. D. Miller. A model of chromate leaching from inhibited primers. In *18th World IMACS / MODSIM Congress*, 2009. URL <http://mssanz.org.au/modsim09/A5/jenkins.pdf>.

- [172] Sakae Yagi and Daizo Kunii. Studies on combustion of carbon particles in flames and fluidized beds. *Symposium (International) on Combustion*, 5(1):231–244, January 1955. ISSN 00820784. doi: 10.1016/S0082-0784(55)80033-1. URL <http://www.sciencedirect.com/science/article/pii/S0082078455800331>.
- [173] O. Levenspiel. Fluid-Particle Reactions: Kinetics. In *Chemical Reaction Engineering*. John Wiley & Sons, 1999.
- [174] KNona C. Liddell. Shrinking core models in hydrometallurgy: What students are not being told about the pseudo-steady approximation. *Hydrometallurgy*, 79(1-2):62–68, September 2005. ISSN 0304386X. doi: 10.1016/j.hydromet.2003.07.011. URL <http://www.sciencedirect.com/science/article/pii/S0304386X0500157X>.
- [175] A. E. Hughes, A. Trinchi, F. F. Chen, Y. S. Yang, I. S. Cole, S. Sellaiyan, J. Carr, P. D. Lee, G. E. Thompson, and T. Q. Xiao. Revelation of Intertwining Organic and Inorganic Fractal Structures in Polymer Coatings. *Advanced Materials*, pages n/a–n/a, May 2014. ISSN 1521-4095. doi: 10.1002/adma.201400561. URL <http://dx.doi.org/10.1002/adma.201400561>.
- [176] A. E. Hughes, A. Trinchi, F. F. Chen, Y. S. Yang, I. S. Cole, S. Sellaiyan, J. Carr, P. D. Lee, G. E. Thompson, and T. Q. Xiao. The application of multiscale quasi 4D CT to the study of SrCrO₄ distributions and the development of porous networks in epoxy-based primer coatings. *Progress in Organic Coatings*, July 2014. ISSN 03009440. doi: 10.1016/j.porgcoat.2014.07.001. URL <http://www.sciencedirect.com/science/article/pii/S0300944014002379>.
- [177] M. Schroeder. *Fractals, Chaos, Power Laws: Minutes from an Infinite Paradise*. W. H. Freeman, New York, 1991.
- [178] Jian Li, Qian Du, and Caixin Sun. An improved box-counting method for image fractal dimension estimation. *Pattern Recognition*, 42(11):2460–2469, November 2009. ISSN 00313203. doi: 10.1016/j.patcog.2009.03.001. URL <http://www.sciencedirect.com/science/article/pii/S0031320309000843>.
- [179] Xin Li, Gang Chen, Lei Wang, Yun-Hui Mei, Xu Chen, and Guo-Quan Lu. Creep properties of low-temperature sintered nano-silver lap shear joints. *Materials Science and Engineering: A*, 579:108–113, September 2013. ISSN 09215093. doi: 10.1016/j.msea.2013.05.001. URL <http://www.sciencedirect.com/science/article/pii/S0921509313005194>.
- [180] A V Panin, A R Shugurov, and K V Oskomov. Mechanical properties of thin Ag films on a silicon substrate studied using the nanoindentation technique. *Physics of the Solid State*, 47(11):2055–2059, 2005. ISSN 1063-7834. doi: 10.1134/1.2131144. URL <http://dx.doi.org/10.1134/1.2131144>.

- [181] John G Bai, Zhiye Zach Zhang, J N Calata, and Guo-Quan Lu. Low-Temperature Sintered Nanoscale Silver as a Novel Semiconductor Device-Metallized Substrate Interconnect Material, 2006.
- [182] Xu Chen, Rong Li, Kun Qi, and Guo-Quan Lu. Tensile Behaviors and Ratcheting Effects of Partially Sintered Chip-Attachment Films of a Nanoscale Silver Paste. *Journal of Electronic Materials*, 37(10):1574–1579, 2008. ISSN 0361-5235. doi: 10.1007/s11664-008-0516-2. URL <http://dx.doi.org/10.1007/s11664-008-0516-2>.
- [183] J A Choren, S M Heinrich, and M B Silver-Thorn. Youngs modulus and volume porosity relationships for additive manufacturing applications. *Journal of Materials Science*, 48(15):5103–5112, 2013. ISSN 0022-2461. doi: 10.1007/s10853-013-7237-5. URL <http://dx.doi.org/10.1007/s10853-013-7237-5>.
- [184] J K Mackenzie. The Elastic Constants of a Solid containing Spherical Holes. *Proceedings of the Physical Society. Section B*, 63(1):2–11, January 1950. ISSN 0370-1301. doi: 10.1088/0370-1301/63/1/302. URL <http://iopscience.iop.org/0370-1301/63/1/302>.
- [185] M.F. Ashby, A.G. Evans, N.A. Fleck, L.J. Gibson, J.W. Hutchinson, and H.N.G. Wadley. *Metal Foams*. Elsevier, 2000. ISBN 9780750672191. doi: 10.1016/B978-075067219-1/50006-4. URL <http://www.sciencedirect.com/science/article/pii/B9780750672191500064>.
- [186] N. Ramakrishnan and V. S. Arunachalam. Effective elastic moduli of porous solids. *Journal of Materials Science*, 25(9):3930–3937, 1990. ISSN 0022-2461. doi: 10.1007/BF00582462. URL <http://dx.doi.org/10.1007/BF00582462>.
- [187] Anthony P. Roberts and Edward J. Garboczi. Elastic Properties of Model Porous Ceramics. *Journal of the American Ceramic Society*, 83(12):3041–3048, December 2000. ISSN 00027820. doi: 10.1111/j.1151-2916.2000.tb01680.x. URL <http://doi.wiley.com/10.1111/j.1151-2916.2000.tb01680.x>.
- [188] CharlesW. Bert. Prediction of elastic moduli of solids with oriented porosity. *Journal of Materials Science*, 20(6):2220–2224, 1985. ISSN 0022-2461. doi: 10.1007/BF01112307. URL <http://dx.doi.org/10.1007/BF01112307>.
- [189] Mark A. Knackstedt, Christoph H. Arns, Mohammad Saadatfar, Tim J. Senden, Ajay Limaye, Arthur Sakellariou, Adrian P. Sheppard, Rob M. Sok, Wolfgang Schrof, and H. Steininger. Elastic and transport properties of cellular solids derived from three-dimensional tomographic images. *Proceedings of the Royal Society A: Mathematical, Physical and Engineering Sciences*, 462(2073):2833–2862, September 2006. ISSN 1364-5021. doi: 10.1098/rspa.2006.1657. URL <http://rspa.royalsocietypublishing.org/content/462/2073/2833>.

- [190] Richard A. Hardin and Christoph Beckermann. Effect of Porosity on the Stiffness of Cast Steel. *Metallurgical and Materials Transactions A*, 38(12):2992–3006, 2007. ISSN 1073-5623. doi: 10.1007/s11661-007-9390-4. URL <http://dx.doi.org/10.1007/s11661-007-9390-4>.
- [191] P. Gadaud, X. Milhet, and S. Pautrot. Bulk and coated materials shear modulus determination by means of torsional resonant method. *Materials Science and Engineering: A*, 521:303–306, 2009. ISSN 09215093. doi: 10.1016/j.msea.2008.09.115. URL <http://www.sciencedirect.com/science/article/pii/S0921509309002068>.
- [192] Dominique Drouin, Alexandre Réal Couture, Dany Joly, Xavier Tastet, Vincent Aimez, and Raynald Gauvin. CASINO V2.42: a fast and easy-to-use modeling tool for scanning electron microscopy and microanalysis users. *Scanning*, 29(3):92–101, 2007. ISSN 0161-0457. doi: 10.1002/sca.20000. URL <http://www.ncbi.nlm.nih.gov/pubmed/17455283>.
- [193] J. Schindelin, I. Arganda-Carreras, E. Frise, V. Kaynig, M. Longair, T. Pietzsch, S. Preibisch, C. Rueden, S. Saalfeld, B. Schmid, J. Tinevez, D. J. White, V. Hartenstein, K. Eliceiri, P. Tomancak, and A. Cardona. Fiji: an open-source platform for biological-image analysis. *Nature methods*, 9(7):676–82, July 2012. ISSN 1548-7105. doi: 10.1038/nmeth.2019. URL <http://dx.doi.org/10.1038/nmeth.2019>.
- [194] I. Arganda-Carreras, C. O. S. Sorzano, R. Marabini, J. M. Carazo, C. Ortiz-de Solorzano, and J. Kybic. Consistent and Elastic Registration of Histological Sections Using Vector-Spline Regularization. In Reinhard R. Beichel and Milan Sonka, editors, *Computer Vision Approaches to Medical Image Analysis SE - 8*, volume 4241 of *Lecture Notes in Computer Science*, pages 85–95. Springer Berlin Heidelberg, 2006. ISBN 978-3-540-46257-6. doi: 10.1007/11889762_8. URL http://dx.doi.org/10.1007/11889762_8.
- [195] K. Suzuki, I. Horiba, and N. Sugie. Linear-time connected-component labeling based on sequential local operations. *Computer Vision and Image Understanding*, 89(1):1–23, January 2003. ISSN 10773142. doi: 10.1016/S1077-3142(02)00030-9. URL <http://www.sciencedirect.com/science/article/pii/S1077314202000309>.
- [196] A. Chaijaruwanich, P. Lee, R. Dashwood, Y. Youssef, and H. Nagaumi. Evolution of pore morphology and distribution during the homogenization of direct chill cast AlMg alloys. *Acta Materialia*, 55(1):285–293, January 2007. ISSN 13596454. doi: 10.1016/j.actamat.2006.08.023. URL <http://www.sciencedirect.com/science/article/pii/S1359645406005945>.

- [197] J. Z. Yi, Y. X. Gao, P. D. Lee, H. M. Flower, and T. C. Lindley. Scatter in fatigue life due to effects of porosity in cast A356-T6 aluminum-silicon alloys. *Metallurgical and Materials Transactions A*, 34(9):1879–1890, September 2003. ISSN 1073-5623. doi: 10.1007/s11661-003-0153-6. URL <http://link.springer.com/10.1007/s11661-003-0153-6>.
- [198] B. H. Hahn and D. T. Valentine. *Essential MATLAB for Engineers and Scientists*. Elsevier, fourth edition, 2010. ISBN 978-0-12-374883-6.
- [199] F. Tariq, P.D. Lee, R. Haswell, and D.W. McComb. The influence of nanoscale microstructural variations on the pellet scale flow properties of hierarchical porous catalytic structures using multiscale 3D imaging. *Chemical Engineering Science*, 66(23): 5804–5812, December 2011. ISSN 00092509. doi: 10.1016/j.ces.2011.07.034. URL <http://www.sciencedirect.com/science/article/pii/S0009250911004969>.
- [200] S. Kim and S. J. Karrila. *Microhydrodynamics: Principles and Selected Applications*. Dover Publications Inc., 2005.